

https://dspace.org/

Carbon overgrowths and ion beam modification studies of FCC crystals by ion implantation

Naidoo, Shunmugam Ramsamy

2008-06-26T07:04:42Z
http://hdl.handle.net/10539/4984

Downloaded from a DSpace repository. https://dspace.org/

Carbon overgrowths and Ion beam modification studies of FCC Crystals by Ion Implantation

Shunmugam Ramsamy Naidoo

January, 2007

Submitted in total fulfilment of the requirements

of the degree of Doctor of Philosophy

School of Physics

University of the Witwatersrand

Abstract

At the onset of this study, the work presented in Chapter 3 of this thesis was the primary focus. The work was motivated by JF Prins where he observed the formation of diamond layers on copper followed by C^+ implantation into copper. This initial result suggested that it may be possible to generate single crystal diamond layers on single crystal copper. Subsequent efforts to reproduce this result failed. A unique end station was developed where a number of parameters could be altered during the implantation process. A series of carbon ion implantations were carried out on copper and copper-nickel (FCC) single crystals in this end station. The layers were characterised using initially Auger Electron Spectroscopy (AES), Low Energy Electron Diffraction (LEED) and later Raman Spectroscopy. During the early period of this study, the surface science equipment at the then Wits-Schonland Research Institute for Nuclear Sciences, was constantly giving problems. The time constraints on waiting for funds to be made available to repair the equipment, urged me to pursue alternative research endeavours and the results of this research is presented in chapter 4 and 5. The initial work will be investigated further in the future. Details of the end station are presented and the initial results of carbon layers generated in this end station are presented.

In chapter 4, a study of C^+ implantation into a type IIa (FCC single crystal) diamond using the cold implantation rapid annealing (CIRA) technique is reported. The Raman spectrum was recorded as a function of annealing temperature and C^+ ion dose. Defect peaks at 1450, 1498 and 1638 cm^{-1} appear in the Raman spectra, which have been previously considered to be unique to MeV implantation. The maximum energy of implantation used in this study was 170 keV. The peaks were monitored as a function of annealing temperature and ion dose. The annealing behaviour of the peaks were similar to those observed in the MeV implantation experiments. It is thus concluded that the defects that give rise to these peaks are related to the point-defect interactions that occur within the implantation regime and not to the implantation energy.

Understanding the nature of the defects that arise during the implantation annealing process, allows one to manipulate the implantation-annealing cycle, so as to generate defect structures that are useful in the fabrication of an active device in a diamond substrate. This is shown in chapter 5.

A p-type (type IIb, FCC crystal) diamond was implanted with either carbon or phosphorus ions using the cold implantation rapid annealing (CIRA) process. In each case, the energies and doses were chosen such that upon annealing, the implanted layer would act as an n-type electrode. The electroluminescence (EL) emitted from these carbon and phosphorus junctions, when biased in the forward direction, was compared as functions of annealing and diode temperatures. Typical luminescence bands such as those observed in cathodoluminescence (CL), in particular blue band A (2.90 eV) and green band (2.40 eV) were observed. Two bands centred around 2.06 and 4.0 eV were also observed for both the carbon and phosphorus junctions, while a band at 4.45 eV appeared only in the phosphorus implanted junction. This was the first time that the 4.45 eV band was observed in an electroluminescent junction.

Declaration

I declare that the work contained in this thesis is the original work of the author. Results of other workers in the field have been acknowledged when referred to in the scope of this study. The results of chapter 3 and 4 have been presented at an annual meeting of the South African Institute of Physics (SAIP, see page 101) and some of the results of chapter 4 have been used in a refereed paper [1]. The results of chapter 5 have been published in the proceedings of a refereed conference [2] and cited in [3, 4]. The study of chapter 3 is under further investigation.

Acknowledgements

Thanks to my supervisors Prof JF Prins and Prof TE Derry for all of their efforts especially in nagging me to write up my thesis. Inasmuch there were problems with the equipment (usually the case for experimental physics), your encouragement to pursue other facets of diamond research has enabled me to put together this body of work. This has given me an opportunity to explore a variety of experimental techniques and the knowledge I have gained will make an able scholar in the field.

To my colleagues Roger Nilen, Raymond Spits, Christoph Fischer, Zeblon Vilikazi, Ryan Maclear, Isaac Maachi, Elias Haddad, Mathew Bossenger, Clint Smallman, Daryl Rebuli, all of whom have moved on to greater callings then being a student, Thanks boys for the good times. To the many research projects which I have had the pleasure to be a part of and have gained an immense wealth of knowledge, thank you to all of the research team individuals for sharing your ideas with me. Some of this work is listed at the end of this thesis (pg 145-146).

To all of the staff at the Schonland Research Centre both academic, support and technical - I enjoyed being part of the friendly spirit we all shared at Schonland. A special thanks to Mik Rebak for his technical expertise in building the end station used in chapter 3 of this study - a work of art.

Thanks to Prof Comins for his useful discussions on Raman spectroscopy and the use of the Raman lab. I am grateful for the assistance of Michelle Nieuwoudt and Rudolph Erasmus for all of their help in accumulating the Raman data. To my colleagues at the Wits Physics Department, in particular Prof Giovanni Hearne - thanks for the laughs and the 24 hour nightshifts at Elletra (Trieste) and ALS (Berkely) synchrotron facilities - looking forward to being under more ‘pressure’. My other research colleague Dr Simon Connell - Thank you for your enthusiasm and energetic spirit.

Thanks to the musicians who share their talents and friendship with me - Jonathan Crossley, Peter Auret and Roland Moses.

To my mother Mrs Ruby Naidoo - you are a pillar of strength. My Sister Daphne for her unwavering support. To my wife Audrey - All your love and kindness makes me a better person. My extended family, Sombur's, Naidoo's, Narain's and Nathasha for being there for my family especially when I am away doing some experiment or jazzing it up.

This thesis is dedicated to the memory of Steve Biko whose words of wisdom raised my consciousness to face the future standing tall and my three daughters; Lisa-April, Mika Alysa and Kiara Alexi - for inspiration, to be your best.

Contents

1 Introduction **17**

1.1 Carbon and its allotropes 17

1.1.1 Diamond 20

1.1.2 The past, present and future of diamond 21

1.2 The scope of this thesis 25

2 Theory and Literature Review **27**

2.1 Introduction 27

2.2 Theory 27

2.2.1 Particle - Solid Interaction 27

2.2.2 Auger electron spectroscopy 30

2.2.3 Raman spectroscopy 33

2.2.4 Basic semiconductor principles 38

2.3 Literature Review 47

2.3.1 A brief background on ion implantation 47

2.3.2 Ion-Implantation into diamond 49

2.3.3 The CIRA process for doping diamond 51

2.3.4 Radiation damage in diamond 54

2.3.5 Auger spectroscopy identification of the allotropes of carbon . . 55

2.3.6 Raman Spectroscopy studies on the allotropes of carbon 55

3 Carbon overgrowths on FCC crystals after ion implantation **58**

3.1 Introduction 58

3.2 Background 59
3.3 Experimental considerations 63
3.3.1 Sample preparation 63
3.3.2 The end station 64
3.3.3 The implantation conditions 65
3.4 Analysis of the carbon overgrowths 66
3.5 Conclusions 68

4 Raman Studies on CIRA processed Diamonds 70
4.1 Introduction 70
4.2 Experimental considerations 71
4.3 Results 75
4.4 Discussion 101
4.5 Conclusions 111

5 Electroluminescence in ion implanted diamond 113
5.1 Introduction 113
5.2 Experimental procedure 114
5.3 Results 118
5.4 Discussion 123
5.5 Conclusions 129

List of Tables

3.1 Lattice constant and structure of certain select materials. 60

3.2 Implantation parameters used for the data presented in this chapter. In all of the cases above a bias voltage of -10.0 V and -15.0 V was applied to the filament and heater respectively. Take note that the gas pressure column is the pressure measured in the end station of the implanter and is not the pressure of the gas that is fed into the target holder end station. 66

4.1 Ion energies and doses used for the C^+ ion implantation in a type IIa diamond. According to the TRIM simulation program, the chosen ion energies and doses create a uniformly damaged layer to a maximum depth of $\approx 0.23\,\mu$m below the surface of the implanted face (see fig. 4.2). A moveable mask was first moved ≈ 1.0 mm down over the top edge of the diamond. This unimplanted region was used to monitor the virgin spectra after each annealing step. The remaining face was implanted with the dose fractions of step 1. The mask was then moved ≈ 1.5 mm down further over the diamond. The remaining exposed surface was implanted with the parameters of step 2. The mask was moved a further 1.5 mm and the remaining surface of the diamond was implanted with the dose fractions of step 3. The procedure continued until the diamond had been implanted with the dose fractions of step 4 and step 5 with the mask travelling 1.5 mm down after each step. Each dose column thus represents the dose fractions implanted at the various energies for regions 1 to 5. This procedure is schematically shown in fig. 4.1. 72

4.2 Summary of the implantation parameters and annealing cycles used in this Raman study. Note that the doses indicated for cycle D is the total implanted dose for the 5 regions on the diamond surface. The same sample holder was used as in cycles A, B and C to generate the five regions. The difference being for cycle D was the total dose of step 1 was implanted at 100 keV over the entire surface of the diamond after which the mask was adjusted downwards by 1.5 mm. The total dose of step 2 was then irradiated on the remaining surface of the diamond at 100 keV and the mask was again moved downwards by 1.5 mm. This process procedure was carried out up to step 5, keeping the energy at 100 keV, to complete the 5 regions of increasing dose as indicated in for cycle D. 76

5.1 Ion energies and doses used for the P^+ and C^+ diode junctions in type IIb diamond. According to the TRIM simulation program, the maximum depth traversed would be $\approx$0.16 μm for both ions. The multistep implantation sequence is achieved by implanting the dose fraction indicated at the highest energy and then moving up along the column to the next energy and implanting the dose fraction at that energy and so on. A total dose of 11.025×10^{15} ions/cm^2 was implanted for the C^+ junction, whereas the P^+ junction had a total dose of 3.15×10^{15} ions/cm^2. 115

List of Figures

1.1 Schematic representation of the graphite crystal structure [5]. 18

1.2 Schematic representation of the diamond FCC lattice structure [5]. 19

2.1 Schematic diagram of competing Auger and X-ray processes in an isolated atom(left) and a solid(right). For both cases the ionisation is at the core level and the Auger electron is emitted from the outer level for an isolated atom and the valence band in case of a solid. (After [6]). 31

2.2 Stokes line (after [7]). 37

2.3 Anti-Stokes line (after [7]). 37

2.4 Illustration of the energy bands of a solid with both donor and acceptor states within the forbidden band gap and a band gap energy E_g. The acceptor impurity level lies at an energy E_A above the filled valence band and the donor impurity level lies at an energy E_D below the empty conduction band. (After [7]). 41

2.5 Illustration of the formation of a $p-n$ junction and the corresponding band structure when equilibrium is attained. No electric current flows when the Fermi level is equalised on both sides. (After [8]) 44

2.6 Illustration of a $p-n$ junction in reverse bias mode(left) and forward bias(right). $\boldsymbol{J}$ indicates the direction of conventional current flow. (After [8]). 45

3.1 Schematic diagram of growth capsule for Cu and Cu-Ni targets used in this study (shown here in 2-D). 63

3.2 Auger spectra obtained for graphite, a synthetic Ib diamond and SiC samples. The arrows indicate one of the primary features that distinguishes sp^2 from sp^3 bonded carbon. The saddle on the lineshape shows a high energy shoulder for sp^3 bonded carbon (diamond and silicon carbide), while the graphite sample has this shoulder slightly lower. 67

3.3 Raman spectrum obtained for the carbon overlayer that was generated by the implantation conditions listed in table 3.1. The Raman spectrum reveals that the carbon has no diamond structure, but has the signatures for disordered carbon (D-band) and polycrystalline graphite (G-band). 68

3.4 Auger spectrum obtained for the carbon overlayer that was generated by the implantation conditions listed in table 3.1. The Auger lineshape reveals that the carbon has no diamond structure, but has the characteristic lineshape observed for sp^2 bonded carbon. 68

3.5 Raman spectrum obtained for the carbon overlayer that was generated by the implantation conditions listed in table 3.1. The Raman spectrum reveals that the carbon has no diamond structure. The additional Raman features that appear in the Raman spectrum of this sample is tentatively ascribed to carbon (graphite crucible used) that probably reacted with the Cu-Ni alloy during the melting since these features also appeared in the unimplanted Cu-Ni samples. It is well documented that carbon chemically reacts with Ni to form nickel carbides at low pressure [9–12]. 69

3.6 Auger spectrum obtained for the carbon overlayer that was generated by the implantation conditions listed in table 3.1. The Auger lineshape reveals that the carbon has no diamond structure. It is highly probable that most of carbon from the implantation process was removed by the hydrogen plasma if we assume that the carbon diffused to the surface of the implanted substrate to form sp^2 bonded carbon. 69

4.1 Schematic drawing of the specifically designed sample holder to achieve the five different implanted regions for the parameters outlined in table 4.1. The travelling mask could be adjusted downwards and the external adjustment was outside the vacuum system of the end station of the ion implanter. After each implantation step the mask was moved 1.5 mm down until five regions with five different doses were implanted on the face of the type IIa diamond. The shaded regions indicate the different regions with the darkest region symbolizing the area that received the highest dose. 73

4.2 TRIM simulation of the damage profile for the implantation parameters used in cycles A, B and C in this study. The damage distribution is spread over a width of $\approx 0.23\,\mu$m. The dashed line is drawn at a vacancy density of $1 \times 10^{22}\,\mathrm{vac/cm^3}$. 77

4.3 TRIM simulation of the damage profile for the implantation parameters used in cycle D (100 keV). The damage distribution is spread over a width of $\approx 0.15\,\mu$m. According to TRIM the damage distribution reaches a maximum near $\approx 0.12\,\mu$m. The average vacancy density for regions 1-2 is below $1 \times 10^{22}\,\mathrm{vac/cm^3}$. For region 3 it is mostly below $1 \times 10^{22}\,\mathrm{vac/cm^3}$, whereas regions 4 and 5 have an average vacancy that is primarily above $1 \times 10^{22}\,\mathrm{vac/cm^3}$. . 78

4.4 Raman spectra obtained for the unimplanted diamond used in this study. The typical diamond line centred at $1331\,\mathrm{cm^{-1}}$ with a line width $2.9\,\mathrm{cm^{-1}}$ was observed after each implantation-annealing cycle. 79

4.5 Raman spectra obtained for the implanted diamond in cycle A - region 1. The implanted dose is less than D_c. Evidence of the $1638\,\mathrm{cm^{-1}}$ peak is present after annealing at 650 °C while the $1498\,\mathrm{cm^{-1}}$ peak is present but not well defined after annealing at 800 °C. No Raman active defect peaks are visible after annealing at 950 °C. 80

4.6 Raman spectra obtained for the implanted diamond in cycle A - region 2. The implanted dose is less than D_c. Evidence of the 1638 cm^{-1} peak and the 1498 cm^{-1} peak is present after annealing at 500 °C. No Raman active defect peaks are clearly visible after annealing at 950 °C. 81

4.7 Raman spectra obtained for the implanted diamond in cycle A - region 3. The implanted dose is less than D_c. Evidence of the 1638 cm^{-1} peak and the 1498 cm^{-1} peak is present after annealing at 500 °C. No Raman active defect peaks are clearly visible after annealing at 950 °C. 82

4.8 Raman spectra obtained for the implanted diamond in cycle A - region 4. The implanted dose is greater than D_c. Evidence of the 1638 cm^{-1} peak is present after annealing at 500 °C while the 1498 cm^{-1} peak is more clearly defined after the 650 °C anneal. The 1498 cm^{-1} defect peak is now still present after annealing at 950 °C. No Raman active defect peaks are present after annealing at 1100 °C. 83

4.9 Raman spectra obtained for the implanted diamond in cycle A - region 5. The implanted dose is greater than D_c. No evidence of the 1638 cm^{-1} peak and the 1498 cm^{-1} peak is present after annealing at 500 °C. The spectra are dominated by a broad band centred around 1550-1580 cm^{-1} which indicates that the implanted - annealed layer consists of disordered graphite. The diamond line is barely visible after annealing at 800 °C. 84

4.10 Raman spectra obtained for the implanted diamond in cycle B - region 1. The implanted dose is less than D_c. The 1638 cm^{-1} peak is present after annealing at RT while the 1498 cm^{-1} peak is present after annealing at 500 °C. No Raman active defect peaks are clearly visible after annealing at 950 °C. The defect peaks labelled (g) and (h) after annealing at 1400 °C are most probably due to contamination from the annealing crucible which was made of graphite. They also appear in the virgin spectra after annealing. (see fig 4.15 cycle C region 1 and 2 at labells (d), (e), (f) and (g)). 85

4.11 Raman spectra obtained for the implanted diamond in cycle B - region 2. The implanted dose is less than D_c. Evidence of the 1638 cm^{-1} peak is present after annealing at RT up to anneals at 800 °C and the 1498 cm^{-1} peak is present after annealing at 500 °C up to anneals at 950 °C. No Raman active defect peaks are clearly visible after annealing at 1100 °C. 86
4.12 Raman spectra obtained for the implanted diamond in cycle B - region 3. The implanted dose is less than D_c. Evidence of the 1638 cm^{-1} peak is present after annealing at RT up to anneals at 800 °C and the 1498 cm^{-1} peak is present after annealing at 500 °C up to anneals at 950 °C. No Raman active defect peaks are clearly visible after annealing at 1100 °C. 87
4.13 Raman spectra obtained for the implanted diamond in cycle B - region 4. The implanted dose is greater than D_c. Evidence of the 1638 cm^{-1} peak is present after annealing at RT up to anneals at 800 °C and the 1498 cm^{-1} peak is barely present after annealing at 500 °C but clearer after annealing at 650 °C up to anneals at 950 °C. No Raman active defect peaks are clearly visible after annealing at 1100 °C. 88
4.14 Raman spectra obtained for the implanted diamond in cycle B - region 5. The implanted dose is greater than D_c. No evidence of the 1638 cm^{-1} peak and the 1498 cm^{-1} peak is present after annealing at 500 °C. The spectra are dominated by a broad band centred around 1550-1580 cm^{-1} which indicates that the implanted - annealed layer consists of disordered graphite. The diamond line is barely visible after annealing at 800 °C. 89
4.15 Raman spectra obtained for the implanted diamond in cycle C - region 1. The implanted dose is less than D_c. The 1638 cm^{-1} peak is present after the RT implant and anneals up to 800 °C. The 1498 cm^{-1} peak is present after annealing at 500 °C up to anneals to 950 °C. The defect peaks labelled (d), (e), (f) and (g) are assigned to contamination from the annealing crucible. Note the defect labelled (d) was measured from the unimplanted diamond (virgin-800 °C) after annealing at 800 °C. 90

4.16 Raman spectra obtained for the implanted diamond in cycle C - region 2. The implanted dose is less than D_c. The 1638 cm^{-1} peak is present after the RT implant and anneals up to 800 °C. The 1498 cm^{-1} peak is present after annealing at 500 °C up to anneals to 950 °C. The defect peaks at 1620 cm^{-1} and 1680 cm^{-1} after the 950 °C are assigned to contamination from the annealing crucible. The same conclusion is made for the Raman shift measured at 1530 cm^{-1} in the virgin spectrum after annealing at 1400 °C. 91

4.17 Raman spectra obtained for the implanted diamond in cycle C - region 3. The implanted dose is less than D_c. The 1638 cm^{-1} peak is present after the RT implant and anneals up to 800 °C. The 1498 cm^{-1} peak is present after annealing at 500 °C up to anneals to 950 °C. 92

4.18 Raman spectra obtained for the implanted diamond in cycle C - region 4. The implanted dose is greater than D_c. The 1638 cm^{-1} peak is present after the RT implant and anneals up to 800 °C. The 1498 cm^{-1} peak is present after annealing at 500 °C up to anneals to 950 °C. The defect peaks at 1580 cm^{-1} and 1620 cm^{-1} after the 1400 °C anneal are assigned to contamination from the annealing crucible. 93

4.19 Raman spectra obtained for the implanted diamond in cycle C - region 5. The implanted dose is greater than D_c. No evidence of the 1638 cm^{-1} peak and the 1498 cm^{-1} peak is present after the RT implant. The spectra are dominated by a broad band centred around 1550-1580 cm^{-1} and 1360 cm^{-1} which indicates that the implanted - annealed layer consists primarily of disordered graphite. 94

4.20 Raman spectra obtained for the implanted diamond in cycle D - region 1. The implanted dose is less than D_c. The 1638 cm^{-1} peak is present after the RT implant and anneals up to 800 °C. The 1498 cm^{-1} peak is present after annealing at 500 °C up to anneals to 950 °C. The broad defect band at 1480 cm^{-1} after the 1100 °C anneal is most probably due to contamination from the annealing crucible. The same can be said for the defect band at 1660 cm^{-1} after the 1400 °C anneal. 96

4.21 Raman spectra obtained for the implanted diamond in cycle D - region 2. The implanted dose is less than D_c. The 1638 cm^{-1} peak is present after the RT implant and anneals up to 800 °C. The 1498 cm^{-1} peak is present after annealing at 300 °C (not well defined) up to anneals to 950 °C. The sharp defect band labelled (c) at 1210 cm^{-1} after the 1400 °C anneal is tentatively assigned to contamination from the annealing crucible during the annealing stage at this high temperature. 97

4.22 Raman spectra obtained for the implanted diamond in cycle D - region 3. The implanted dose is less than D_c. The 1638 cm^{-1} peak is present after the RT implant and anneals up to 800 °C. The 1498 cm^{-1} peak is present after annealing at 300 °C up to anneals to 950 °C. The defect band labelled (a) at 1250 cm^{-1} after the 1400 °C anneal is tentatively assigned to contamination from the annealing crucible. Similar defects appear in the virgin spectra after high temperature annealing as shown earlier in other spectra. 98

4.23 Raman spectra obtained for the implanted diamond in cycle D - region 4. The implanted dose is greater than D_c. No evidence of the 1638 cm^{-1} peak and the 1498 cm^{-1} peak is present after the RT implant. The spectra are dominated by broad bands centred around 1550-1580 cm^{-1} and 1360 cm^{-1} which indicates that the implanted - annealed layer consists primarily of disordered graphite. It is interesting to note that in these spectra there is strong evidence of the diamond peak in spite the presence of a broad disordered graphite band even after annealing at high temperatures. The diamond line in this case most probably arises from the unimplanted layer above the graphitic layer recalling that for cycle D the implanted dose was performed at a single energy. 99

4.24 Raman spectra obtained for the implanted diamond in cycle D - region 5. The implanted dose is greater than D_c. No evidence of the 1638 cm^{-1} peak and the 1498 cm^{-1} peak is present after the RT implant. The spectra are dominated by a broad band centred around 1550-1580 cm^{-1} which indicates that the implanted - annealed layer consists primarily of disordered graphite. 100

4.25 Annealing behaviour of the 1498 and 1638 cm^{-1} bands for cycle A and B. The Full Width at Half Maximum (FWHM) was obtained for the different peaks by fitting a Lorentzian function over the appropriate peaks in the Raman spectra. 101

4.26 Annealing behaviour of the 1498 and 1638 cm^{-1} bands for cycle C and D. The Full Width at Half Maximum (FWHM) was obtained for the different peaks by fitting a Lorentzian function over the appropriate peaks in the Raman spectra. The data points labelled with * in cycle C for the 1638 cm^{-1} are those where the band was initially not centred around 1638 cm^{-1}, but appeared as a broad band centred around 1630 cm^{-1}. Note that cycle D had no additional features in regions 4 and 5 at any of the annealing temperatures, but rather broad bands centred around 1580 cm^{-1} and 1360 cm^{-1}. 102

4.27 Raman spectra collected during cycle D after annealing at 650 °C (left figure) for 1 hour and thereafter at 800 °C (right figure) for 1 hour. The 1638 cm^{-1} and the 1658 cm^{-1} peaks are clearly visible as well as the defect band centred around 1450 cm^{-1}. Note also the shift to higher wavenumbers for the 1450 and 1498 cm^{-1} defect bands afer the 800 °C anneal. 104
4.28 1498 cm^{-1} peak position versus annealing temperature. The behaviour for cycle A indicates that the tensile stress in is substantially less after a CIRA process with the dose implanted over a wide width. 106
4.29 1498 cm^{-1} peak position versus TRIM damage. 107
4.30 Peak width plotted against peak position for cycle C. The lines joining the points are for guiding the eye. A linear approximation can be deduced between the two quantities. The same is reported for MeV implanted diamond [13]. 108

5.1 Device set-up (not drawn to scale). The above configuration was clamped in a specifically designed holder to measure the IV characteristics, and thereafter placed in a chamber with a monochromator assembly and photomultiplier tube so that the light output could be recorded. 116
5.2 Damage and range profiles for the P^+ junction as obtained from TRIM98 with $E_d = 45$ eV. The doses and energies used are shown in table 5.1. A similar profile is obtained for the C^+ implanted junction. Based on our observations of chapter 4, we could expect that implanted layer above the dashed line (close to 1×10^{22} vac/cm^3) will form a graphitic layer which will be etched away when boiled in an oxidising acid solution. The region demarcated A is within a rough approximation the layer that is removed by boiling in the hot acid solution. The shape of the profiles suggests why the diodes are considered graded np-junctions as argued in the text. 117

5.3 Typical IV curves obtained for the diode junctions. The legend describes the IV curve measured after annealing the diamond at that temperature. All measurements were done at room temperature. No conclusions are made with respect to the current density since the device set-up did not yield the same active area for different measurements. 119

5.4 EL spectra measured for the C^+ junction under different foward voltages and diode operating temperatures. The peak assignment, peak energy, annealed temperature, bias voltage and diode temperature are listed alongside each of the peaks in the spectra shown. Since the active area of the junctions were not the same for different measurements, no conclusions were made with respect to the measured intensities. 120

5.5 EL spectra measured for the P^+ junction under different foward voltages and diode operating temperatures. The peak assignment, peak energy, annealed temperature, bias voltage and diode temperature are listed alongside each of the peaks in the spectra shown. Since the active area of the junctions were not the same for different measurements, no conclusions were made with respect to the measured intensities. 121

5.6 EL spectra measured following an anneal at 700 °C. The P^+ spectrum was recorded at 190 °C at a forward bias of 40 V. For the C^+ junction, a forward bias of 35 V at 112 °C was used. Both junctions show the generation of Green Band A luminescence at high temperatures. Similar spectra, (as can be seen in fig 5.4 and 5.5) at high diode temperatures, are obtained following the anneals at 500 and 900 °C. Since the active area of the junctions were not the same for different measurements, no conclusions were made with respect to the measured intensities. 122

5.7 EL spectra measured for the C^+ and P^+ junctions after annealing at 1100 °C. The spectrum obtained for the C^+ junction was at a forward bias of 30 V and a temperature of 67 °C. The P^+ spectrum was recorded at a forward bias of 40 V at 111 °C. There is no indication of the 2.4 eV band even at a high diode temperature. The 2.06 eV band and 4 eV bands were prominent after the 1100 °C anneal. No conclusions are made with respect to the emitted intensities. 127

5.8 Electroluminescence spectra obtained for the C^+ and P^+ diode junctions after the anneals at 1300 and 1500 °C. Both junctions emitted blue band A (2.9 eV), while only the P+ junction had a UV emission centred around 4.45 eV. The C^+ (1300 °C) and C^+ (1500 °C) spectra were recorded at a forward bias of 40 and 45 V, while the diode operating temperature was at -34 and -45 °C respectively. The P^+ (1300 °C) and P^+ (1500 °C) spectra were recorded at a forward bias of 40 and 35 V, while the diode operating temperature was at -39 and 22 °C respectively. There are no indications of the 2.06 and 4 eV band nor could the 2.4 eV band be generated after the high annealing cycles. No conclusions are inferred from the emitted intensities. . 128

5.9 Recombination between activated phosphorus and boron (DAP recombination) can be used to explain the origin of the 4.45 eV observed in the EL diodes fabricated in this study. 130

Chapter 1

Introduction

1.1 Carbon and its allotropes

The carbon atom has a ground state configuration of $1s^2$, $2s^2$, $2p^2$. The ability of the s and p orbitals to hybridize to what are commonly referred to as sp, sp^2 and sp^3 hybrid orbitals allows the carbon atom to bond chemically in predominantly covalent configurations in a host of ways. This has led to the natural occurrence and discovery of a myriad of gases, liquids and solids, in which carbon is the central constituent, and many of which are congruent to our existence and is the basis of organic chemistry. We will focus primarily on the solid state allotropes of carbon.

In nature there are three common forms of solid carbon ie. coal, graphite and diamond. Coal has many impurities and the carbon atoms have no long range order and it is an amorphous carbonaceous material. Graphite and diamond are two materials that occur naturally in a crystalline form.

The atomic arrangement of graphite is shown in fig. 1.1. The structure is easily described as a two dimensional net, with each mesh of the net being a hexagon. The carbon-carbon atom separation is 0.141 nm between the neighbouring atoms in the hexagons, while the planes are about 0.34 nm apart. The lattice parameters are a_o and c with 4 atoms in the unit cell. The space group is labelled as C6/mmc (C-centered

hexagonal). This separation between the planes is too large for any interplanar bonding but is sufficient to form the structure of the graphite lattice. The strong bonding within the planes is a result of sp^2 bonding between the carbon atoms.

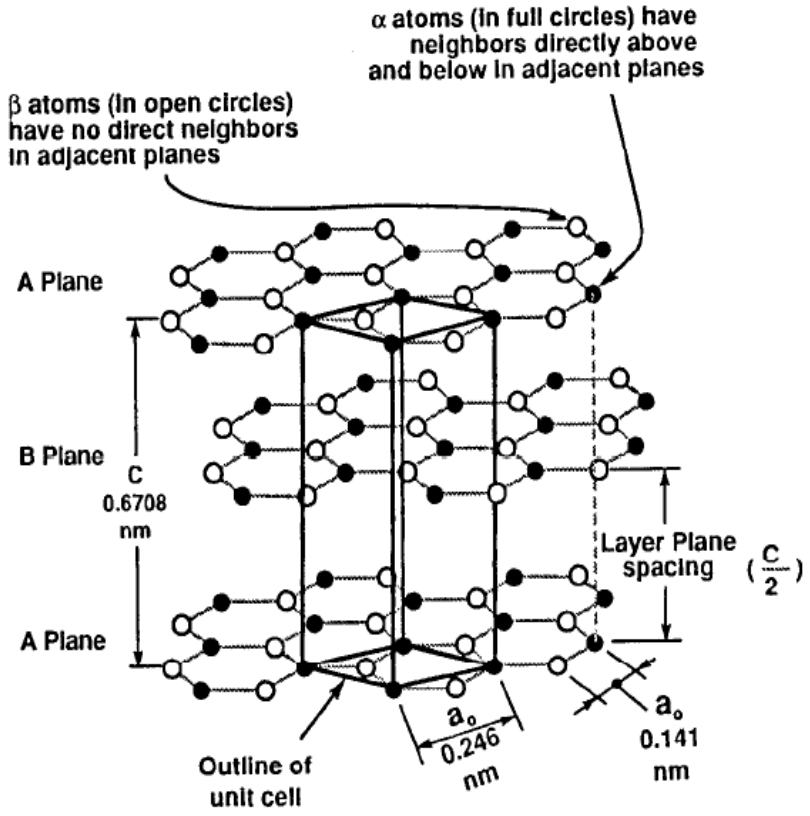


Figure 1.1: Schematic representation of the graphite crystal structure [5].

The diamond lattice has its carbon atoms 0.154 nm apart in a three dimensional puckered hexagonal structure. This tetrahedral bonding arrangement is a result of the sp^3 bonding configuration of the carbon atoms. A more natural perspective of the geometric configuration is to view the crystal as two inter-penetrating face centered cubic lattices (FCC)as shown in fig. 1.2. The length of the edge of the cube face in

the unit cell is 0.356 nm. There are 8 atoms in the unit cell and the space group is designated as Fd3m (face-centered cubic).

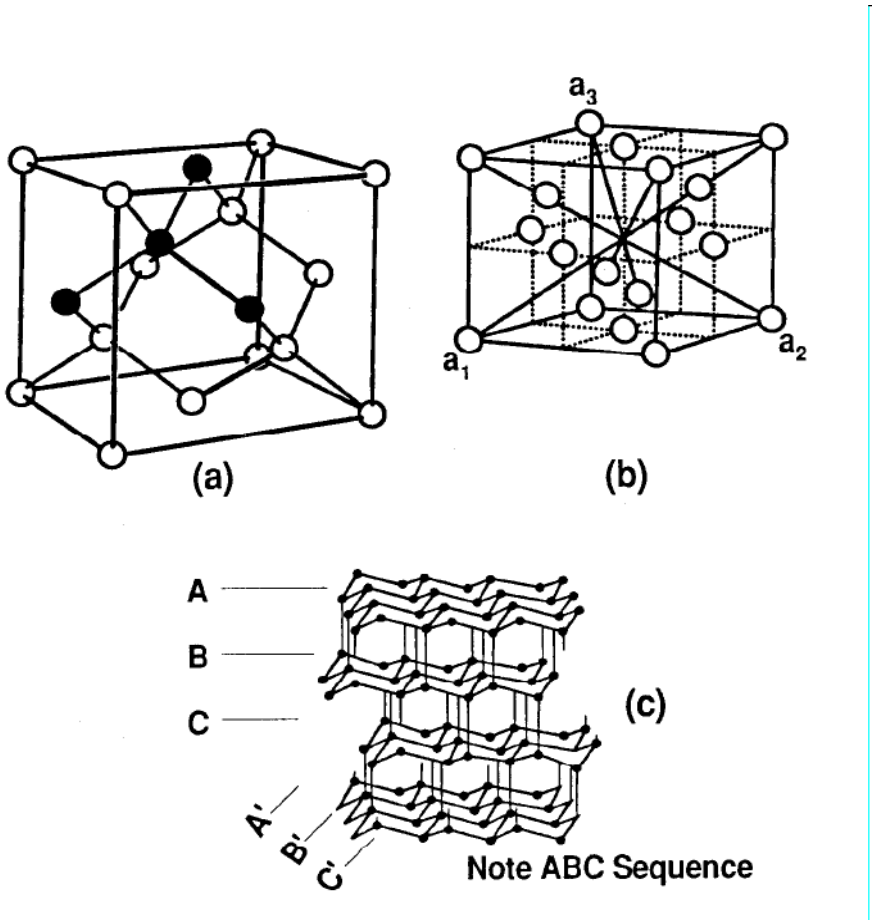


Figure 1.2: Schematic representation of the diamond FCC lattice structure [5].

Inasmuch as the geometrical structures of graphite and diamond are built from carbon atoms, the optical and electrical properties differ significantly. Pure diamond is transparent, while graphite is opaque. Graphite is a conductor while diamond with a band gap of 5.47 eV, makes it an ideal insulator. The density of diamond is 3.51 g.cm^{-3} and that of graphite is 2.2 g.cm^{-3} [7]. It is amazing that the basis of these differences is contained in the bonding configurations discussed earlier.

1.1.1 Diamond

It is with the diamond gem that humankind has had a fascination. It has a natural beauty that is exploited for cosmetic purposes. The hardness and abrasive properties of the crystal are useful in cutting tools. The exceptionally high thermal conductivity ($20\,\mathrm{W.cm^{-1}.K^{-1}}$ for high quality natural type IIa diamonds) of the crystal has been successfully utilised as heat sinks in high temperature environments [14]. Diamond is also chemically inert and impervious to even the most harsh chemical environments. When it was discovered that the diamond lattice was made up of carbon atoms, a research endeavour ensued that demonstrated that the graphitic carbon could be converted into the diamond lattice. The early attempts by Gannal, Despretz, Lionnet, Boismenu, Rousseau, Marsden and others were either controversial or proved unsuccessful. When it was realised that diamonds that occurred naturally were formed deep in the earth's crust and transported to the surface by volcanic eruptions, this paved the way for the idea that synthetic diamond could be derived by a high pressure-high temperature (HPHT) process in the lab, similar to the conditions in which they were formed deep below the earth's surface. Moissan and Hannay were among the first pioneers to use the process of HPHT of growing 'synthetic' diamond, but their claims of successfully synthesizing diamond in this manner was proved false. Many others followed with most failing or making fraudulent claims. This fascinating history and other interesting details can be found in [15].

The science of thermodynamics later laid the theory which could be applied in the laboratory to synthesize diamonds by HPHT. The General Electric Research Laboratory, led by Nerad, were the first successful company to announce the synthesis of diamonds by HPHT [16]. The strides made in technology and the understanding of the process has developed the process into a highly competitive industry. Most of the crystals generated by HPHT are used in cutting, drilling and abrasive tools while the 'natural' crystals are first considered for cosmetic applications. Natural and synthetic diamond are classified into a variety of classes dependent on both their purity and

impurity concentration. These details are aptly outlined in [14]. In this body of work a natural type IIa diamond was used in the study of chapter 4. Type IIa diamonds are the highest quality gem diamonds found in nature and contain extremely low levels of nitrogen. A natural type IIb diamond was used in the study of chapter 5. Type IIb diamonds are also high in quality and morphology, with little or no nitrogen content, but contains boron as its major impurity.

The highly directional covalent bonding as a result of the sp^3 hybridisation makes diamond an insulator. The band gap of diamond has been measured to be at 5.47 eV at room temperature. With its high thermal conductivity and high electron and hole mobilities, diamond thus avails itself as an ideal candidate for semiconductor applications [17]. The crystal structure is also the prototype for the semiconductor materials silicon and germanium. Nature provided the first semiconducting diamond crystals where substitutional boron was the acceptor impurity in natural type IIb diamonds. With the advent of growing diamond at low pressure by a process referred to as plasma assisted chemical vapour deposition (PACVD or commonly CVD), the realisation of growing large area diamond wafers for semiconductor processing is more apparent. Prior to this era of research, it was demonstrated that ion implantation provided a suitable route to introducing dopants into the diamond lattice.

1.1.2 The past, present and future of diamond

In spite of diamond's promise as an opto-electronic medium, diamond electronics has not lived up to its full potential. The problems encountered have been difficult to surmount. The two main hurdles have been the ability to grow high quality diamond layers by heteroepitaxy and the introduction of suitable dopants for n and p-type conductivity. The layers have to have a large area with a minimal amount of defects. CVD layers by hetroepitaxy have grown in area over the past years, but the quality of the layers has not improved as fast. It has been shown that the substrate on which the layers are grown is critical to the nature of the layers. At present silicon and silicon carbide are the two substrates on which reasonable diamond layers are being grown via

the methods of hot filament CVD and micro-wave plasma CVD. The layers generated by these methods are polycrystalline and have too many defects for semiconductor application. Part of the problem has been the lattice mismatch of the substrate to the diamond lattice which inevitably leads to multi oriented growth. The ability to introduce dopants during the deposition process (heteroepitaxial growth) has led to the incorporation of boron and phosphorus as dopants into the polycrystalline lattice, but the fact of the growth being unoriented, with other defects, has meant that the layers are not suitable for semiconductor application.

In the last decade advances in HPHT technology has been able to produce high quality synthetic type Ib, IIa, IIb and many other coloured diamonds which have become available commercially for their cosmetic beauty. The crystallinity and morphology of these diamonds are in fact better than most high quality natural diamonds. These advances have perked the interest in the development of synthetic diamond as undulators and monochromators in the next generation synchrotron light sources and free electron lasers [18, 19]. Present challenges within these applications are the processing technologies of the diamond surface particularly in the <111> direction and the preparation of high quality thin crystals with larger surface areas which would require larger crystals to be generated by HPHT processes. The high quality HPHT diamonds have also been used to grow high quality CVD diamond by homoepitaxy. Boron doped layers grown in this manner have carrier mobilities far exceeding those measured in natural IIb diamond [20, 21]. Schottky type diodes (vertical configuration) devised on these high quality diamond layers showed a switching voltage of 2.0 V and a voltage blocking capability of -2.5 kV [21]. Based on these developments it is apparent that in spite of the drawbacks experienced in the heteroepitaxial growth of diamond, more effort should be focussed in this research area, so that large area single crystal diamond could be grown.

Ion implantation has proved to be successful in creating p-type layers in natural IIa single crystals with hole mobilities usually lower but sometimes comparable to

those measured in natural IIb crystals [22, 23]. n-type behaviour has been reported using phosphorus [24], oxygen [25] and nitrogen [26] implantation, but the layers are highly compensated by the damage-related acceptor and donor states. The highly compensated layers and low mobilities measured in ion implanted diamond is due to the radiation damage introduced by the implantation process. Diamond will relax to its allotrope graphite when heated above 1800 °C in air. The implanted layer will collapse to graphite upon annealing in vacuum or an inert gas atmosphere when the implanted density of ions exceed a critical damage density. Hence it does not provide an avenue like its counterpart silicon in annealing the crystal near its melting point to reduce the radiation damage. One has to be judicious in the choice of implantation energies, temperature, dose, dose rate and consequent annealing temperature to obtain a desired result. Numerous approaches have been employed in an effort to counteract the effects of radiation damage as well as a host of theoretical models to explain the nature of the damage. The reader is pointed to the work contained in [1, 27–42] and references therein. It is clear from these publications that we have come a long way but there are also some unresolved issues. Aspects of these publications will be pointed out where relevant to the scope of this work.

Within the body of literature on diamond electronics it is accepted by both experimental and theoretical modelling that boron is an acceptor when it is in a substitutional lattice site in diamond, while phosphorus and nitrogen are both substitutional donor type impurities. Particular emphasis is focussed on boron and phosphorus since both these impurities can be incorporated in the growth chambers of CVD systems. The substitutional boron acceptor level is 0.37 eV [17, 43, 44], above the valence band while phosphorus has a donor level at 0.63 eV [31, 45–48] below the conduction band when in a substituional lattice site. In spite of the relatively deep acceptor and donor levels of these impurities effective device construction has been demonstrated for both implanted and CVD doped diamond [29, 49–51]. Apart from the conventional substitutional dopants, molecular dopants, interstitial type dopants and impurity complexes coupled with vacancies may provide an alternative for shallower type dopants. The-

oretical calculations and experimental evidence for alternate shallower dopants have been suggested in [24, 26, 52–56].

Understanding the surfaces of diamond has also been an area of intense research in the past three decades. The nature of how the surface of diamond reconstructs in different environments has been a key in understanding diamond nucleation by heteroepitaxy. It has been found that when diamond surfaces are exposed to different plasma treatments then diamond exhibits the property of negative electron affinity (NEA) or positive electron affinity (PEA). This attribute has also been found to be possible in the polycrystalline layers grown by CVD methods. Surface reconstruction has also important consequences for the formation of Schottky type devices on diamond. The hydrogenated surface that has been found to contribute favourably to the formation of an NEA surface and oxygen plasma treatment induces Schottky switching behaviour for certain metallic depositions on diamond surfaces. The reports covered in [57–67] cover these aspects. The ability to incorporate cold cathode devices which is preempted by NEA surfaces on diamond layers will open new frontiers of technology and research.

In the last decade quantum information processing (QIP), quantum cryptography and quantum computing has received much attention in scientific literature. Diamond has been touted as a possible source of single photons for the development of QIP. Particular focus has been given to the nitrogen-vacancy and the nickel-nitrogen (NE8) center. Because diamond has such strong covalent bonds and low spin orbit interaction, this leads to long lifetimes for spin states. Coupled with its high Debye temperature will mean high temperature operation for quantum devices fabricated in diamond. These developments are well documented in [5, 68–72]. It has also been reported that a boron doped diamond structure exhibited superconductivity at transition temperature of 4 K [73]. This will only probably be of academic interest.

Based on the developments reported in [20, 21] it would appear that the dawn of diamond electronics is finally upon us. As the 21st century unfolds we can be sure that

diamond technology will be in the forefront of new ideas in the opto-electronic industry [74], QIP and in the beam optics of the high intensity hard X-ray synchrotron sources and free electron lasers.

1.2 The scope of this thesis

The research output of this thesis considered the ion beam modification of fcc lattices with diamond being the primary lattice. In chapter 4 we consider the radiation damage induced by keV implantation into the diamond crystal. It is pivotal to gauge an understanding on the defect structures created during the implantation process, how they anneal, and their effect on acceptor and donor impurities if any. The point defects and extended defects created during the implantation-annealing process can be both detrimental and useful in the ion implanted layers. Raman spectroscopy was used to monitor the radiation damage as a function of annealing temperature. The results are compared to MeV implanted diamond layers and the differences in the results obtained are discussed.

In the final section we use the radiation damage to create a minority carrier injection junction in a natural IIb diamond. With this experiment electron injection junctions using carbon and phosphorus ion implantation were created. The electroluminescence (EL) emitted from the diode junctions was monitored, and compared with that observed in cathodoluminescence (CL). Distinct differences were observed for the carbon and phosphorus junctions. The luminescent bands observed were correlated to possible defect structures that give rise to the electron bands that generate the recombination centers for the light emitting electron de-excitations.

We first consider the initial investigation results obtained on carbon ion implanted structures grown on single crystal copper and copper-nickel crystals. Copper has a lattice constant of 3.62 Å compared to that of diamond with a lattice constant of 3.52 Å. Carbon is not miscible in copper, and will not form any carbidic structures or

stable chemical bonds between itself and the copper matrix. Carbon implanted into the copper and copper-nickel crystals will diffuse out towards the surface and form carbon based structures on the surface. Earlier experiments and work by other researchers have revealed different results. Reports that diamond layers could be generated were not verified and subsequent experimenters have revealed other interesting carbon structures but not diamond. The work presented here concerns layers grown in a unique end station where the implanted carbon ions were accelerated into the metal in the presence of a plasma created near the surface of the implanted crystal. A variety of parameters could be changed and each led to the creation of different structures at the surface of the implanted crystal. This is a work in progress which will attempt to find a set of surface conditions that would deliver a network of sp^3 bonded carbon atoms on the copper or copper-nickel surface. This may lead to a seeding process that will generate large area single crystal diamond using CVD processes. Auger electron spectroscopy (AES), low energy electron diffraction (LEED) and Raman spectroscopy were used to identify the surface structures that formed at the surfaces of the copper and copper nickel-crystals.

Chapter 2

Theory and Literature Review

2.1 Introduction

A brief discussion on the theoretical background of the experimental and analytical processes employed in this study is presented. We discuss in particular ion implantation, Auger electron spectroscopy, Raman scattering spectroscopy and some basic semiconductor principles.

2.2 Theory

2.2.1 Particle - Solid Interaction

An ion accelerated towards the surface of a solid target will pass into the target, where it loses energy by interacting with the atoms and electrons of the host material, and then eventually come to rest within the matrix of the solid or pass through it, depending whether the incident energy was sufficiently high or on the thickness of the target. In this study the incident ion energy was in the keV range and the materials substantially thick so that all the ions would stop within the solid targets used. The depth at which the penetrating ions will come to rest is dependent on the incident ion energy, the mass of the accelerated ion and the density of the target material.

The interactions the projectile undergoes in its path during its passage through the target material, prior to coming to rest can be described by three processes, electronic scattering, nuclear scattering and nuclear reactions. Nuclear scattering is an elastic scattering process between the target atom and the incident ion in which both the nuclear states of the target atom and scattered ion remain unaltered. The process is described by an interatomic interaction potential where the dominant term is given by the Coulomb interaction between the two nuclei. Nuclear reaction mechanisms and electronic scattering are inelastic processes where the interaction leads to a change in the nuclear state and electronic states of the bombarding atoms, respectively. Each of these scattering events contributes to the energy loss of the incident ion.

The cross sections for nuclear reactions are significantly smaller than those for electronic scattering and nuclear scattering. Within the energy regime employed in this study nuclear reactions do not significantly affect the motion of the ion through the substrate. The energy loss of the ion due to electronic and nuclear scattering can be treated as two statistically independant processes. An in depth theoretical description of the kinematic factors, cross sections and other pertinent factors to describe the interaction mechanisms that lead to the energy losses due to electronic scattering and nuclear scattering can be obtained from the text in [75]. For the purpose of this study it will suffice to write the general expressions that describe the range for an ion of incident energy E_i entering an amorphous solid. Within the theoretical descriptions for the energy losses it is evident that nuclear scattering processes are dominant at lower energies while electronic scattering events have a higher cross section at higher energies. The energy losses that occur owing to electronic scattering are described in the electronic loss term, $\left(\frac{dE}{dt}\right)_e$, where dE is the mean energy loss in a differentially small target thickness dt. Similarly, nuclear scattering leads to a nuclear loss term, $\left(\frac{dE}{dt}\right)_n$. The rate of the energy loss by nuclear plus electronic stopping is $\left(\frac{dE}{dt}\right)$ and is called the stopping power. If we consider electronic stopping and nuclear stopping to

be independant processes then

$$\frac{dE}{dt} = \left(\frac{dE}{dt}\right)_n + \left(\frac{dE}{dt}\right)_e \tag{2.1}$$

The projected ion range, R_p is obtained by integrating (2.1),

$$R_p = \int_0^{E_i} \frac{dE}{\left(\frac{dE}{dt}\right)_n + \left(\frac{dE}{dt}\right)_e} \tag{2.2}$$

Close to R_p, the nuclear stopping dominates the energy loss mechanism and it is near this depth where most of the host lattice atoms are dislodged from their substitutional sites. A displaced atom in turn can have gained sufficient energy from the incident ion and may knock-on other host atoms from their lattice positions. This cascading process of recoiling target atoms continues until neither the incident ion nor the recoiling atoms have sufficient energy to eject any other host atoms from their lattice sites. Since the two-body collisions of the ions with the target atoms are statistically independent this leads to an approximately gaussian shape for the final distribution of the incident ions in the range R_p. The standard deviation ΔR_p is known as the longitudinal ion straggling. Suitable computational models are available which calculate the final ion distribution and damage as a result of the ion irradiation process. We used TRIM92 (The Transport of Ions in Matter) in this study [75].

TRIM makes the following assumptions in its calculations. It assumes that the incoming ion will impact on a crystalline solid in a random direction, thus excluding any channelling of ions. It does not take into account any phase changes that occur during the irradiation process. It cannot account for any dynamical annealing or thermal annealing if the crystal is implanted at higher temperatures. Most of these assumptions are derived from the theoretical descriptions employed to describe the ion-solid interaction. It is apparent that the process is a highly sophisticated many-body interaction and thus simplified theoretical models are used in the computational codes.

The relevance of the ion-solid interaction in the purpose of this study was to observe

the effects of the radiation damage caused by the irradiation process and the clustering and new phase formation of carbonaceous species in the solid materials implanted. The ion-solid interaction also lends itself as a suitable tool for analysis such as Rutherford Backscattering analysis (RBS), Nuclear Reaction Analysis (NRA), Ion channelling studies in crystalline materials, Proton Induced X-ray Emission (PIXE), etc. These analytical techniques take advantage of the interactions or excitations that take place as a result of the nuclear and electronic scattering in the solid. These excitations and interactions result in characteristic X-rays, gamma rays or elastically backscattered ions which assist in identifying properties of the excited matrix. They form part of a large study known as Ion Beam Analysis which has been successful in assessing various properties of materials at an atomic level.

2.2.2 Auger electron spectroscopy

Apart from the heavy ions such as protons and alpha particles which are utilised for ion beam analysis of solids, we have at our disposal the use of electrons, X-ray photons and visible light photons to study the properties of materials. The use of low energy particles such as electrons is useful since they do not induce any significant damage to the matrix or the surface of the solid being investigated. The common techniques employed to study the chemical properties of the surfaces of solid materials are electron spectroscopy for chemical analysis (ESCA) also referred to as X-ray photoelectron spectroscopy (XPS) and Auger electron spectroscopy (AES), while low energy electron diffraction (LEED) is used to determine the crystal structure near the surface. Each of these techniques deduces information on the near surface properties of materials.

The Auger effect for an isolated atom is shown in fig. 2.1. An incident electron with energy E_k interacts with a core atomic binding level and causes ionisation. The level depicted in the diagram is the K or $1s$. Relaxation of the atom back to its ground state occurs by filling the core level with an electron from an outer level. The excess of energy, which is the difference in the binding energies, then causes either an emission of a photon or an electron of characteristic energy. The electron that may be emitted

is called an Auger electron.

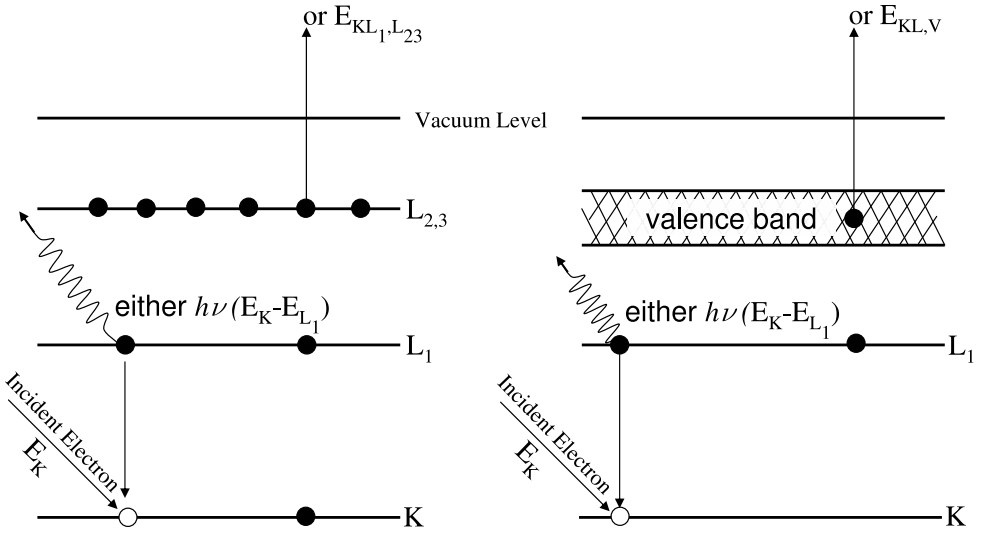


Figure 2.1: Schematic diagram of competing Auger and X-ray processes in an isolated atom(left) and a solid(right). For both cases the ionisation is at the core level and the Auger electron is emitted from the outer level for an isolated atom and the valence band in case of a solid. (After [6]).

Inasmuch both Auger and X-ray photon emission processes compete, the Auger emission probability is close to unity for core level binding energies less than ≈ 2000 eV. For the example shown for the isolated atom in figure 2.1, the Auger transition is labelled $KL_1L_{2,3}$ by convention. This follows the simple nomenclature based on X-ray spectroscopy, but does become inadequate if for example there is coupling between the two holes in the final doubly ionised state. For the study undertaken in chapter 3, our focus will not be on the details of the fine structure and its labelling in terms of spectroscopic nomenclature. When the atoms combine to form a solid (or liquid), the atomic energy levels shift and broaden to form energy bands. The outermost levels containing the valence electrons form the valence band. Auger transitions which involve electrons in the valence band are intense in solids. For the transition depicted

in figure 2.1 in case of the solid, it would be labelled KL_1V. If both the de-exciting and emitted electrons had emerged from the valence band then this transition would have be labelled KVV.

An Auger electron that has been emitted from the surface of a solid will have an energy that is directly related to its surroundings at or near the surface of the solid. This energy can be measured accurately by means of the technology that has been developed for Auger spectroscopy. A typical setup consists of a cylindrical mirror analyzer (CMA) or hemispherical analyzer (HA). For the Auger spectra collected in this work a HA was used. The electrons that leave the sample and enter the analyzer pass initially through a system of electrostatic lenses that defines the accepted analysis area. In the HA, a second set of electrostatic lenses controls the pass energy. A potential is applied to this second lens to reduce the kinetic energy of the electrons. Applying this potential allows one to operate the analyzer at a constant pass energy. The hemispherical part of the analyzer focuses the electrons into the plane of a channeltron electron multiplier. The detecting system thus measures the number of electrons at a certain kinetic energy. A prerequisite in any Auger spectrometer or most surface analysis equipment is ensuring that the sample is in an ultra-high vacuum (UHV) environment (typically $10^{-9} - 10^{-11}$ mbar). An UHV chamber ensures that there is a minimum level of adsorbates that reside on the sample surface. This is important because Auger electrons leave the sample with energies of the order of 10-800 eV for most light elements, and it is only the electrons that emerge within the first 5-10 nm of the surface of the sample that carry the information that is useful in Auger spectroscopy. For further technical aspects of surface spectroscopies the reader can refer to the texts in [6, 76–80].

Suppose we have an Auger transition that takes place in a solid from an element with atomic number Z. If the levels involved are, for example, K, L_1 and V then the energy of the Auger electron is given by:

$$E_{\mathrm{KL_1V}} = E_{\mathrm{K}}(Z) - E_{\mathrm{L_1}}(Z+\Delta) - E_{\mathrm{V}}(Z+\Delta) - \Phi_{\mathrm{A}} \tag{2.3}$$

where Φ_A is the work function of the analyzer. The term Δ, which lies between 0 and 1, is factored in to compensate for the higher binding energies that become apparent in the level that is ionized by the primary electron. Since every element has a unique electronic structure, we can see from equation (2.3) that Auger spectroscopy is a useful tool for elemental analysis. Because the combination of an atom with another changes the electron density surrounding the atom, which changes the binding energies, chemical shifts can be measured by Auger spectroscopy. We should note however that chemical shifts are more easily measured in X-ray photoelectron spectroscopy (XPS).

The electrons that emerge from the target into the analyzer, not only consist of Auger electrons, but also secondary electrons and elastically scattered electrons. The elastically scattered electrons are of course at the energy of the primary electron beam which is typically in the range of 1 to 5 keV. Auger peaks thus are difficult to see in the spectra because of the relatively high background. It is common therefore that most spectra are electronically differentiated during the acquisition mode. This is easily achieved by superimposing a sinusodial voltage (typically 0.1 to 5 V) over the analyzer. Most Auger spectra are shown as $\frac{dN}{dE}$ vs E and the Auger peaks appear as sharp spikes because of the change in slope at an Auger peak position. This differentiation also produces a *lineshape* relative to the Auger peak. This lineshape has been found to be an important source of chemical information, particularly when either or both of the electrons involved in the Auger transition originate from the valence band. If an electron participating in the Auger transition is in the valence band, then the electron carries information on the conditions of the band. Changes in lineshapes are very clear for carbon in the form of graphite, diamond and different carbides [9, 81–84]. It will be shown in chapter 3, that this is useful when analyzing thin layers of carbon at the surfaces of substrates.

2.2.3 Raman spectroscopy

The inelastic scattering of light by matter was first observed by Sir C. V. Raman in 1928 [15]. He observed that a minute fraction of the incident light was shifted from its

original wavelength after interacting with a liquid under observation. The effect was ruled out as fluorescence since it remained fixed with respect to the incident radiation and showed no dependence on the wavelength of the incident light. The effect was a result of the interaction of the light with the phonon vibrations of the liquid molecules, and is referred to as the *Raman effect* in honour of the person who first observed this phenomenon.

The origin of Raman scattering is due to the vibration of the atoms and polarizability of the electron cloud which make up the bonds in a solid, liquid or gas. Consider for example a simple gas such as CO_2. The molecule can be considered as a set of masses, with the carbon atom, m_{C} at the centre and the oxygen atoms, m_{O}, attached on each side. The bonds between the carbon and oxygen atoms are viewed as springs with spring constant k, and the vibration of the system about its centre of mass for simple harmonic motion is given by:

$$\nu = \frac{1}{2\pi}\sqrt{\frac{k}{\mu}}\,, \tag{2.4}$$

where μ is the reduced mass of the harmonic oscillator given by:

$$\mu = \frac{m_{\mathrm{C}} m_{\mathrm{O}}}{m_{\mathrm{C}} + m_{\mathrm{O}}}\,. \tag{2.5}$$

The time dependent positions of the vibrating CO_2 diatomic molecule are described by

$$r = r_e \cos 2\pi\nu t\,, \tag{2.6}$$

where r is the position at time t and r_e is the equilibrium bond length.

When an external field, ϵ, interacts with a vibrating molecule, such as described above,

the bonding electrons are displaced from their equilibrium positions inducing an electron dipole moment d proportional to the applied field ie.

$$d = a\epsilon\,, \tag{2.7}$$

where a is the constant of proportionality and is known as the polarizability of the molecule and describes the ease with which the electrons in the bond are distorted by the vibrating atoms. For a monochromatic source of light as is used in Raman scattering, the electric field which interacts with the molecule can be described by :

$$\epsilon = \epsilon_o \cos 2\pi\nu_o t\,, \tag{2.8}$$

where ν_o is the frequency of the the light source and ϵ_o is the amplitude of the electric field. An induced fluctuating dipole moment is obtained which is described by combining equations (2.7) and (2.8) ie.

$$d = a\epsilon_o \cos 2\pi\nu_o t\,. \tag{2.9}$$

Polarizability is a tensor quantity and the separation of the atoms described in equation (2.6) also determines the frequency with which the polarizability will vary. The polarizabilty can be described by a Taylor series expansion

$$a = a_e + \left(\frac{\partial a}{\partial r}\right)_e r + \cdots \text{higher terms}\,, \tag{2.10}$$

where a_e is the polarizability at the equilibrium position. For Raman scattering the amplitude of vibration is small and hence the higher order terms in the expansion can be ignored. By substituting equation (2.6) into equation (2.10) we obtain:

$$a = a_e + \left(\frac{\partial a}{\partial r}\right)_e r_e \cos 2\pi\nu t \,. \tag{2.11}$$

Substituting equation (2.11) into equation (2.9) yields the frequencies at which an oscillating dipole will radiate electromagnetic energy:

$$d = a_e\epsilon_o \cos 2\pi\nu_o t + \left(\frac{\partial a}{\partial r}\right)_e r_e\epsilon_o \cos 2\pi\nu t \cos 2\pi\nu_o t \tag{2.12}$$

$$d = a_e\epsilon_o \cos 2\pi\nu_o t + \left(\frac{\partial a}{\partial r}\right)_e \frac{r_e\epsilon_o}{2}[\cos 2\pi(\nu_o + \nu)t + \cos 2\pi(\nu_o - \nu)t] \tag{2.13}$$

recalling that $\cos A \cos B = \frac{1}{2}[\cos(A + B) + \cos(A - B)]$.

The first term in equation (2.13) is for elastic scattering or Rayleigh scattering. The second and third terms are due to inelastic scattering and imply that there must be a change in polarizability during the vibration of the molecule for that vibration to scatter radiation inelastically.

The photons that are inelastically scattered by the absorption of a phonon will have frequency $\nu_o + \nu$ and is known as the anti-Stokes line. If the incident photon is inelastically scattered by the emission of a phonon then it can have frequency $\nu_o - \nu$ and is called the Stokes line.

The above description of Raman scattering used a classical approach for the harmonic oscillator. The energy of the vibration of the atoms that constitute any substance is quantized and this quantum of energy is called a phonon. The quantum theory of phonons is adequately dealt with in the texts of Kittel [7] and [85]. It can be shown that the vibrations of a linear lattice of particles connected by springs can be quantized and the energy eigenvalues of the quantum harmonic oscillator are given by:

$$\mathcal{E}_k = \left(n_k + \frac{1}{2}\right)\hbar\omega_k \,, \tag{2.14}$$

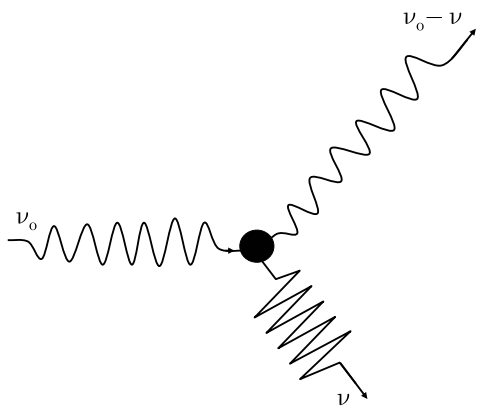


Figure 2.2: Stokes line (after [7]).

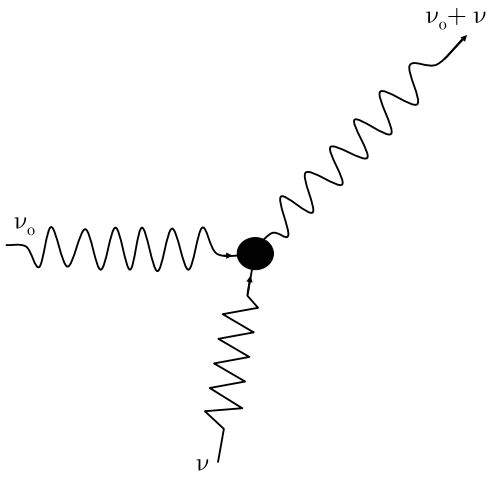


Figure 2.3: Anti-Stokes line (after [7]).

where the quantum number $n_k = 0, 1, 2, \cdots$ and ω_k is the frequency of the harmonic oscillator. With the above result it follows that the energy of the entire system of phonons is

$$U = \sum_k \left(n_k + \frac{1}{2} \right) \hbar \omega_k \,. \tag{2.15}$$

Equations (2.13) and (2.14) show that the phonons propogate as elastic waves and the energy associated with these elastic waves is quantized. Another important result of the quantum mechanical analysis is:

$$\frac{I\left(\nu_o + \nu\right)}{I\left(\nu_o - \nu\right)} = \exp\left(-\hbar\nu / k_B T\right), \tag{2.16}$$

where $I\left(\nu_o \pm \nu\right)$ is the intensity of the Stokes (phonon creation) or anti-Stokes (phonon annihilation) line, T is the temperature in Kelvin, k_B is Boltzman's constant and $\hbar$ refers to Planck's constant/2π.

The above description considered a linear lattice of particles for simplicity but can

be extended to describe a 3-D lattice. In many crystal systems at least two atoms form the primitive basis cell. The modes of vibration of such crystal systems are made up of what are termed, the acoustical and optical modes. Raman scattering involving acoustic phonons is called Brillouin scattering while it is called polariton scattering when optical phonons are involved. The brief overview outlined in equations (2.4) to (2.14) above demonstrates that Raman scattering processes can yield information on the mass of the atoms that make up the bonds in a lattice. By using the intensity ratio in equation (2.16) it is also possible to determine the density of vibrational states that generates the Raman scattered signal. In order to achieve this one needs a calibrated standard. More important, in terms of the experiment described in chapter 4, Raman scattering with the phonons in a diamond crystal lattice yields information on the nature of the bonds between the atoms in the crystal.

2.2.4 Basic semiconductor principles

With regard to the arguments presented in chapter 5, it is necessary to highlight some basic semiconductor physics. This overview is related to the ideas used in this work, but further details can be read in the texts of Kittel [7] and many textbooks on semiconductor physics.

As discussed earlier, when the atoms combine to form a solid (or liquid), the atomic energy levels shift and broaden to form energy bands. The outermost levels containing the valence electrons form the valence band. In metals one can consider the valence band to be 'half' filled. This implies that there are many energy states above the 'half' filled band that are not occupied, and an electron only has to gain a minute amount of energy to reach an unoccupied energy state in this level. The electrons that occupy these available states are termed 'free electrons' and form the basis as to why metals are termed good *conductors* of electric current. A material is considered an *insulator* when the valence band is completely filled. In this case there are no available states in or above the filled valence band which are near to the valence band. The next available state, available in the *conduction band* is separated by an energy gap, E_g, termed the

forbidden band gap. For a perfect material there are no available states an electron can occupy in the band gap. In order to reach the next lowest state an electron would require a considerable amount of energy which in the case of thermal excitation would be difficult. If however a voltage termed the *breakdown voltage* were applied across an insulating material, the electrons could acquire sufficient energy to occupy states in the conduction band.

In any material the Pauli exclusion principle prevents electrons in a crystal from acquiring energy due to thermal excitations of the atoms, unless the energy is sufficient for the electrons to occupy a level in the conduction band (for an insulator), which is separated from the filled valence band by an energy gap, E_g. There however remains a probability that a fraction of the electrons from the filled valence band will acquire enough energy to scale the energy gap. This fraction of electrons is proportional to $e^{-E_g/2kT}$, where k is Boltzman's constant and T is the temperature in Kelvin. These electrons will respond to an applied field as they occupy levels in the nearly empty conduction band. So a material that is a perfect insulator at absolute zero (-273.13 °C) can become a partial conductor at higher temperatures and its conductivity will increase with increasing temperature. This is the characteristic behaviour of a *semiconductor*. A semiconductor whose electrical conductivity is a result of the thermal excitation of charge carriers is termed an *intrinsic* semiconductor. In terms of band structure, a semiconductor is referred to as a direct band gap material when the maximum state of the valence band is directly below the minimum state in the conduction band. In these materials (for eg. GaAs) an electron can make a direct transition from the valence band to the conduction band. Diamond and silicon are examples of materials that have and indirect band gap. In these materials, an electron from the valence band needs to interact with a phonon to occupy an available state in the conduction band since the minimum state of the conduction band is not directly above the maximum state of the valence band.

In practice it is common to introduce impurity atoms into a semiconductor material

to achieve conduction. An n-type semiconductor is one which contains a number of impurity atoms which add electrons to the crystal. With respect to the energy band description, the impurity atom creates a donor level which lies in the band gap of the material. If it is a shallow donor then its energy level, E_D, will lie fairly close to the lowest available energy level of the conduction band. The probability of transferring an electron form a donor level to an unoccupied state in the conduction band is proportional to $e^{-E_D/kT}$. Silicon, for example, which is a tetrahedrally covalently bonded semiconductor material can have the pentavalent phosphorus atom in a substitutional lattice site as an n-type impurity atom.

A p-type semiconductor material is one where an impurity atom removes an electron from the topmost filled valence band so that it can occupy a substitutional lattice site of the material. Consider again the silicon lattice with the trivalent boron atom occupying a substitutional lattice site. In this case the acceptor level, E_A, lies close to the top of the valence band. The probability that an electron will leave the uppermost level of the filled valence band to occupy an available state in the acceptor level is generally proportional to $e^{-E_A/kT}$. When an electron leaves the valence band it leaves behind a positive 'hole'. Thus in a p-type semiconductor the electrical transport is by hole conduction. In an n-type semiconductor the majority carriers are electrons, while in a p-type material the majority carriers are holes. Semiconductors whose conduction is increased by introducing dopant atoms are termed *extrinsic* semiconductors.

Another important concept used in semiconductor theory is the notion of the *Fermi level*. The origin of the Fermi level comes from statistical physics (Fermi-Dirac, Maxwell-Boltzman or Bose-Einstein) where it is referred to as the *chemical potential*, μ and it describes the average energy change per particle. The reader is pointed to the texts in [7, 8] for a complete description of the ideas of statistical physics and particularly the Fermi-Dirac distribution law. As discussed earlier electrons (fermions) obey the Pauli exclusion principle and cannot exist in identical energy states. At absolute zero the electrons occupy the lowest available energy states and build up a 'Fermi sea'

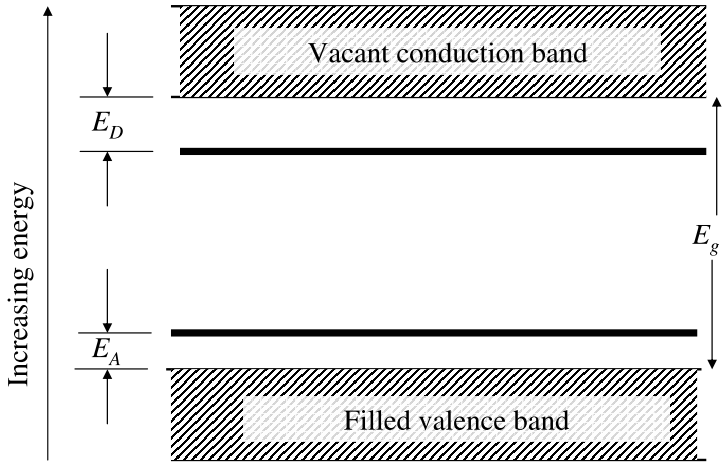


Figure 2.4: Illustration of the energy bands of a solid with both donor and acceptor states within the forbidden band gap and a band gap energy E_g. The acceptor impurity level lies at an energy E_A above the filled valence band and the donor impurity level lies at an energy E_D below the empty conduction band. (After [7]).

of electron energy states. The Fermi level is the energy-surface of that sea at absolute zero and no electrons will have sufficient energy to rise above this surface.

At higher temperatures there is a probability that an electron will occupy states above the Fermi level. The probability that an electron will occupy a given energy state at a given temperature can be calculated from the Fermi function (derived from Fermi-Dirac statistics):

$$f(E) = \frac{1}{e^{(E-E_F)/kT} + 1}\,, \tag{2.17}$$

where k is Boltzman's constant and T is the temperature in Kelvin. It can be seen that this function dictates that at ordinary temperatures ($\approx 300\,\mathrm{K}$), most of the levels

are filled up to the Fermi level, E_F, and a few electrons have energies above the Fermi level. In a semiconductor the valence band is separated from the conduction band by the band gap E_g. In the band gap, the density of electron energy states is zero while the Fermi function has a finite value in the band gap. So of course no electrons can be found in the band gap even at higher temperatures. But there are many states available in the conduction band and the Fermi function has a finite value in the conduction band at higher temperatures. From this we can see that the conduction of a semiconductor material increases with temperature as expected. It can be shown that under certain conditions that the Fermi level in an intrinsic semiconductor lies near the midpoint of the band gap [7]. More pertinent to the discussions in chapter 5, it is apparent from the above discussion that the position of the Fermi level will be influenced by the n or p-type dopants in a semiconductor material. In an n-type material the Fermi level is shifted towards the conduction band and lies near the energy levels created by the n-type dopant. Similarly it can be shown that for a p-type material the Fermi level lies near the acceptor level. In both these cases the temperature is low; at high temperatures the Fermi level shifts to the midpoint of the band gap for either a n or p-type semiconductor [7, 8].

Of particular importance to this text is the construction of a $p-n$ junction. The $p-n$ junction is the basis of most semiconductor device construction used in electronics. As its name suggests a $p-n$ junction is formed when a n-type semiconductor is physically joined to a p-type material. Creating n or p-type regions in a semiconductor material is easily achieved by ion implantation. Prior to the implantation method the generation of $p-n$ junctions was made possible by introducing the dopant atoms during the melt phase in semiconductor materials such as silicon and germanium. This is not possible in diamond and hence the implantation method is more commonly used to create solid state devices in diamond. This approach is used in chapter 5. With regards to the discussion on the results obtained in chapter 5, a brief outline on what occurs at the interface of a $p-n$ junction is discussed below.

The $p-n$ junction

As discussed earlier the Fermi level will lie at different positions in an n or p-type semiconductor. When the two types are joined or the different regions are created by ion implantation, the Fermi level must be constant throughout $p-n$ junction. This condition is necessitated by the definition of the Fermi level as a chemical potential which is a property of the entire material. At the interface of a $p-n$ junction, the equalisation of the Fermi level is achieved by moving the entire band structure of the p-type material relative to the n-type side. This movement of the band structure occurs because of the redistribution of the electrons at the interface of the junction, which in turns changes the potential energy. At the interface some of the free electrons on the n-type side diffuse across the to the p-type side and combine with the holes. This creates a region of positively charged donors and negatively charged acceptors which is referred to as the *depletion region*. This is illustrated in figure 2.5.

If a $p-n$ junction has an applied voltage across it, then electrons will be continually removed from one side. In this case the situation of a uniform potential as illustrated in fig. 2.5 is never attained and no net current flow will be observed. A $p-n$ junction is said to be *reverse biased* if a an external potential V is applied so that the n-type side is positive. In this case electrons are being removed from the n-type side which implies that the Fermi level is decreased by an amount eV on this side. Alternatively one can view this situation as an increase in the width of the depletion region. The probability that an electron will flow from the n-type side to the p-type side will be reduced since the potential it has to overcome has been increased by an amount eV. Hence the current flow in the reverse bias mode is fairly small even for high applied voltages.

When the p-type side of the junction is connected to the positive terminal of a voltage supply the junction is *forward biased*. An electron will now traverse a potential barrier which has been reduced by an amount eV. In this case the width of the depletion region is reduced and the current flow is significantly enhanced. A $p-n$ junction thus

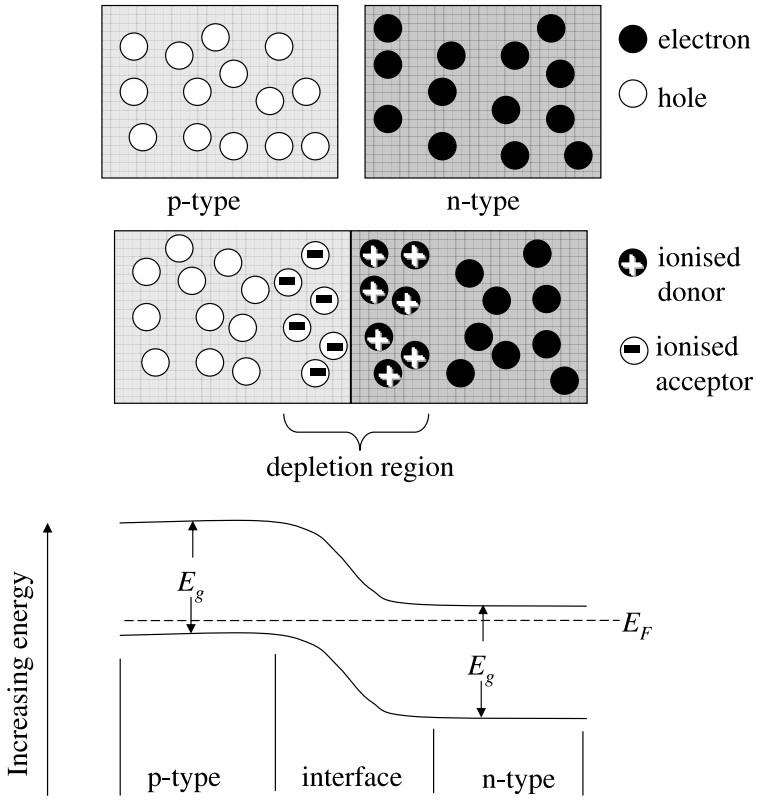


Figure 2.5: Illustration of the formation of a $p-n$ junction and the corresponding band structure when equilibrium is attained. No electric current flows when the Fermi level is equalised on both sides. (After [8])

acts as a rectifier. Typical $I-V$ curves for a $p-n$ junction diode is shown in figure 4.3. Figure 2.6 illustrates the behaviour of a $p-n$ junction in forward and reverse bias.

The above discussion and relevant diagrams have been summarized from the texts in [7, 8, 86].

Light Emitting Diodes (LED)-Electroluminescence

The fabrication of LED's in semiconductor materials (especially GaAs, GaAsP and GaP) is a well developed industry. In particular the development of the blue LED was important to the development of the high information density storage on optical disks.

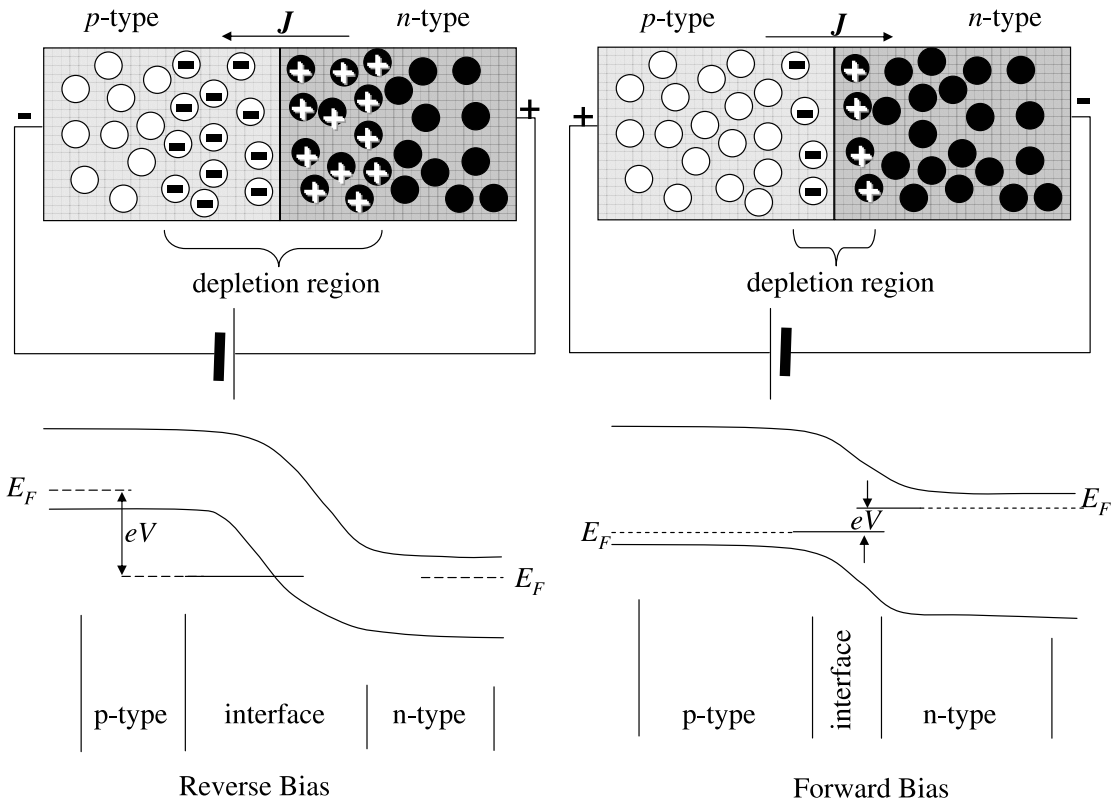


Figure 2.6: Illustration of a $p-n$ junction in reverse bias mode(left) and forward bias(right). $\boldsymbol{J}$ indicates the direction of conventional current flow. (After [8]).

LED's are also used in the fabrication of solid state lasers by using suitable modulating circuits.

Based on the discussions presented earlier it is apparent that a $p-n$ junction can act as a LED. In the forward bias configuration electrons are injected to the conduction band on the p-type side of the junction, while holes are injected into the n-type side. Electron-hole recombination processes do occur on either side of the junction and within the depletion region, which in some cases, results in the emission of a photon. The energy of the photon is dependant on the energy levels involved in this recombination process. In chapter 5, we measure the luminescence emitted by a diode junction created

by ion implantation in a type IIb diamond, and use this information to infer which defect bands are responsible for the luminescence. In this manner, electroluminescence can be used as a diagnostic tool, which can reveal information on the defects and their associated energy bands created during the implantation-annealing process.

2.3 Literature Review

2.3.1 A brief background on ion implantation

In relation to the content of this thesis it is imperative to gauge a brief summary of how the ion-solid interaction has been exploited in the solid state material sciences. The content of work that has been published is extensive and specified article reviews are pointed out for more detailed reading.

The initial research incentive to understand the ion-solid interaction was pre-empted by a need to understand the effects fissile material had on the materials used in nuclear reactor components [87]. The early work of ion beam bormbardment utilised ion energies in the tens of keV ranges to sputter the surfaces of materials. As technology increased in accelerator based physics, the ability to accelerate ions of any element up to energies in the MeV range has now become possible. One of the earliest applications of introducing atoms into a solid state material by an accelerator was in the semiconductor fabrication of diode junctions. The initial work by Ohl [88] in 1952 at Bell Laboratories and then later by Cussins [89] in 1955 were able to demonstrate dopant activation, but was hampered by their inability at the time to remove the damage created by the implantation process. These damage centers acted as charge traps and compensating centers. Schockley [90] and Moyer [91] then demonstrated that by post implantation annealing, these defects were reduced and a restoration of the lattice crystallinity was achieved. Their ideas were used to demonstrate diode action for use in nuclear particle detectors by Alvegar and Hansen [92] and Martin [93]. By the 1960's, the rapid enhancement of accelerator technology and the fabrication of integrated circuits for commercial exploitation, spurred on the research for good quality diodes using ion implantation. This was achieved and good quality bipolar transistors and metal oxide semiconductor transistors were reported [94–97] This method of producing semiconductor action in germanium and silicon was by the mid 1980's a highly developed and sophisticated field. A plausible understanding of these rapid developments in the field was that the method was clean and reproducible. It was also possible by lithography

techniques to mask off certain areas and only implant selected areas to a predetermined density. This is usually the case for most semiconductor device construction. Diffusion furnaces which were used earlier in silicon technology became somewhat obsolete as a result of this added advantage in ion implantation technology. The technique also assisted in the miniaturization of devices in integrated circuit technology.

As the demand for ion implanters grew, new applications of the method were reported in the literature at a bewildering rate. These applications were enhanced by advancements in the ion source technology which made a host of exotic ion beams easily attainable. The hardening of stainless steel by nitrogen implantation has had an impact on drilling and surgical tools, implantation of active elements into catalysts used in the synthesis of petroleum to prolong their reaction time, the introduction of rare earth elements into silicon for laser application, the generation of new phase materials [98–100] and the list goes on. Coupled with the theoretical advances in ion beam analysis, exotic probes such as radioactive indium, carbon-13 etc, were implanted into different lattices, and nuclear techniques such as perturbed angular correlations, nuclear reaction analysis [101], etc were employed to glean information of the implanted probe and the host lattice at an atomic level [102–104]. More recently, the introduction of atoms into a matrix by ion implantation has been utilised to investigate the phenomenon of nanophase particles embedded in the host lattice. This colossal research endeavour continues unabated and will no doubt continue to add to scientific knowledge. Apart from the experimental techniques that have been and are presently being pursued, theoretical modelling of the ion-solid interaction has progressed to a high degree. Point defect engineering has consequentially become a useful technique in improving the quality of doped layers in semiconductor physics. These advances have been developed to a deep understanding in conventional semiconductor materials such as silicon, germanium, GaAs, etc. In diamond semiconductor physics, these ideas have also developed to a reasonable understanding. A part of this thesis is focussed on how defects introduced as a result of the implantation process can be used for minority carrier injection.

2.3.2 Ion-Implantation into diamond

The successes that were achieved by ion implantation into silicon and germanium were an obvious precursor that the same feat could be achieved in diamond for semiconductor application. However the same properties that made diamond an attractive semiconductor material made the task of introducing dopants via the implantation method or other conventional methods a challenging task. The diamond lattice reverts to graphite when heated to temperatures above 1800 °C. So the idea of implantation and annealing the lattice at its melting point to reconstitute the lattice and activate the implanted dopants, as was possible for silicon and germanium, could not be applied to diamond. The relaxation of diamond to graphite also excluded the use of diffusion furnaces to dope the diamond lattice. In spite of these drawbacks the implantation-post annealing method still presents one of the best routes to introducing dopants to higher densities into the tightly covalently bonded diamond lattice.

The implantation method gained momentum when Wentorf and Darrow in 1965 reported that the diamond surface became conducting when exposed to a low energy plasma. Vavilov *et al* in 1968 published their work on keV lithium and boron implanted diamond. They measured the activation energies for these dopant atoms. A large body of work followed in the literature, with contradicting claims made by research workers in the field [17]. We can conjecture that these initial attempts with their opposing claims were a result of the lack of understanding of the point defects created during the implantation process, and how they compensated the presumed activated dopant atoms.

Within the last three decades, the experimental and theoretical research into the semiconducting possibilities of diamond began to reveal how the point defects and extended defects introduced by ion implantation influenced the mobilities of the carriers and the activation energies of the dopant atoms. The implantation-annealing recipes that have emerged for diamond doping span a wide variety of approaches. Relevant aspects and the appropriate references to these developments have been outlined in

section 1.1.2. Unlike silicon that will collapse to an amorphous silicon when the damage introduced by implantation exceeds a critical value, diamond relaxes to its polymorph, graphite or graphite like state, when the damage supercedes a critical level. This value has been termed the graphitization threshold and has been calculated to be $1 \times 10^{22}\,\mathrm{vac.cm^{-3}}$ [105] according to TRIM. It is also referred to as the amorphization threshold [13, 37, 106–109]. This revelation consequently led to some of the creative approaches to achieve semiconducting behaviour and make ohmic contacts to this wide band-gap material [17, 32, 110].

The relaxation of the diamond lattice to graphite when the radiation damage exceeds the critical damage density is related to the difference in temperature at which the interstitials and vacancies migrate in diamond [31]. Three temperature regimes have been deduced to give a description of how the point defects migrate in diamond within the collision cascade of the implanted ion during implantation. At temperatures below $\approx 50\,^{\circ}\mathrm{C}$, the vacancies are immobile while the mobility of the interstitials is severely inhibited. Above $\approx 50\,^{\circ}\mathrm{C}$ and below $\approx 500\,^{\circ}\mathrm{C}$ the interstitials are mobile and a fraction of them recombine with the vacancies. A percentage of these interstitials diffuse away from the implanted region leaving behind an excess of vacancies. The onset of the graphitization threshold may occur for higher ion doses at higher target temperatures due to the increased probability of vacancies annihilating with interstitials. For target temperatures above $500\,^{\circ}\mathrm{C}$ both the vacancies and the interstitials are mobile. Because of this the interstitial-vacancy annihilation rate is greatly enhanced, and the diamond structure remains intact [35]. It was also shown that when a diamond substrate is implanted with the isochemical element, diamond growth occurred at the surface at high implantation temperatures. The nature of the diamond layers generated in this manner has been found to be highly dislocated [111].

The constraint of using natural and synthetic substrates to fabricate suitable devices by ion implantation has been the intrinsic defects that are already present in these substrates. The volume of publications on the different types of defect structures

in synthetic and natural diamond that have been discovered experimentally and modelled theoretically is immense. These include interstitial type defects, vacancy centers, nitrogen aggregates, nickel complexes, just to name a few. A vast domain of experimental techniques and theoretical models have been used to elucidate the nature of the different types of defects that are present in diamond before and after implantation. The reader is referred to the texts contained in [3, 33, 39, 104, 107, 112–121] for a brief overview of the many types of defects in diamond. I will refer to some of them which are relevant to the text of this work. Thus the quest of finding a suitable route to grow high quality diamond layers which are close to defect free remains a precursor to the development of viable device fabrication in diamond. High quality CVD diamond layers can be generated by homoepitaxy, but crystal sizes are determined by the size of the diamond substrate and these are usually small. The work in chapter 3 of this thesis looks at one such possibility for the generation of high quality large area diamond layers.

The implantation route route used in this study has been employed to generate p-type layers in diamond. A brief overview of this implantation 'recipe' is presented in the next section.

2.3.3 The CIRA process for doping diamond

The focus in the content of this thesis is the cold-implantation-rapid-annealing (CIRA) process for doping diamonds, developed in South Africa by J F Prins. The approach of the CIRA technique is a consequence of the temperature regimes at which the point defects are mobile in the diamond lattice. As discussed in the previous section, the interstitials in the diamond lattice are mobile at low temperatures relative to the temperature at which the vacancies become mobile. Implantation at ambient temperatures at some single energy will result in an excess of vacancies being left in the region in which the selected dopant atoms will come to rest. At keV energies the interstitial atoms diffuse to the nearest surface away from the implanted layer. Any subsequent annealing to trap the dopant atoms in substitutional sites and reduce the radiation

damage created during the implantation is thwarted by the fact that the implanted region has an excess of vacancies. Any annealing above $\approx 500\,^{\circ}$C may in some cases (depending on the initial dose implanted) result in the implanted region graphitizing. Even if the implanted region does not collapse to a graphitic structure after annealing, any dopant activation which leads to electrical activity, is inhibited by the defects that form from the excess vacancies.

Thus the conventional approach which applied to Si, GaAs, Ge etc did not produce the desired effect in diamond when it came to doping by means of ion implantation. To circumvent the problems dicussed above, the CIRA technique requires that the diamond target be held at cold temperatures, typically liquid nitrogen temperature ($\approx$-196 °C). The implantation energies and doses are also chosen such that the dopant atoms are spread over a width, say ω. After the implantation steps have been carried out, the diamond is then removed from the target holder and transferred to a liquid nitrogen bath. The diamond sample is then dropped into a preheated crucible which is usually at temperatures above $\approx 500\,^{\circ}$C. This approach hinges on the fact that one can reduce the vacancies left after the annealing process, by ensuring that there are enough carbon self-interstitials within the implanted layer to annihilate with most of the vacancies. The reason for increasing the width is to increase the probability that a self-interstitial will encounter a vacancy, and also for that same reason, a dopant atom will be caught in a substitutional site.

The probability P_c that an interstitial will annihilate with a vacancy may be written as:

$$P_c = \frac{\mu_e}{\mu_e + \mu_c}, \tag{2.18}$$

where μ_c is the average jumps an interstitial will make in the width ω until it meets up and annihilates with a vacancy and μ_e is the number of jumps to diffuse out of the layer. It is assumed that once an interstitial atom diffuses out of the implanted layer

it will never return. However it is practical to note that some interstitials could return to the layer and so the probability is then written as:

$$P_c = \frac{\mu_e}{(1-\Phi)\,\mu_e + \mu_c}, \tag{2.19}$$

where Φ lies between 0 and 1. These ideas are further developed in terms of the concepts of a 'catch-volume', 'catch- site' and a 'meet-site'. Within the context of these concepts, the probability defined above is now postulated to relate to the catch-volume surrounding a vacancy, where if an interstitial may wander into this volume it spontaneously annihilates with the vacancy. The interstitial may also diffuse up to the boundary of this volume called the meet-site. It can then jump into a catch-site within the volume, or still diffuse away into one of the surrounding interstitial sites. If on average an interstitial has to make μ_m jumps to reach a meet site, it can be shown that

$$\mu_c = \mu_m\left(1 + q\exp\left[\frac{E_C - E_D}{k_B T}\right]\right), \tag{2.20}$$

where T is the temperature, E_C is the activation barrier that needs to be scaled when jumping from a meet-site into a catch site, E_D is the activation barrier that is scaled during diffusion, q is the ratio of available interstitial sites to catch-sites when an interstitial is in a meet-site and k_B is Boltzmann's constant. Since μ_m is inversely proportional to the number of vacancies N_v, one can write that:

$$\mu_m = \frac{Q}{N_v}, \tag{2.21}$$

where Q is a constant of proportionality. Substituting (2.21) and (2.20) into (2.19) gives:

$$P_c = \frac{\mu_e N_v}{(1-\Phi)\,\mu_e N_v + Q\left(1 + q\exp\left[\frac{E_C - E_D}{k_B T}\right]\right)}. \tag{2.22}$$

The best way to increase P_c to be near 1, will be to increase μ_e. A larger width ω will increase μ_e and minimize the number of interstitials that diffuses away from the implanted layer. Equation (2.22) is not a description of the CIRA process, but demonstrates that the parameters of the CIRA process do strive to optimize P_c to be near unity. This will in turn reduce the number of vacancies that are left after the annealing step thereby reducing the compensating bands that impair the n or p type conductivity of the activated dopant atoms. The single and complex vacancy structures also act as scattering centers that reduce the mobility of the charge carriers. For a more detailed and theoretical description of the above process the reader is referred to the texts in [31, 34, 35].

The CIRA process is used in the experiment discussed in chapter 4 and the resultant radiation damage is analysed using Raman spectroscopy. The doses and energies used in table 4.1 create a width of $\approx 0.23\,\mu$m below the surface of the diamond. The doses and energies were chosen so that the vacancy distribution, as generated by TRIM, was uniform from near the surface to the maximum implantation depth. A similar set of implantation parameters using the CIRA technique has been used to generate boron doped diamond.

2.3.4 Radiation damage in diamond

Our focus in this body of work is the radiation damage caused as a result of the implantation process. During this process a host of carbon atoms are knocked out of their lattice positions thereby creating vacancies, carbon self-interstitials and extended defects. The dopant atoms also occupy positions which may be substitutional and in or near an interstitial site. The nature of the damage is dependent on the current density

of the accelerated ions, implanted dose, diamond temperature during implantation, ion energies, mass of accelerated ions and subsequent annealing cycle.

There are many techniques that can be used to assess the state of the diamond lattice after the implantation annealing process. The choice of any technique is dependant on the changes one wishes to observe as a result of the implantation and annealing process. Primary changes that occur are in the electrical and optical properties as well as lattice alterations. Suitable texts have been suggested in section 2.3.2.

2.3.5 Auger spectroscopy identification of the allotropes of carbon

Auger spectroscopy is a useful tool in determining the chemical state of carbon when it resides near the surface of a substrate. In relation to the work presented in chapter 3, we were primarily interested in determining the nature of the bonding between the carbon atoms that had segregated to the surface of the copper and copper-nickel substrates used in this study. It has been shown that the solid state allotropes of carbon viz. diamond, graphite and carbides have a distinct lineshape with respect to the differentiated Auger spectrum [9, 81–84].

The different lineshapes in the differentiated Auger spectrum can be expected since the covalent sp^3 bonding in diamond will have a KVV transition which is different from the KVV transition in an sp^2 network of carbon atoms as in graphitic carbon. This distinction will be shown specifically for the spectrometer set-up used in chapter 3. Further reading on Auger spectroscopy is detailed in [6, 76–80].

2.3.6 Raman Spectroscopy studies on the allotropes of carbon

In relation to the discussion in section 2.2.3 it is clear that Raman spectroscopy is a sensitive non-destructive tool in determining the bond structure between carbon atoms. sp, sp^2 or sp^3 bonds between the carbon atoms will have distinct vibrational states,

while cubic and hexagonal structures will also have unique signatures [122, 123], if they are Raman active. Raman spectroscopy has been used extensively in diamond research, and has become one of the primary diagnostic methods in the field of diamond nucleation by High Pressure High Temperature (HPHT) or chemical vapour deposition (CVD) [124, 125].

The diamond Raman line originates from first order scattering on the triply degenerate transverse optical (TO) phonons of F_{2g} symmetry in an undisturbed diamond lattice which corresponds to the vibrations of the two interpenetrating FCC lattices decribed in fig 1.2. This unique line acts as a fingerprint for identifying diamond and was first observed by Ramaswamy and Bhagavantam [15]. Irrespective of the excitation wavelength, the line appears at 1332.5 cm^{-1} in the Raman spectrum. At room temperature the Stokes line is much stronger than the anti-Stokes line. The Stokes line when observed at room temperature is narrow and has a Lorentzian shape for high quality diamonds [see fig. 4.4]. The Raman scattering cross-section for diamond is relatively large, but much smaller than that of graphite. The phonon-confinement model is often used to explain changes that are observed in the first order Raman diamond line under different experimental conditions. Details of the model and the theoretical considerations upon which it is based is adequately oulined in the text of [124]. It is important to note that, as pointed out by Ager *et al* [124], the phonon-confinement model does not describe some of the experimental observations with regards to the first order diamond diamond Raman line.

Our focus in this work is on the changes that occur in a diamond lattice as a result of the implantation process (chapter 4) and the segregation of carbon on the surface of copper and copper-nickel substrates (chapter 3). We will therefore centre our dicussions on the relevant Raman features related to these aspects. The D-band (1310 to 1450 cm^{-1}), G-band (1520 to 1610 cm^{-1}) and G-line ((1585 cm^{-1}) are some of the features we will refer to where relevant to this study [126]. In the literature, Raman shifts obtained near 1250 cm^{-1} are controversially associated with amorphous

diamond [107, 127]. Amorphous diamond is best described as a diamond structure which mantains its lattice translation over small crystal domains (<100 nm). In ion implanted diamond it is conjectured that amorphous zones are created by the implanted ion by ballistic type processes [37] or thermal spikes [13]. These amorphous zones with a three-fold coordination or sp^2 bonded configuration alter the periodicity of the diamond lattice. The Raman spectra of such a diamond layer are reported to mimic closely the phonon density of states of diamond where a maximum occurs close to 1250 cm^{-1} [107]. The 1250 cm^{-1} Raman shift is also argued to originate from transpolyacetylene (double bonded carbon chains) [123, 127] which is observed in nanodiamond. The reader is referred to the text in [3, 107, 119, 126] for a summary of the many other features that are present in the Raman spectra of carbon and its allotropes. In particular the book by Zaitsev (2001) [3] reviews all of the Raman signatures obtained in the literature for diamond and CVD diamond obtained under different experimental conditions before 2001.

Chapter 3

Carbon overgrowths on FCC crystals after ion implantation

3.1 Introduction

High-pressure high-temperature processes to grow diamond have advanced to a high degree of sophistication. At high pressures (≈200 kbar) and high temperatures (≈4000 °C) graphite which is the thermodynamically stable phase of carbon at room temperature, can be converted into diamond. The same process is enhanced by the use of metallic catalysts such as nickel, iron, cobalt and chromium. These metal solvent catalysts increase the transformation rate and drastically reduce the temperature (≈1600 °C). and pressure (≈60 kbar) [15]. The present technology can now deliver high quality single crystal diamond comparable to the morphology of natural type IIa diamond. The process can include boron in the growth capsule and deliver p-type semiconducting diamond. However, the ability to use this present technology to synthesize large area single crystal diamond layers is not possible. Many other processes have been developed notably at low pressure and the reader is referred to the texts in [9–12, 60, 62, 64, 122, 128–134] The process of CVD of diamond has however paved a possible way forward to achieve the growth of high quality diamond layers. A suitable substrate with a large surface area is at present the stumbling block to generating sin-

gle crystal diamond layers with a low defect density and large area. In this chapter we present the initial results that were obtained in an effort to find an alternative solution to providing a suitable substrate to deliver single crystal diamond by CVD.

The work presented in this chapter was initially the focus of this dissertation. Unfortunately due to some major equipment failures, the research focus shifted to the work presented in chapters 4 and 5. The results presented are thus not from a complete study. It is a work in progress and we hope that our initial intents will be realised in the near future.

3.2 Background

As mentioned earlier, the low pressure, low temperature process of CVD to generate diamond layers on non-diamond substrates was a revolution in materials science. The method can deliver high quality single crystal diamond, when the substrate is single crystal diamond or cubic boron nitride. When the substrate is non diamond materials such as silicon and silicon carbide the diamond layers generated by CVD processes are polycrystalline. One of the primary reasons for the unoriented growth is the lattice mismatch with the substrate to that of the diamond lattice spacing. Reviews on the CVD processes are adequately dealt with in the references listed earlier. I will not attempt to discuss the process in detail in this thesis, but take note of the role of H_2 in the CVD process. The other primary gases that are predominantly used are the hydrocarbons, such as methane. The two gases, H_2 and CH_4 or C_2H_2 etc, where the hydrogen is about 98 to 99.5 % by volume, are passed over a heated substrate (700-1000 °C) for example molybdenum, silicon or silicon carbide. The substrate is sometimes biased with a suitable voltage, and the hydrocarbon molecules interact with the surface substrate. Any sp^3 carbon that resides on the surface substrate remains, while any sp or sp^2 carbon species are etched or reduced by the hydrogen. The exact nature of the substrate in terms of the chemical interaction with the hydrocarbon species does not appear to be a precursor for diamond nucleation, but without hydrogen in the plasma, the nucleated

diamond is overwhelmed by the graphitically bonded carbon. Variations on the CVD process have been developed which include hot filament CVD, plasma (direct current discharge, microwave and radio frequency) CVD and combustion flames [131]. Apart from the interest in diamond synthesis, other classes of materials in which carbon is a primary constituent have been developed. These include diamond-like carbons (DLC), amorphous carbon-nitrides (a:C-N) and amorphous carbon-silicon alloys all of which show an interesting array of optical and physical properties [123].

From the experimental evidence thus far, it has been proved that homoepitaxial diamond growth is possible by CVD, whereas heteroepitaxy mostly leads to polycrystalline growth. The primary difference between the two applications is as mentioned the lattice constant mismatch between diamond and the substrate. Listed in table 3.1 are the lattice constants for certain select materials. An obvious choice for the CVD process would be copper or nickel since the lattice constant compares well with that of diamond. A Cu-Ni alloy may also lead to a lattice parameter close to that of diamond. Nanocrystalline $Cu_{0.55}Ni_{0.45}$ alloys generated by pulsed electrodeposition has a lattice constant of 3.569 Å [135]. Heteroepitaxy of single crystal copper on diamond (100) surfaces has been reported [58, 67], while CVD *single* crystal diamond growth on copper and nickel has been attempted but not much success has been achieved on these substrates apart from polycrystalline diamond [11, 12, 136, 137].

Substrate (structure)	Lattice constant (Å)
diamond	3.567
silicon (diamond)	5.430
nickel (fcc)	3.520
copper (fcc)	3.610
SiC (diamond)	4.350

Table 3.1: Lattice constant and structure of certain select materials.

We need to emphasize that inasmuch as the advent of the low pressure process of CVD diamond growth brought about the hope that single crystal diamond may be

achieved on large area substrates, this potential has not yet been realised by heteroepitaxy. The process still remains the best hope that this feat can be achieved, since it has been shown that the homoepitaxial process does deliver single crystal growth [129]. The obvious way forward is how to prepare a surface of a substrate with a large area and a lattice constant similar to single crystal diamond.

One such alternative was proposed by Prins and Gaigher, and this approach is the central focus of this chapter. The experimental approach presented by Prins *et al* centres on using copper as a substrate owing to the close lattice proximity and the FCC lattice arrangement which occurs in copper and diamond. The idea focussed on carbon ions implanted into a copper substrate held at high temperature. Due to the low solubility of carbon in copper, the implanted carbon ions diffuse to the surface or possibly migrate to a carbon cluster within the implanted host. The ensuing interactions at the surface of the copper substrate between the C-C atoms will result in carbon overgrowths. It is possible that the morphology of the copper substrate can influence the carbon atoms at the surface to assume the diamond lattice. Both single crystal copper (111) and polycrystalline copper substrates were used in the experiment first performed by Prins and Gaigher [138]. The energy of implantation of the $^{12}C^{+}$ was 120 keV and the dose rate was around $6.5 \times 10^{16}.\mathrm{cm}^{-2}.\mathrm{h}^{-1}$. The total dose implanted was 5×10^{17} $^{12}C^{+}.\mathrm{cm}^{-2}$. The target temperature was high, of the order of 900 °C for a series of experiments. The carbon overgrowths generated under these conditions were lifted from the copper by means of chemical etching and floated onto glass slides. Their initial analysis revealed that some of their etched fragments was diamond, while most others were highly oriented graphite.

A series of overgrowths generated by carbon implantation into polycrystalline copper samples were analyzed using Raman spectroscopy and transmission electron microscopy (TEM) by Hoff, Vestyck, Butler and Prins [139]. The overgrowth layers liberated from the copper substrates were transparent and 3 of the fragments analyzed showed definite traces of diamond. In a particular fragment, the TEM analysis revealed

orientational carbon overgrowth with the diamond lattice parameter ($a = 0.356\,\text{nm}$) and the Raman analysis showed a signal for diamond at $1326\,\text{cm}^{-1}$. Further experimentation by Prins and Gaigher for carbon implantation in single crystal copper (111) was not able to reproduce the result, and the etched overgrowths were identified as oriented graphite. Further efforts to corroborate the results obtained by Prins and Gaigher were performed by Lee *et al.* They performed a similar experiment with 200 keV carbon ions on (100), (110), (111) and (210) copper crystals. The copper substrate temperature was in the range 850-1000 °C during the implantation procedure. All of their overgrowths revealed (0001) oriented graphite formation [140]. Nayaran *et al* [141] reported a method based upon carbon implantation (60 to 120 keV) into copper (polycrystalline and single crystal specimens) at room temperature and thereafter followed by pulsed laser melting of the copper substrate. The carbon overgrowths generated in this manner contained the diamond Raman signal at $1332\,\text{cm}^{-1}$. They also reported that carbon implantation at room temperature or higher temperatures alone did not result in the formation of the diamond phase, but the pulsed laser irradiation and rapid solidification was found to be necessary to produce the diamond phase. Cabioc'h *et al* [142], published their findings on their work using the implantation-outdiffusion technique in copper. They observed uniformly oriented graphite overgrowths as well as insulating carbon layers and carbon onions similar to those reported by Banhart [143] and Lu-Chang [144] after electron irradiation of graphitic carbon. Banhart demonstrated in their experiment that the carbon onion cells are able to transform to diamond after electron radiation. Further evidence of carbon onions was shown by Hiroaki [145] after carbon implantation into copper. Wang *et al* [146] implanted both carbon and hydrogen into copper which resulted in both graphitic carbon and diamond like carbon (DLC) formation.

As mentioned earlier we revisit the implantation-outdiffusion method of carbon overgrowths on fcc crystal systems, in particular copper due to its low affinity to form a carbide. From earlier reports on the method, it is clear that both diamond and more often graphitic layers have been generated using the approach. We describe

below a unique end station that has been developed to alter the surface conditions of the substrate during implantation. The implantation-outdiffusion approach is also being used to try and synthesize other interesting materials, which if successful will have immense technological applications [99, 133, 147]. Other forms of carbon growths which are of current interest are fullerenes and carbon nanotubes [148].

3.3 Experimental considerations

3.3.1 Sample preparation

A programmable Eurotherm tube furnace was used to grow single crystal copper and copper-nickel (16.6 % Ni by mass) crystals. The copper and copper-nickel metal sections were prepared by melting high purity copper and copper-nickel powder (99.99 %) in a graphite crucible. The Cu-Ni composition was prepared by mixing Cu and Ni powder. The mixture was tumbled for several hours to obtain a uniform distribution of the Ni in Cu. The copper or copper-nickel powder was placed in a RF furnace and the system was flushed with argon during this melting phase. A copper (100) seed crystal was placed in a graphite crucible. A second seed with a cylindrical geometry was grown into the original seed crystal (disc) and thereafter the sample of rectangular geometry was grown into the cylindrical seed (fig 3.1).

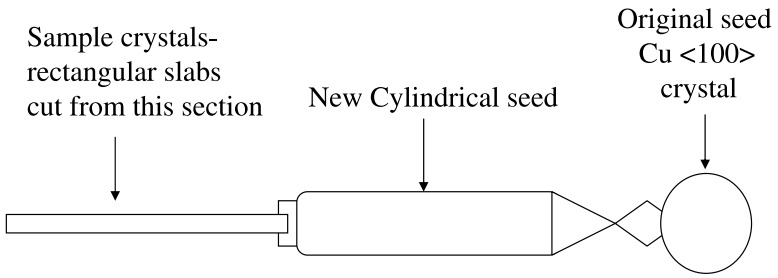


Figure 3.1: Schematic diagram of growth capsule for Cu and Cu-Ni targets used in this study (shown here in 2-D).

At each preparation step an x-ray diffraction pattern was taken to monitor the orientation of the copper and Cu/Ni metal crystal sections that were grown. A typical (100) pattern was observed at all times. The rectangular cross section was cut using a diamond saw, into 8.0 mm lengths. The $8 \times 4 \times 3\,\mathrm{mm}^3$ slabs were individually mechanically polished by hand on one side using 0.01 μm Al_2O_3 powder mixed in distilled water on a percale cotton sheet. When a satisfactorily flat finish was attained the samples were electropolished in a Buhler electromet system. Each sample was treated for 2-3 minutes on the mechanically polished side in an electrolyte solution of orthophosphoric acid and copper carbonate in the electropolishing cell. A voltage of 15-20 V was maintained in the cell during this procedure. The crystals were rinsed in methanol and dried on lint free cloth. Upon observation the samples appeared flat with a mirror finish, but closer inspection under an optical microscope revealed etch pits on the surface which were probably induced during the electropolishing procedure. The polished surfaces of each of the crystals was examined using low energy electron diffraction (LEED), to determine any surface orientation. None was observed on any of the surfaces prior to implantation.

3.3.2 The end station

Each of the samples were mounted in an unique end station target holder. The end station was designed with a sample heater and a filament heater. A gas feedthrough allowed e.g. water vapour, acetone vapour, H_2 and CF_4 etc. to pass over the filament heater. The filament heater was constructed out of thin tungsten wire. A voltage of 35.0 V was applied to this filament. This made it 'white' hot, which is typically observed at thermionic emission. The filament heater was positioned near the front end of the target holder such that any gas being passed into the end station would be ionised by the electrons that are emitted by the filament. The sample heater (resistive element heater) onto which the sample was mounted could heat the sample up to 1000.0 °C. A water cooled jacket surrounded the sample heater. A voltage feedthrough allowed the sample heater to be biased. In the initial experiments described here, this voltage was

-15.0 V. The proximity of the heater bias in relation of the target surface and filament heater was such that any gas that was ionised by the filament heater would be attracted towards the sample and thereby increase the probability of interaction of the ionised gases with the sample surface. A second bias voltage was applied onto a ring which was in front of the target and filament heater. A negative bias of 10.0 V was applied to this ring during the implantation procedure. Its position was such that electrons emitted from the filament heater would be repelled back towards the target surface, and consequently increase the probability of it ionising the gas being fed into the end station. For the data presented, a selected gas or vapour was continuously admitted into the target holder during implantation or annealed in the chosen gas for 1 hour before implantation.

3.3.3 The implantation conditions

The implantations were performed on a Varian 200-20A2F ion implanter at the Schonland Research Institute for Nuclear Sciences. The energy of the accelerated carbon ions was 120 keV. The dose rate ranged between 3 to 6 μA. The total dose implanted for all targets was 5×10^{17} $^{12}C^{+}.cm^{-2}$. Different gases and target temperatures were utilized in this initial study. The implantation conditions for a selected number of targets are summarized in table 3.2. Several other implantations were carried out and the results of these carbon overgrowths are not shown in this work. This is primarily because the results obtained do not differ significantly from the selected data that is presented.

Prior to implantation the target was heated by the sample heater to a specific temperature. Two thermocouples were used to monitor the target temperature during implantation. The back thermocouple monitored the base of the sample heater, while the front thermocouple was positioned to monitor the target temperature. The target was heated to some temperature and held at this temperature for approximately an hour. In some cases the filament heater was switched on at thermionic emission with the bias voltages switched on and a specific gas was admitted into the end station target holder. The base pressure of the ion implanter end station was $1 - 2 \times 10^{-6}$ mbar.

The micrometer fine control valve along the gas feedthrough was opened to admit a selected gas over the filament heater. It was adjusted so that the end station pressure was maintained at some specific pressure within the range $1 \times\ 10^{-5} - 5 \times\ 10^{-6}$ mbar.

3.4 Analysis of the carbon overgrowths

From previous observations made by Prins and Gaigher, it was decided not to etch the carbon layers away from the metal crystals, since the overlayers are extremely thin and tend to fragment to small sections which become difficult to handle. Auger electron spectroscopy and Raman spectroscopy was used to determine the nature of the overlayers that resided on the Cu and Cu-Ni samples. Upon inspection under an optical microscope the surfaces of samples Cu11, 20005 and 20006 showed evidence of overlayers that were not present prior to the implantation process. The samples implanted with the hydrogen plasma (20002-20004) did not show any obvious evidence of an overlayer. The Auger spectrometer used was the VG Scientific CLAM100 system with a hemispherical analyzer. Before analysis of the implanted targets, the spectra shown in fig. 3.2 were collected to act as a calibrant to assess the difference we would observe for sp^2 and sp^3 bonded carbon for the CLAM100 spectrometer. All spectra

Sample	Filament current (A)	Gas pressure (mBar)	Crystal (100)	Front temp. (°C)	Back temp. (°C)	Heater current (A)
Cu11	3.02	2×10^{-5} Acetone	Cu	700.0	728.0	4.94
20002	3.10	1.5×10^{-5} H_2	Cu	705.0	694.0	2.88
20003	3.04	9×10^{-6} H_2	Cu-Ni	608.0	518.0	1.61
20004	2.76	7×10^{-6} H_2	Cu	510.0	343.0	0.0
20005	3.07	2×10^{-5} CF_4	Cu	580.0	747.0	3.32
20006	3.06	3×10^{-5} CF_4	Cu-Ni	650.0	611.0	2.40

Table 3.2: Implantation parameters used for the data presented in this chapter. In all of the cases above a bias voltage of -10.0 V and -15.0 V was applied to the filament and heater respectively. Take note that the gas pressure column is the pressure measured in the end station of the implanter and is not the pressure of the gas that is fed into the target holder end station.

were collected with a sinusoidal voltage of $\pm 5.0\,\mathrm{V}$ applied over the analyzer i.e. electronic differentiation took place. Care was taken to ensure that the primary beam or sinusoidal voltage did not significantly change the peak position (sample charging) or alter the lineshape of the Auger spectra.

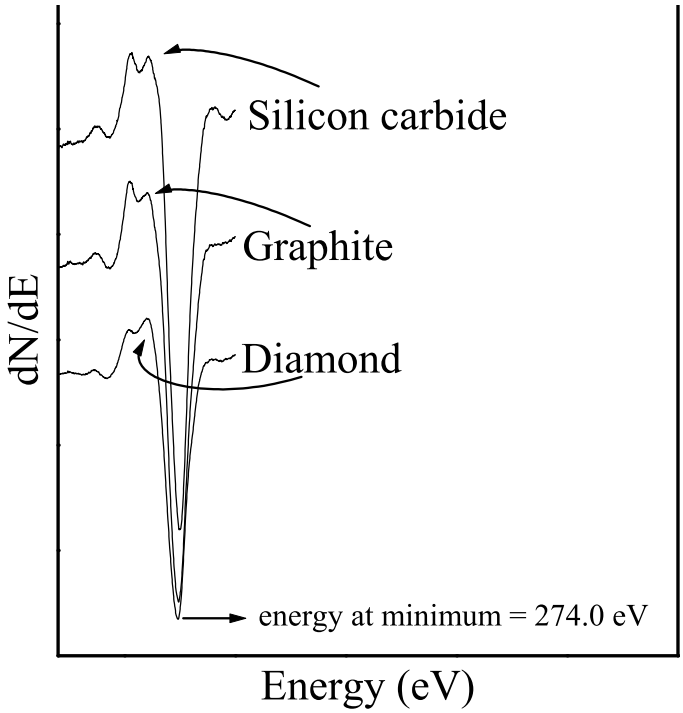


Figure 3.2: Auger spectra obtained for graphite, a synthetic Ib diamond and SiC samples. The arrows indicate one of the primary features that distinguishes sp^2 from sp^3 bonded carbon. The saddle on the lineshape shows a high energy shoulder for sp^3 bonded carbon (diamond and silicon carbide), while the graphite sample has this shoulder slightly lower.

The Raman setup details have been described earlier in section 3.2. The Raman and Auger spectra for sample Cu11 and 20003 are shown in figures 3.3 to 3.6. The spectra for the other samples listed and those not listed show similar features to the spectra of samples cu11 and 20003 respectively and are not shown here.

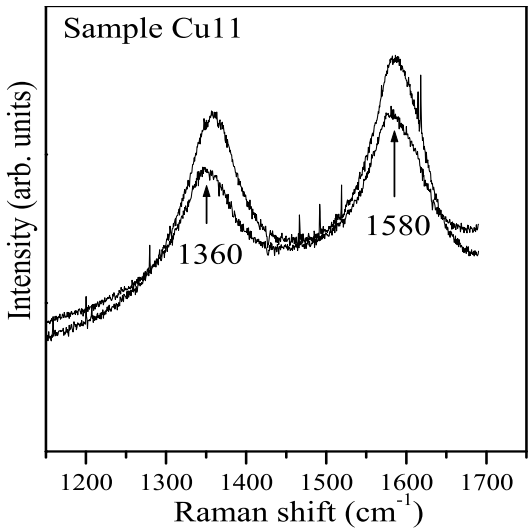


Figure 3.3: Raman spectrum obtained for the carbon overlayer that was generated by the implantation conditions listed in table 3.1. The Raman spectrum reveals that the carbon has no diamond structure, but has the signatures for disordered carbon (D-band) and polycrystalline graphite (G-band).

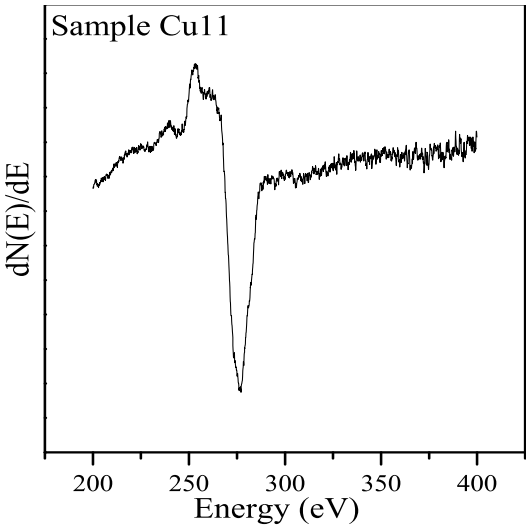


Figure 3.4: Auger spectrum obtained for the carbon overlayer that was generated by the implantation conditions listed in table 3.1. The Auger lineshape reveals that the carbon has no diamond structure, but has the characteristic lineshape observed for sp^2 bonded carbon.

3.5 Conclusions

These initial results did not reveal any specific conditions that may lead to diamond growth. An interesting point to consider was the data obtained for the sample implanted with a hydrogen plasma. It appears that most of the carbon that segregates to the surface forms sp^2 bonded carbon. The action of the hydrogen near the sample surface would be to remove this carbon. This is similar to what occurs in CVD processes of diamond growth [16]. We hope in the near future to look at the possible parameters that may deliver a sp^3 network of carbon atoms using this unique end station. This will hopefully lead to a seeding system that will deliver single crystal diamond using CVD methods. The use of CF_4 gas in the experimental end station described earlier is of particular interest as it may lead to the formation of fluorinated amorphous carbon (a-C:F). This material has a low dielectric constant and has useful applications in

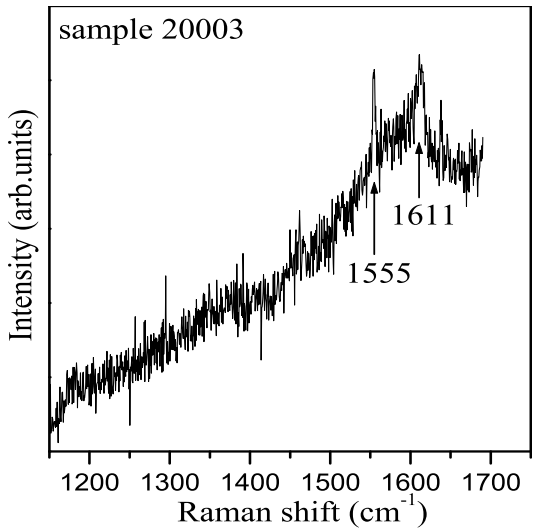


Figure 3.5: Raman spectrum obtained for the carbon overlayer that was generated by the implantation conditions listed in table 3.1. The Raman spectrum reveals that the carbon has no diamond structure. The additional Raman features that appear in the Raman spectrum of this sample is tentatively ascribed to carbon (graphite crucible used) that probably reacted with the Cu-Ni alloy during the melting since these features also appeared in the unimplanted Cu-Ni samples. It is well documented that carbon chemically reacts with Ni to form nickel carbides at low pressure [9–12].

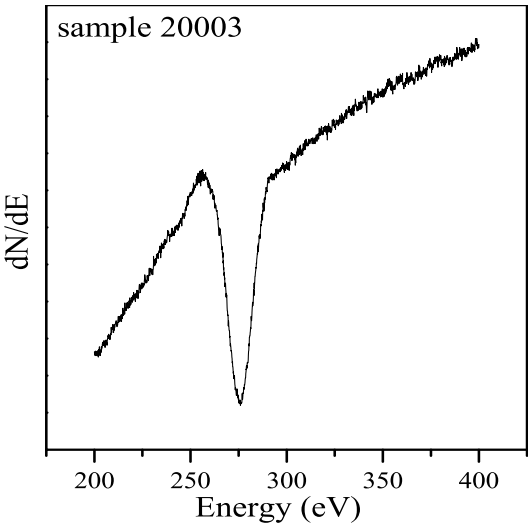


Figure 3.6: Auger spectrum obtained for the carbon overlayer that was generated by the implantation conditions listed in table 3.1. The Auger lineshape reveals that the carbon has no diamond structure. It is highly probable that most of carbon from the implantation process was removed by the hydrogen plasma if we assume that the carbon diffused to the surface of the implanted substrate to form sp^2 bonded carbon.

future ultra large scale integrated circuits [123, 133].

Chapter 4

Raman Studies on CIRA processed Diamonds

4.1 Introduction

Diamond is coveted for its extreme properties which make it suitable for semiconductor application in adverse environments. At present one of the best means for introducing dopants into this wide band gap material has been achieved by ion implantation [17]. Ion implantation however also introduces radiation damage (isolated point defects and extended defects) that compensates the impurity level of the active dopants [149, 150]. The defects which give rise to these impurity levels are dependent on the implantation energy, temperature, dose, dose rate and the subsequent annealing temperatures. Raman spectroscopy has proven to be a useful technique on assessing the radiation damage as a result of the implantation process in diamond. The defects that are detectable by Raman spectroscopy as a result of the radiation damage induced by the implantation annealing process, are not a complete description of all the defects that have been created during the process. It nonetheless serves as a useful non-destructive diagnostic tool that has added an immense volume of information on defects in diamond. In single-crystal diamond the Raman scattering spectrum is dominated by a single intense peak at $\pm$ 1332 cm^{-1} [119]. The implantation-annealing process introduces point defects which alters the vibrational density of states near and within the implanted region, which gives rise to a number of defect peaks in the Raman spectrum

and alters the lineshape and peak position of the $1332\,\mathrm{cm}^{-1}$ diamond peak [13]. In the present work, carbon ions in the keV range were implanted into a single-crystal diamond and the Raman scattering spectra were recorded as a function of implantation dose and annealing temperature. The defects produced were compared to those produced by MeV ion implantation where it was claimed at the time that MeV implantation gave rise to unique Raman signatures that are not observed in keV implanted diamond. The work produced in this chapter was the first to show that this is not the case.

4.2 Experimental considerations

A single-crystal natural IIa diamond $8.25 \times 3 \times 2\,\mathrm{mm}^3$ was implanted at liquid nitrogen ($\mathrm{LN}_2 \approx -196\,^{\circ}\mathrm{C}$) temperature with the doses and energies shown in table 4.1. Similar dose steps and implantation energies have been used previously for obtaining good quality p-type layers by boron implantation. The choice of carbon ions was to monitor the changes due to radiation damage and exclude any changes to foreign atom bonding in the diamond crystal. The implanted face was polished in the {100} direction and boiled in an oxidising acid solution prior to the implantation step discussed above. The diamond was mounted on a sample holder which had a device that could move a mask over the diamond surface. The target holder was oriented 7° to the normal incidence of the beam in order to reduce any channelling effects. A dose rate of $\approx 10^{13}\,\mathrm{ions.s}^{-1}.\mathrm{cm}^{-2}$ was used in all of the implantation steps. For a beam energy of 37 - 170 keV of near normal incidence and low dose rate we can assume that sputtering effects at the surface of the diamond will be neglible [151]. Diamond is an insulator and will charge up due to secondary electrons being emitted from the near surface after being struck by an energetic ion. The surface charge induced will have an impact on the energy of the emitted electrons, but not significantly change the energy of the incoming ions. The potential due to surface charging has been measured to be near 1 kV for most diamond surfaces. Therefore all changes observed in the Raman spectrum will be attributed to the energy losses of the implanted ion below the diamond surface and not to any

surface induced charging caused by the impinging ion.

Energy (keV)	Dose ($\times 10^{14}$ ions/cm^2)				
170	0.375	1.5	1.875	15	18.75
140	0.125	0.5	0.625	5	6.25
128	0.0625	0.25	0.3125	2.5	3.125
116	0.0625	0.25	0.3125	2.5	3.125
103	0.0625	0.25	0.3125	2.5	3.125
90	0.0625	0.25	0.3125	2.5	3.125
77	0.0625	0.25	0.3125	2.5	3.125
64	0.0625	0.25	0.3125	2.5	3.125
51	0.0625	0.25	0.3125	2.5	3.125
37	0.0625	0.25	0.3125	2.5	3.125
	step 1→step 2→step 3→step 4→step 5				

Table 4.1: Ion energies and doses used for the C^+ ion implantation in a type IIa diamond. According to the TRIM simulation program, the chosen ion energies and doses create a uniformly damaged layer to a maximum depth of $\approx 0.23\,\mu$m below the surface of the implanted face (see fig. 4.2). A moveable mask was first moved ≈ 1.0 mm down over the top edge of the diamond. This unimplanted region was used to monitor the virgin spectra after each annealing step. The remaining face was implanted with the dose fractions of step 1. The mask was then moved ≈ 1.5 mm down further over the diamond. The remaining exposed surface was implanted with the parameters of step 2. The mask was moved a further 1.5 mm and the remaining surface of the diamond was implanted with the dose fractions of step 3. The procedure continued until the diamond had been implanted with the dose fractions of step 4 and step 5 with the mask travelling 1.5 mm down after each step. Each dose column thus represents the dose fractions implanted at the various energies for regions 1 to 5. This procedure is schematically shown in fig. 4.1.

A moveable mask was first moved ≈ 1.0 mm down over the top edge of the diamond. This unimplanted region was used to measure the virgin spectra after each anneal. The first step implanted a total dose of 1×10^{14} ions/cm^2 over the entire remaining face. The mask was then moved a distance of 1.5 mm over the diamond surface and a second irradiation of 4×10^{14} ions/cm^2 was implanted on the diamond, so that the total dose implanted on the remaining exposed region was now 5×10^{14} ions/cm^2. The mask was moved a further 1.5 mm and a dose of 5×10^{14} ions/cm^2 was implanted on the exposed surface. The procedure continued until we had implanted five different regions

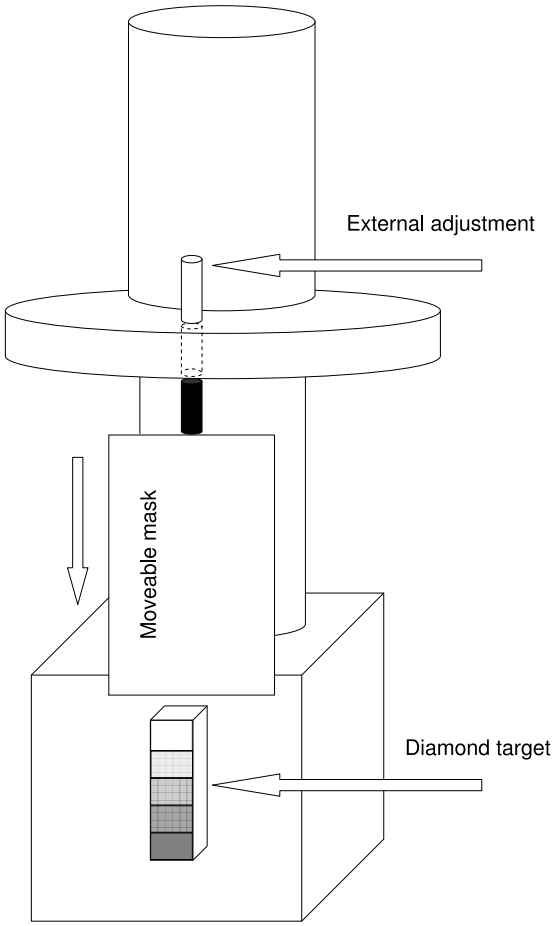


Figure 4.1: Schematic drawing of the specifically designed sample holder to achieve the five different implanted regions for the parameters outlined in table 4.1. The travelling mask could be adjusted downwards and the external adjustment was outside the vacuum system of the end station of the ion implanter. After each implantation step the mask was moved 1.5 mm down until five regions with five different doses were implanted on the face of the type IIa diamond. The shaded regions indicate the different regions with the darkest region symbolizing the area that received the highest dose.

on the diamond each with increasing dose. It follows that region 1 had the lowest total dose, 1×10^{14} ions/cm^2 and region 5 had the highest total dose, 1×10^{16} ions/cm^2. The procedure is aptly outlined within figure 4.1 and table 4.1. The diamond was held at liquid nitrogen temperature while it was removed from the implantation holder and then rapidly annealed to 500 °C for 1 hour in a preheated graphite crucible. The annealing cell was flushed with argon and details of the annealing apparatus setup is

described elsewhere [17]. The diamond was allowed to cool to room temperature and thereafter cleaned with contrad in an ultrasonic bath and rinsed with distill water.

The Raman analysis was carried out on a Jobin-Yvon T64000 spectrometer in single spectrograph mode with a holographic notch filter to remove the Rayleigh scattered light and a holographic grating of 1800 grooves/mm to disperse the light onto a liquid nitrogen-cooled Spectrum One CCD detector. The spectral range of this grating was 650 cm^{-1} and the resolution was 0.62 cm^{-1}/pixel. The slit width was 50.0 μm. An Olympus B×40 confocal microscope was attached to the instrument and an objective of magnification 100× and aperture 0.9 were used to focus the laser light onto the surface to a spot size of $\pm$2.0 μm. The sample was placed on a motorized XY MIDI stage which enabled reproducible positioning of the laser spot on the five different areas between different annealing stages. All of the spectra were measured at the same position in each of the areas irrespective of the annealing cycle. The confocal pinhole size was 0.1 mm. The sample depth to which the laser will penetrate a transparent diamond with the above confocal setup is $\pm$2.5 μm. The excitation radiation used was the 514.5 nm line of a Coherent Innova 308 Argon ion laser, power 100 mW. The mercury green emission line at 1122.47 cm^{-1} with respect to the 514.5 nm argon ion laser line was recorded with each Raman spectrum collected. The mecury line was used for calibration of the observed Raman shift. Two sets of spectra were collected on the same spot in each area. For one set the integration time was 15 s with three spectra being averaged; for the other set the integration time was 120 s with two spectra being averaged.

The diamond was further annealed for 1 hr at 650, 800, 950, 1100, 1400 °C. This implantation-annealing sequence will be referred to as cycle A. After each anneal the diamond was cleaned using contrad in an ultrasonic bath and rinsed in distilled water and then the Raman spectrum was recorded for each region. The diamond was not cleaned by boiling in an oxidising acid solution in any of the annealing cycles since this would have etched away the implanted layer if it had been graphitized by the implanted

dose at the annealed temperature.

The diamond was then polished to remove traces of the previous implanted layer and cleaned by boiling in an oxidising acid solution [17] and rinsed in distilled water. The same implantation process was carried out, but this time the rapid temperature anneal was to room temperature (RT). The Raman spectrum for each region was recorded as before and after subsequent anneals at 500, 650, 800, 950, 1100 and 1400 °C. This implantation-annealing sequence will be referred to as cycle B. The diamond was polished and cleaned and the same implantation steps were performed and this time the diamond was at room temperature during the implantation process. The Raman spectrum was recorded as before and after annealing at 200, 300, 500, 650, 800, 950, 1100 and 1400 °C. This implantation-annealing sequence will be referred to as cycle C. The diamond was polished and cleaned as before and a further implantation-annealing sequence was performed, only this time the implantation was done at a single energy of 100 keV with the same total doses used in cycles A, B and C. The diamond was held at room temperature during the implantation. The Raman spectra were recorded from ambient and after annealing for 1 hour at 300, 500, 650, 800, 950, 1100 and 1400 °C. This implantation-annealing sequence will be referred to as cycle D. The 4 cycles and implantation parameters are summarized in table 4.2.

4.3 Results

The implantation doses and energies as shown in table 4.1 for cycle A, B and C were chosen to create a uniformly damaged layer below the surface of the diamond to a depth of approximately 0.23 μm [fig. 4.2]. The parameters were chosen such that the implanted ion has an increased probability of encountering a carbon self-interstitial during the annealing process, and at the same time reducing the density of vacancies that were created during the implantation process. In order to reduce the interstitial migration during the implantation process the implantation was carried out at low temperatures for cycles A and B [CIRA process: section 2.3.3].

	Cycle A	Cycle B	Cycle C	Cycle D
Energy (keV)	See Table 4.1	See Table 4.1	See Table 4.1	100
Target Temp. (°C)	LN_2	LN_2	RT	RT
Dose (ions/cm^2)	See Table 4.1	See Table 4.1	See Table 4.1	1×10^{14} $\rightarrow 5 \times 10^{14}$ $\rightarrow 1 \times 10^{15}$ $\rightarrow 5 \times 10^{15}$ $\rightarrow 1 \times 10^{16}$
Annealing Cycle (°C)	$LN_2 \rightarrow$ 500 $\rightarrow$650$\rightarrow$800 $\rightarrow$950$\rightarrow$1100 $\rightarrow$1400	$LN_2 \rightarrow$RT $\rightarrow$500$\rightarrow$650 $\rightarrow$800$\rightarrow$950 $\rightarrow$1100$\rightarrow$1400	RT$\rightarrow$200 $\rightarrow$300$\rightarrow$500 $\rightarrow$650$\rightarrow$800 $\rightarrow$950$\rightarrow$1100 $\rightarrow$1400	RT$\rightarrow$300 $\rightarrow$500$\rightarrow$650 $\rightarrow$800$\rightarrow$950 $\rightarrow$1100$\rightarrow$1400

Table 4.2: Summary of the implantation parameters and annealing cycles used in this Raman study. Note that the doses indicated for cycle D is the total implanted dose for the 5 regions on the diamond surface. The same sample holder was used as in cycles A, B and C to generate the five regions. The difference being for cycle D was the total dose of step 1 was implanted at 100 keV over the entire surface of the diamond after which the mask was adjusted downwards by 1.5 mm. The total dose of step 2 was then irradiated on the remaining surface of the diamond at 100 keV and the mask was again moved downwards by 1.5 mm. This process procedure was carried out up to step 5, keeping the energy at 100 keV, to complete the 5 regions of increasing dose as indicated in for cycle D.

As outlined in the previous section we have used 4 different implantation-annealing cycles in this study. For cycles A and B implantations were done at liquid nitrogen temperature with the total dose implanted over a wide width, while cycle C was implanted at room temperature over a wide width whereas cycle D was implanted at ambient temperature with the total dose implanted at a single energy which results in the implanted profile occupying a narrower width. The TRIM estimation of the damage profile for the implantation parameters of cycle D is shown in fig. 4.3. Based on the calculations of Uzan-Saguy *et al* [105] it is shown that the implanted dose for regions 1, 2 and 3 are below the critical dose D_c to achieve an average vacancy density above 1×10^{22} vac/cm^3. Regions 4 and 5 are implanted with a dose that creates an average vacancy density above 1×10^{22} vac/cm^3. Note that the units of the y-ordinate for the TRIM simulation profiles in this text are shown in vac/cm^3.

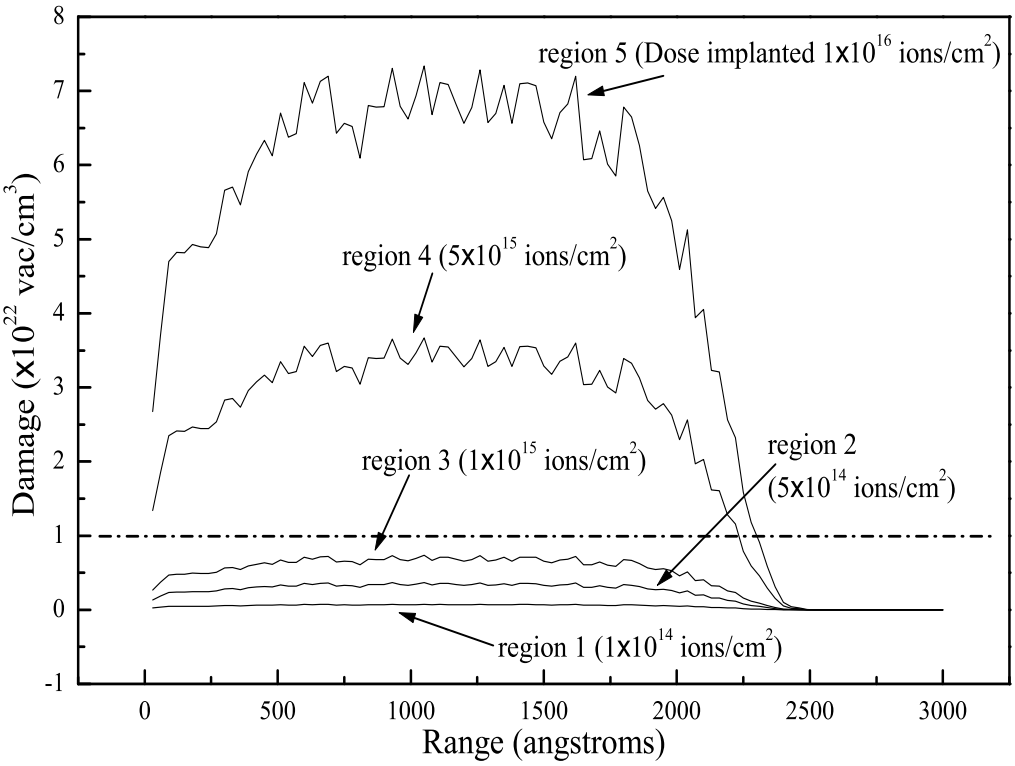


Figure 4.2: TRIM simulation of the damage profile for the implantation parameters used in cycles A, B and C in this study. The damage distribution is spread over a width of $\approx 0.23\,\mu$m. The dashed line is drawn at a vacancy density of $1 \times 10^{22}\,\mathrm{vac/cm^3}$.

Prior to implantation the diamond showed a well defined diamond peak centred at $1331\,\mathrm{cm^{-1}}$ [fig. 4.4].

After irradiation the Raman scattering spectra obtained for regions 1 to 4 gave rise to defect peaks near 1450, 1498, $1638\,\mathrm{cm^{-1}}$. These peaks were observed irrespective of the implantation-annealing sequences employed in this study. Region 5, which received the highest dose, had a broad band centred around 1550-$1580\,\mathrm{cm^{-1}}$. All of the Raman spectra obtained for each of the implantation-annealing cycles are shown in figures 4.5 - 4.25. The spectra show only the region of interest and the length of the intensity scale has been chosen to be the same for each of the graphs within a specific set. The sloping background observed in most of the spectra is due to photoluminescence (PL)

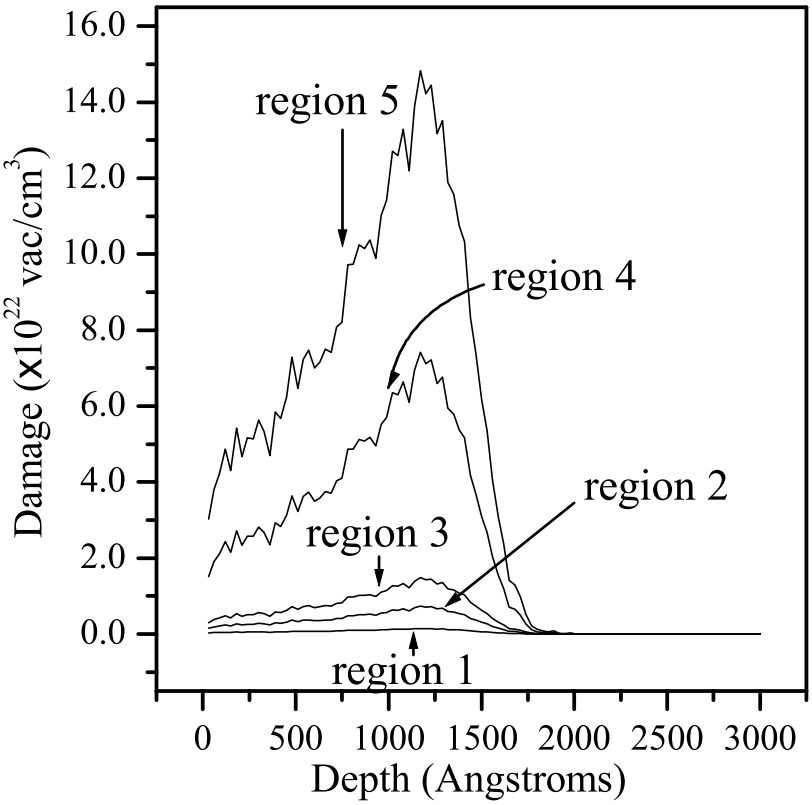


Figure 4.3: TRIM simulation of the damage profile for the implantation parameters used in cycle D (100 keV). The damage distribution is spread over a width of $\approx 0.15\,\mu$m. According to TRIM the damage distribution reaches a maximum near $\approx 0.12\,\mu$m. The average vacancy density for regions 1-2 is below $1 \times 10^{22}\,\mathrm{vac/cm^3}$. For region 3 it is mostly below $1 \times 10^{22}\,\mathrm{vac/cm^3}$, whereas regions 4 and 5 have an average vacancy that is primarily above $1 \times 10^{22}\,\mathrm{vac/cm^3}$.

which is typically observed for Raman spectra for the visible wavelength used in this analysis. It is particularly enhanced in these spectra because the vertical scale has been chosen to highlight the defect peaks which are small in intensity compared to the diamond Raman line. Selected virgin spectra are also shown for different annealing temperatures. No background subtraction has been used in any of the Raman spectra shown in this chapter. Specific spectra which show more clearly the Raman peaks and their peak positions are highlighted further on in section 4.4.

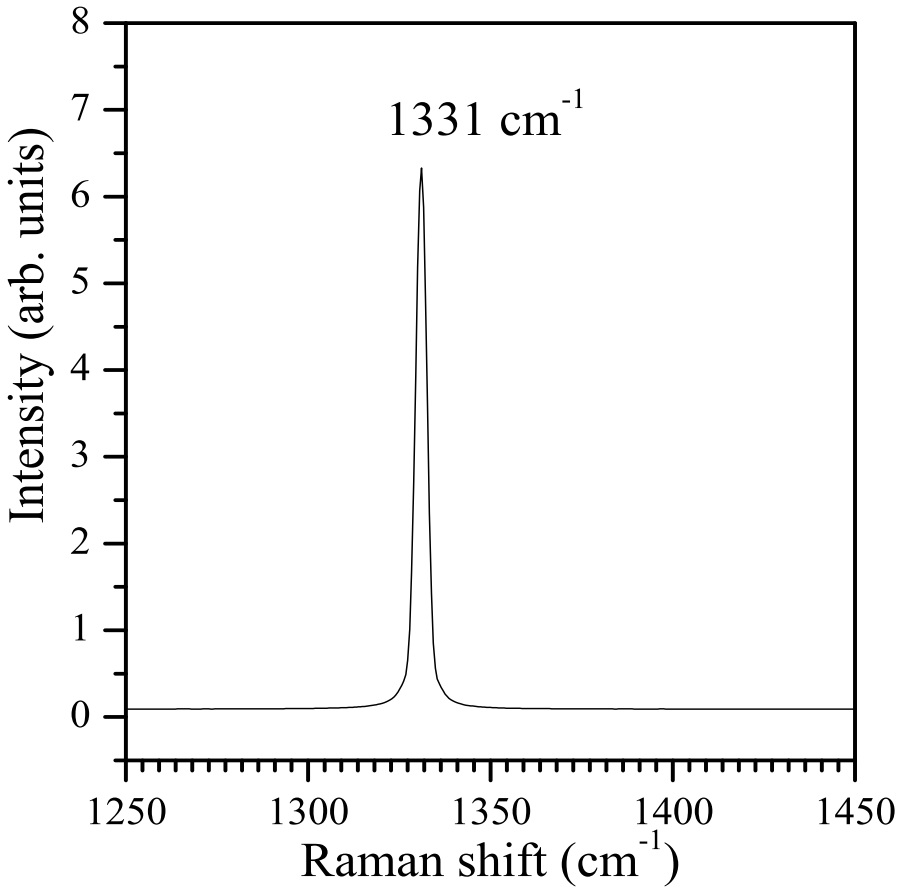


Figure 4.4: Raman spectra obtained for the unimplanted diamond used in this study. The typical diamond line centred at 1331 cm^{-1} with a line width 2.9 cm^{-1} was observed after each implantation-annealing cycle.

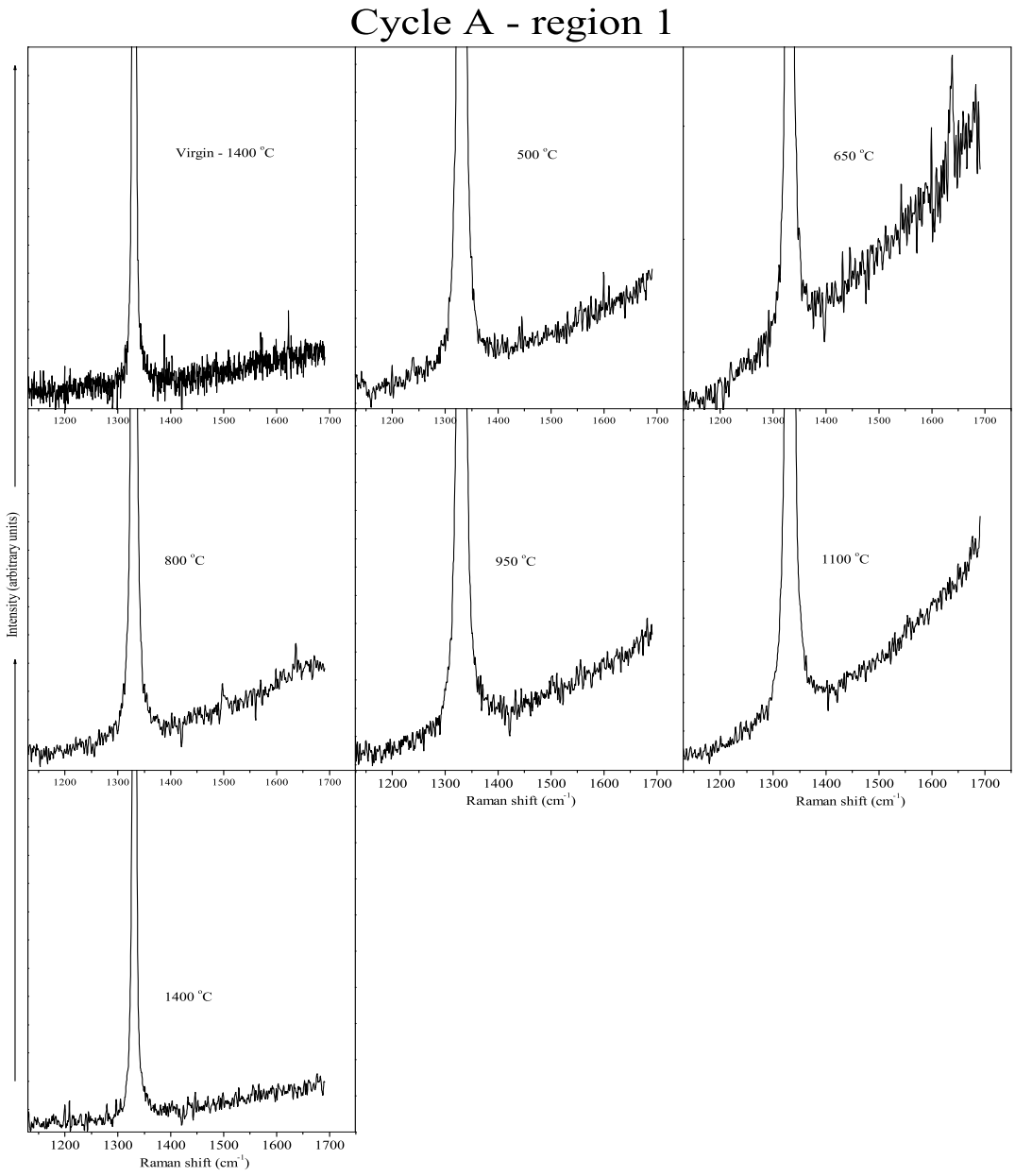


Figure 4.5: Raman spectra obtained for the implanted diamond in cycle A - region 1. The implanted dose is less than D_c. Evidence of the 1638 cm^{-1} peak is present after annealing at 650 °C while the 1498 cm^{-1} peak is present but not well defined after annealing at 800 °C. No Raman active defect peaks are visible after annealing at 950 °C.

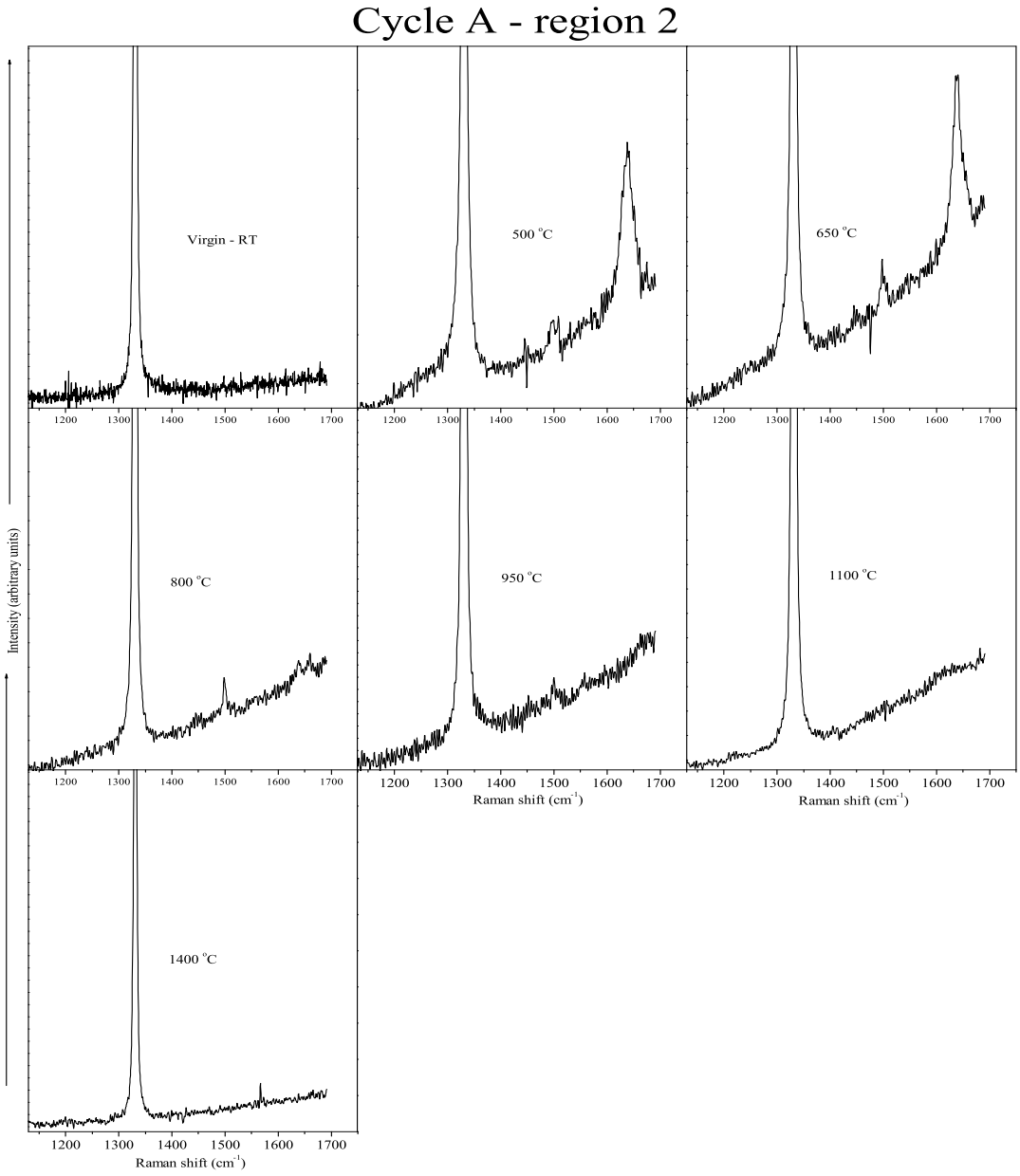


Figure 4.6: Raman spectra obtained for the implanted diamond in cycle A - region 2. The implanted dose is less than D_c. Evidence of the 1638 cm^{-1} peak and the 1498 cm^{-1} peak is present after annealing at 500 °C. No Raman active defect peaks are clearly visible after annealing at 950 °C.

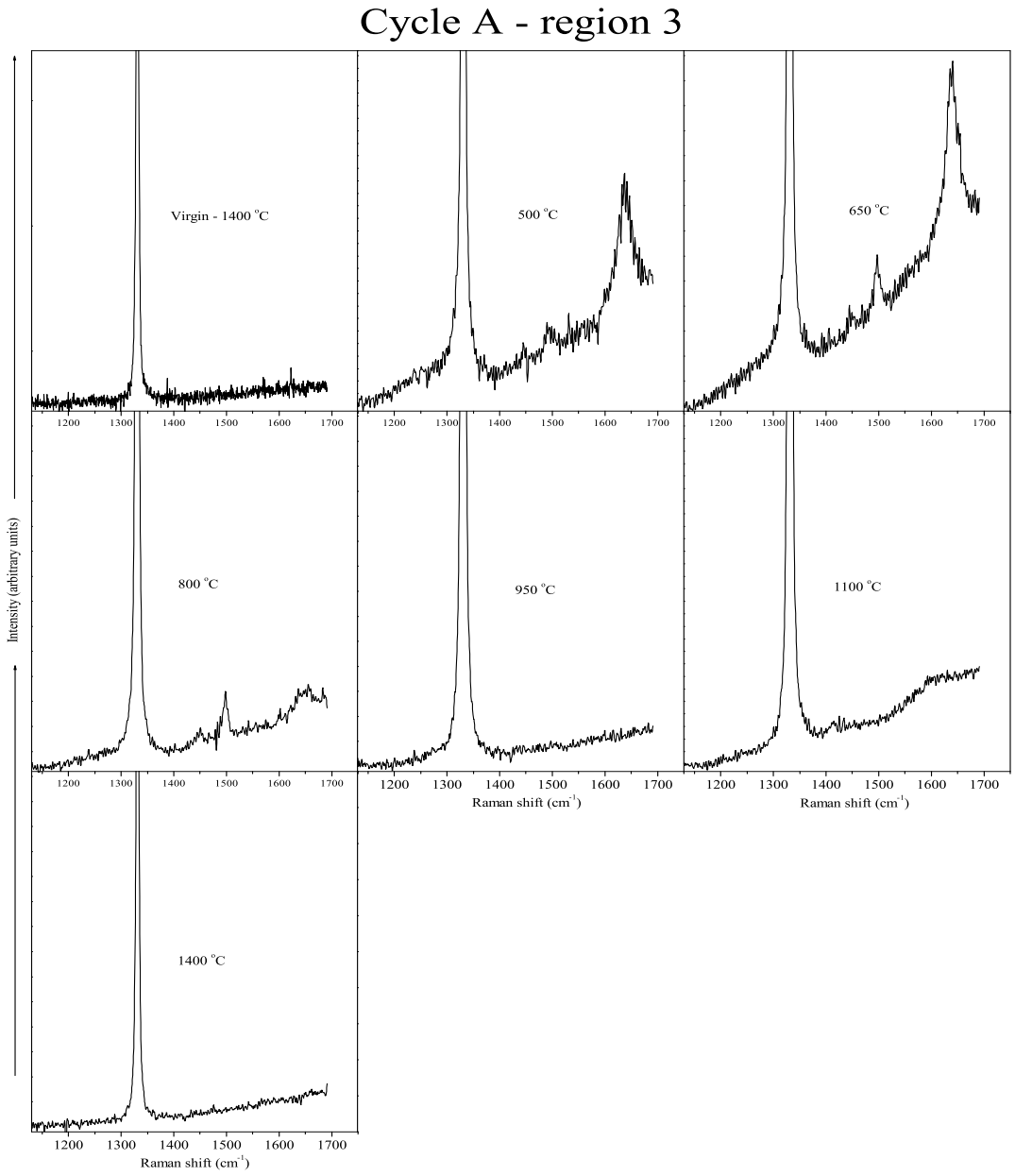


Figure 4.7: Raman spectra obtained for the implanted diamond in cycle A - region 3. The implanted dose is less than D_c. Evidence of the 1638 cm^{-1} peak and the 1498 cm^{-1} peak is present after annealing at 500 °C. No Raman active defect peaks are clearly visible after annealing at 950 °C.

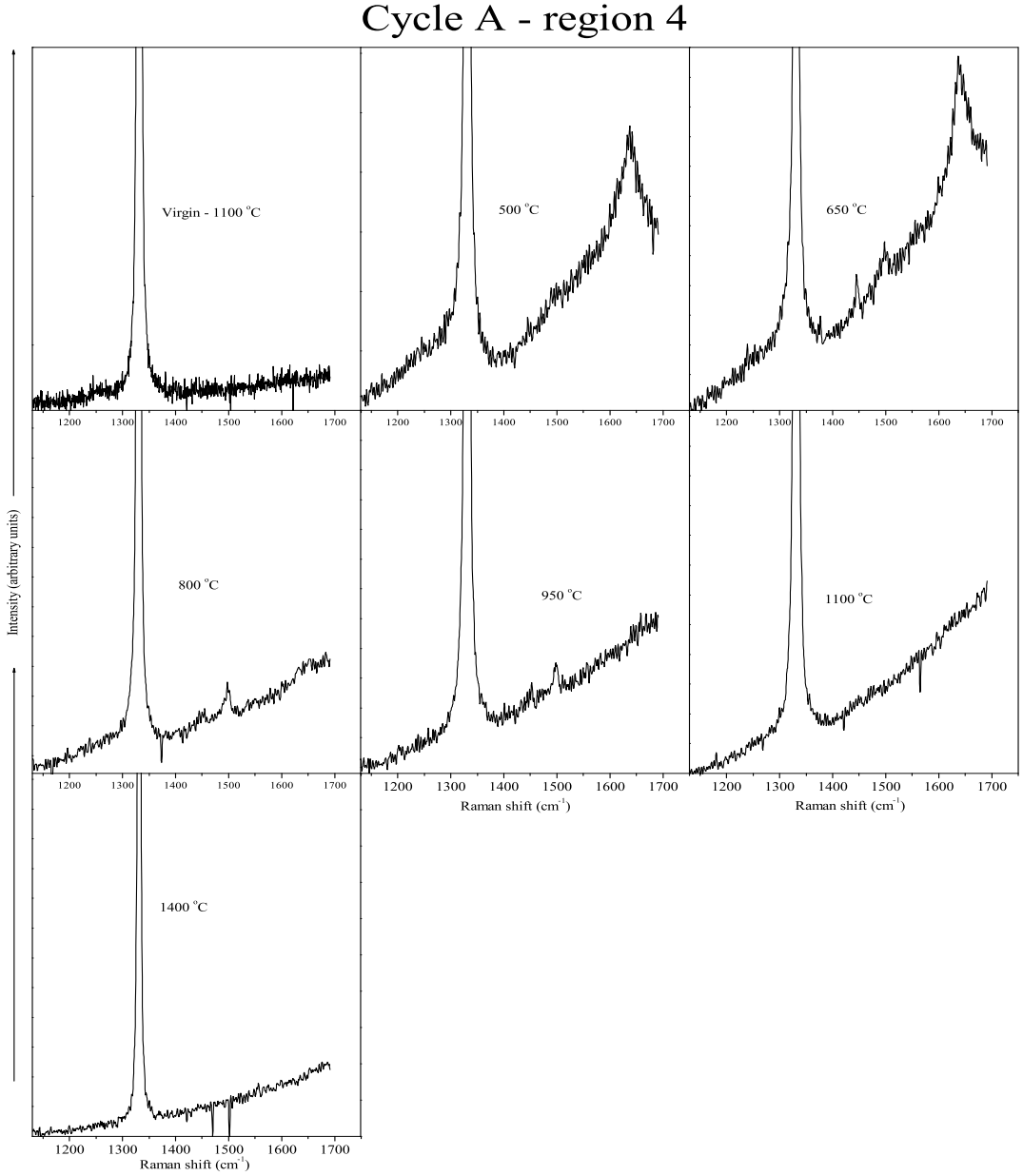


Figure 4.8: Raman spectra obtained for the implanted diamond in cycle A - region 4. The implanted dose is greater than D_c. Evidence of the 1638 cm^{-1} peak is present after annealing at 500 °C while the 1498 cm^{-1} peak is more clearly defined after the 650 °C anneal. The 1498 cm^{-1} defect peak is now still present after annealing at 950 °C. No Raman active defect peaks are present after annealing at 1100 °C.

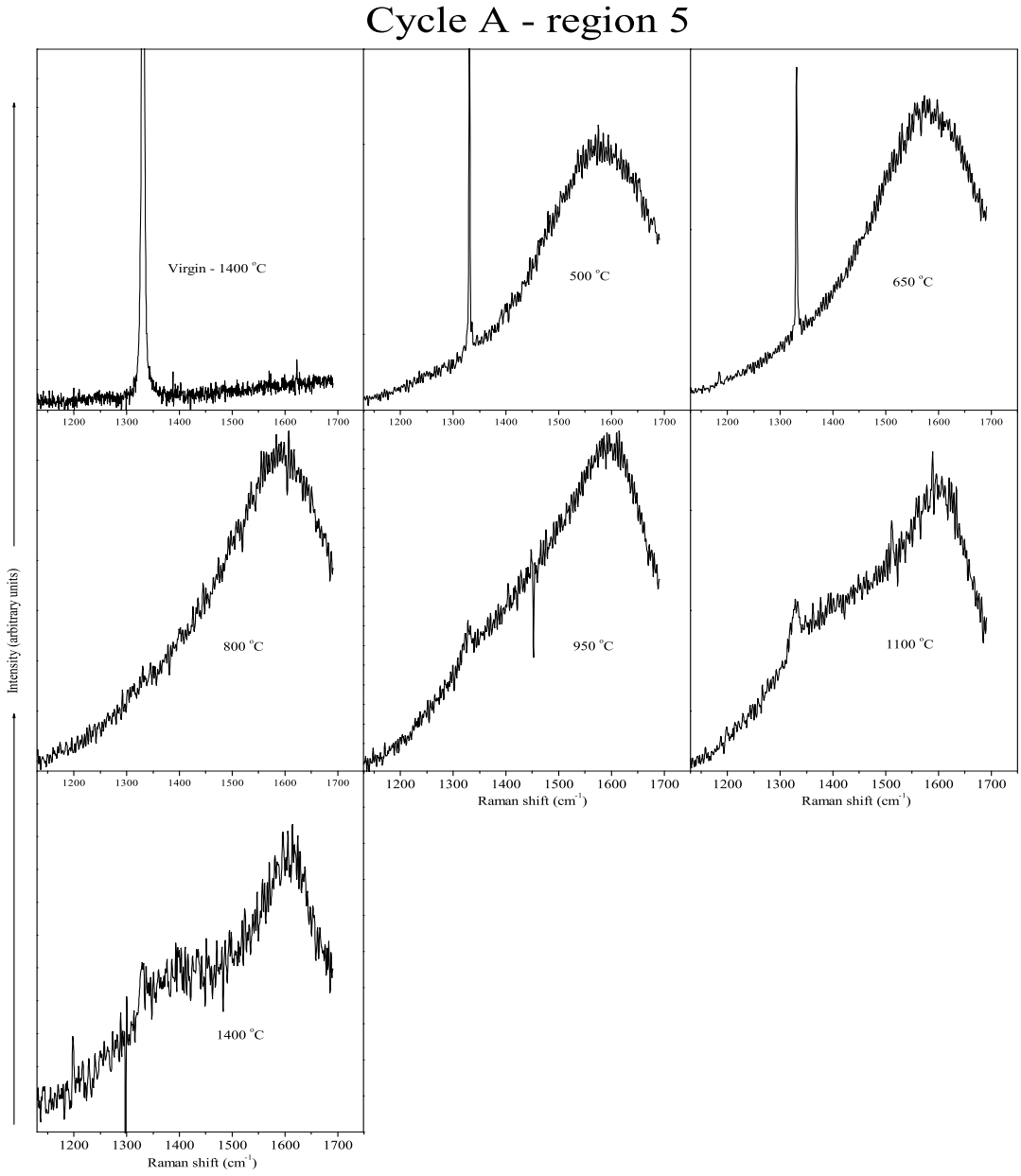


Figure 4.9: Raman spectra obtained for the implanted diamond in cycle A - region 5. The implanted dose is greater than D_c. No evidence of the 1638 cm^{-1} peak and the 1498 cm^{-1} peak is present after annealing at 500 °C. The spectra are dominated by a broad band centred around 1550-1580 cm^{-1} which indicates that the implanted - annealed layer consists of disordered graphite. The diamond line is barely visible after annealing at 800 °C.

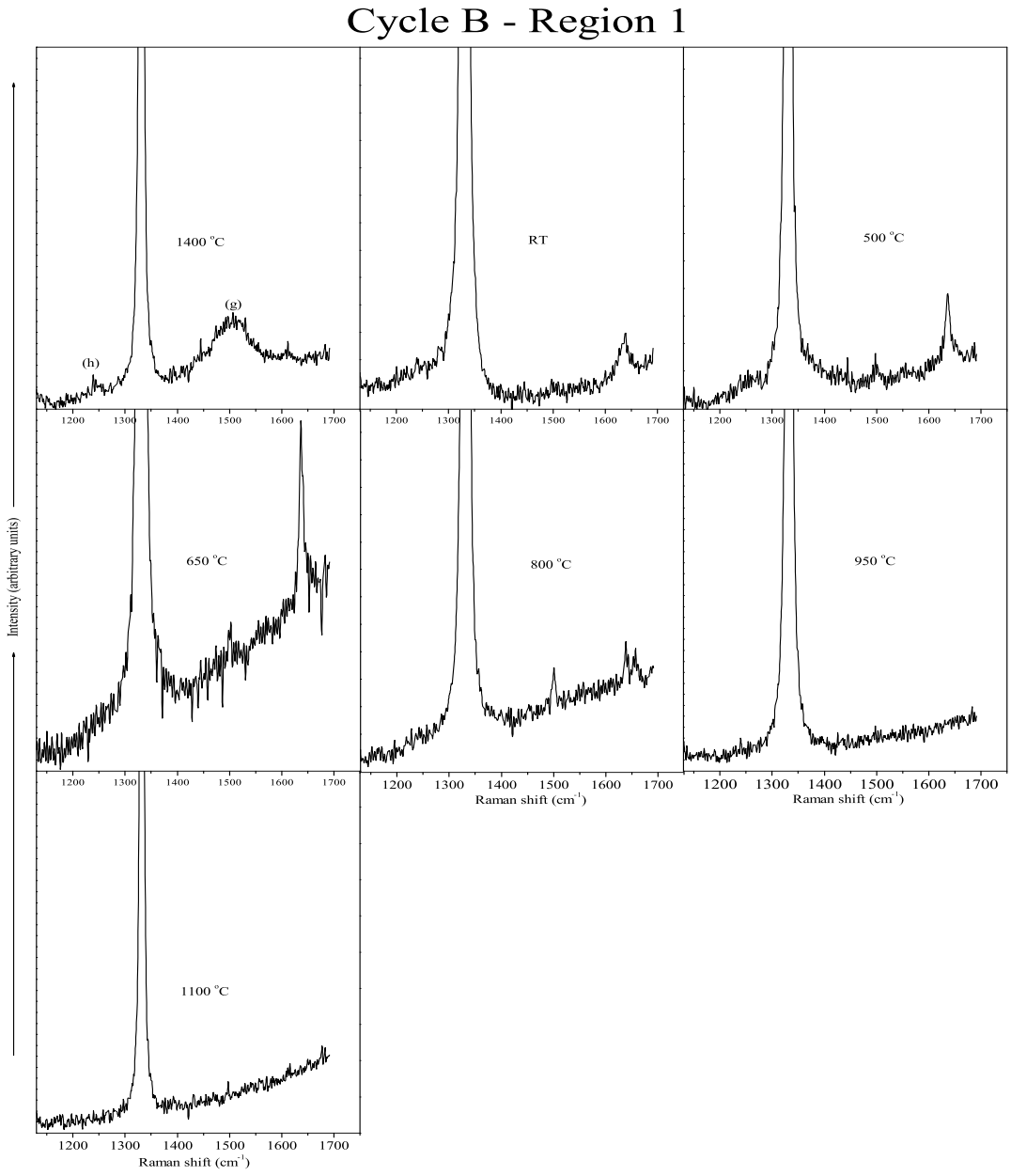


Figure 4.10: Raman spectra obtained for the implanted diamond in cycle B - region 1. The implanted dose is less than D_c. The 1638 cm^{-1} peak is present after annealing at RT while the 1498 cm^{-1} peak is present after annealing at 500 °C. No Raman active defect peaks are clearly visible after annealing at 950 °C. The defect peaks labelled (g) and (h) after annealing at 1400 °C are most probably due to contamination from the annealing crucible which was made of graphite. They also appear in the virgin spectra after annealing. (see fig 4.15 cycle C region 1 and 2 at labells (d), (e), (f) and (g)).

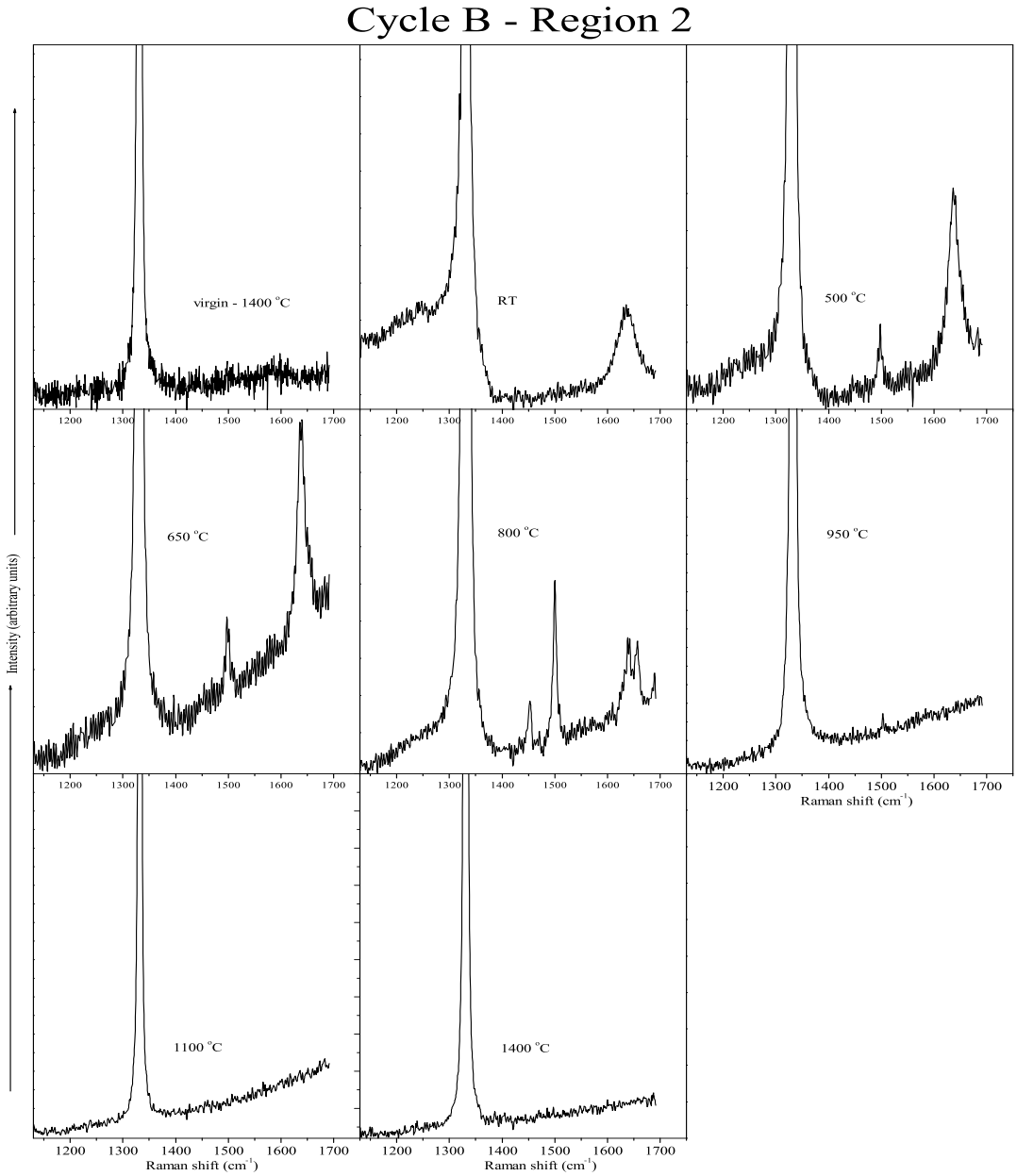


Figure 4.11: Raman spectra obtained for the implanted diamond in cycle B - region 2. The implanted dose is less than D_c. Evidence of the 1638 cm^{-1} peak is present after annealing at RT up to anneals at 800 °C and the 1498 cm^{-1} peak is present after annealing at 500 °C up to anneals at 950 °C. No Raman active defect peaks are clearly visible after annealing at 1100 °C.

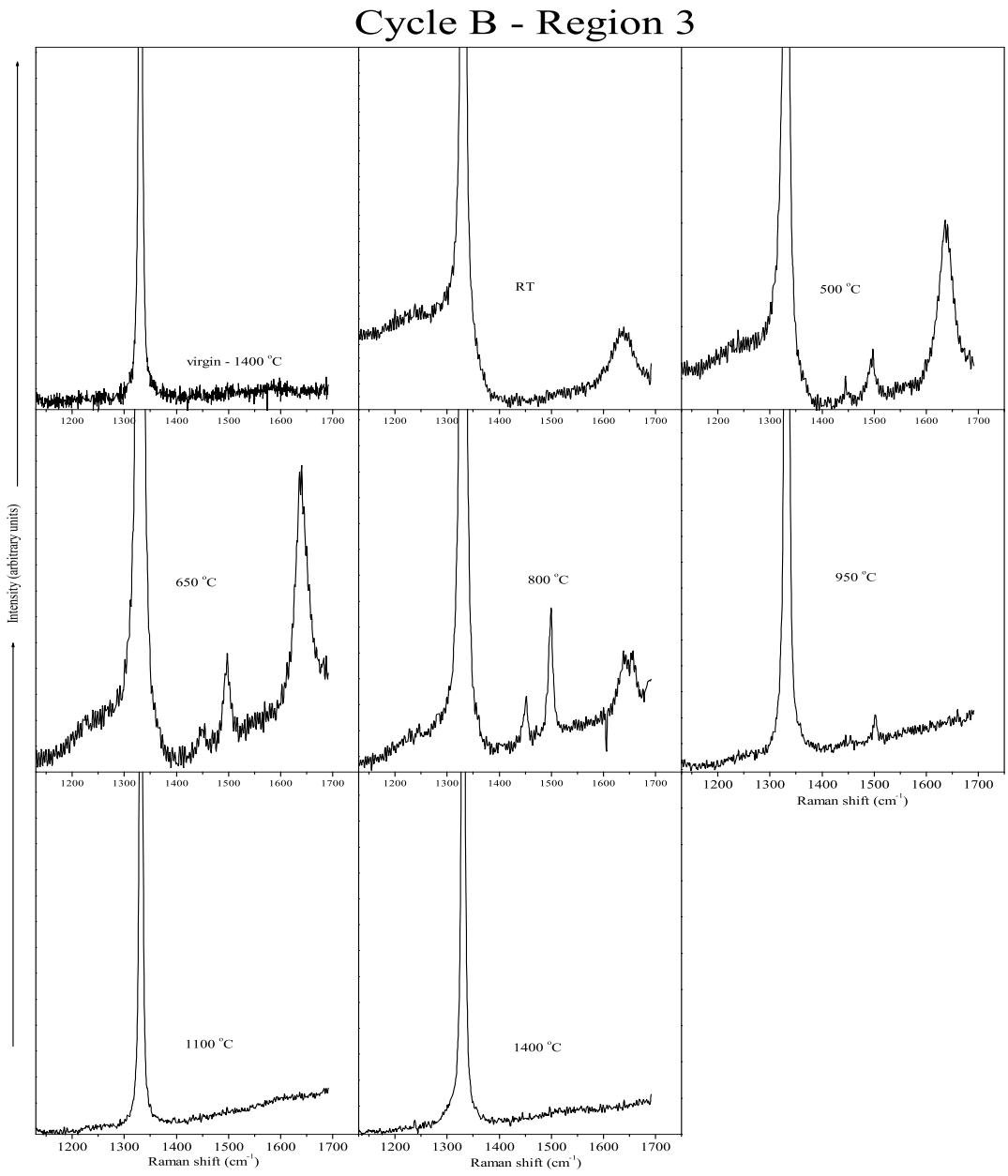


Figure 4.12: Raman spectra obtained for the implanted diamond in cycle B - region 3. The implanted dose is less than D_c. Evidence of the 1638 cm^{-1} peak is present after annealing at RT up to anneals at 800 °C and the 1498 cm^{-1} peak is present after annealing at 500 °C up to anneals at 950 °C. No Raman active defect peaks are clearly visible after annealing at 1100 °C.

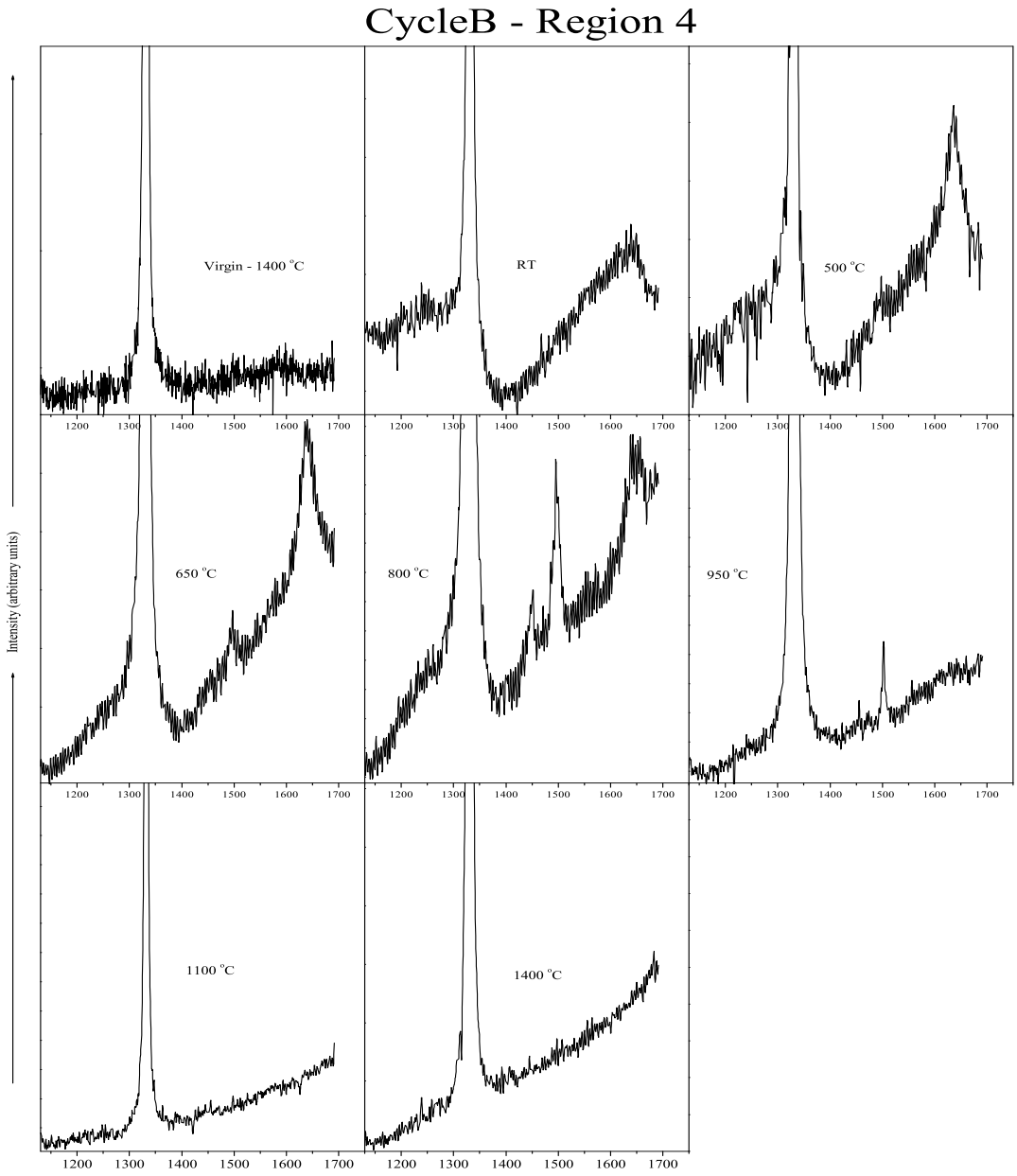


Figure 4.13: Raman spectra obtained for the implanted diamond in cycle B - region 4. The implanted dose is greater than D_c. Evidence of the 1638 cm^{-1} peak is present after annealing at RT up to anneals at 800 °C and the 1498 cm^{-1} peak is barely present after annealing at 500 °C but clearer after annealing at 650 °C up to anneals at 950 °C. No Raman active defect peaks are clearly visible after annealing at 1100 °C.

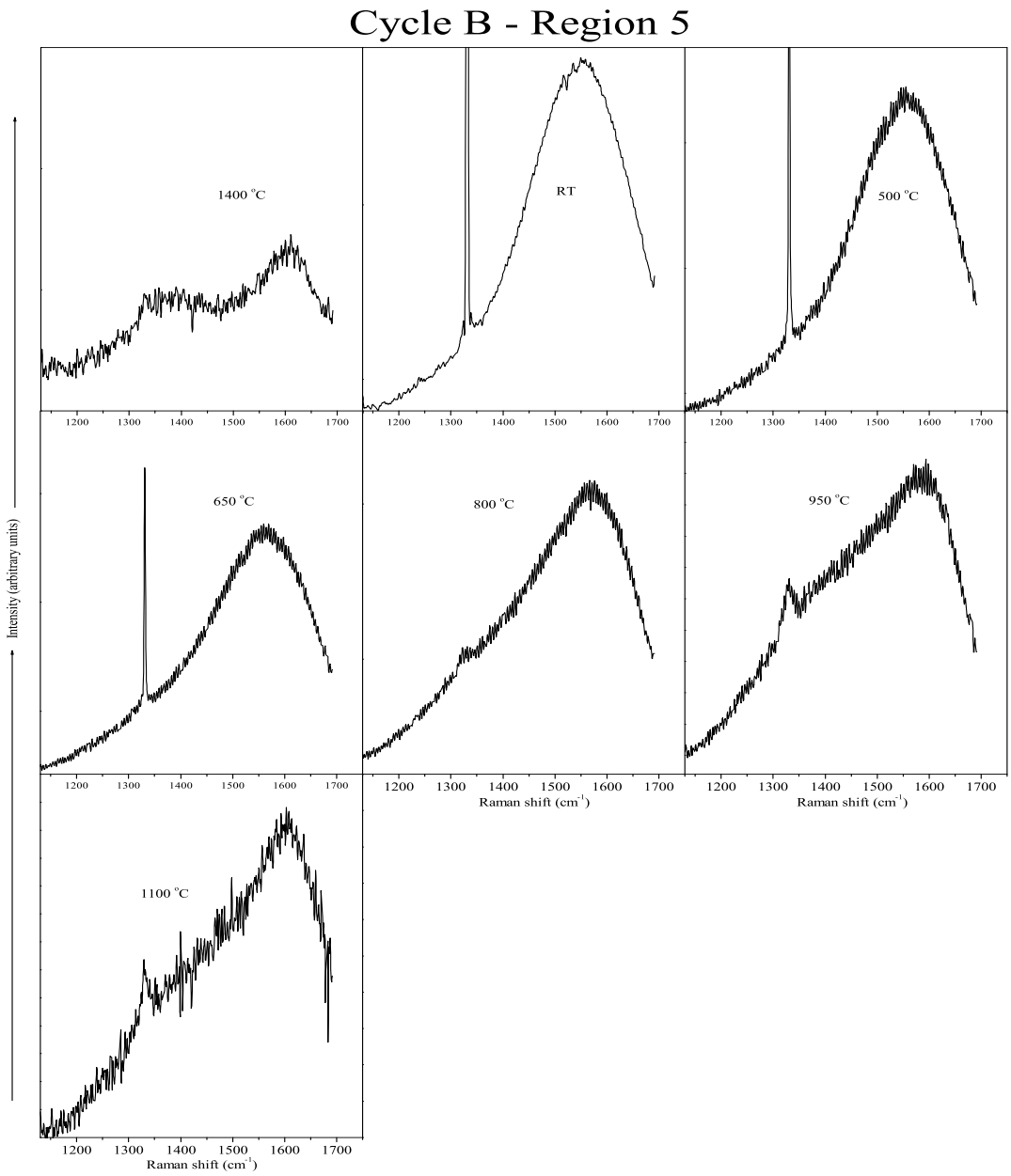


Figure 4.14: Raman spectra obtained for the implanted diamond in cycle B - region 5. The implanted dose is greater than D_c. No evidence of the 1638 cm^{-1} peak and the 1498 cm^{-1} peak is present after annealing at 500 °C. The spectra are dominated by a broad band centred around 1550-1580 cm^{-1} which indicates that the implanted - annealed layer consists of disordered graphite. The diamond line is barely visible after annealing at 800 °C.

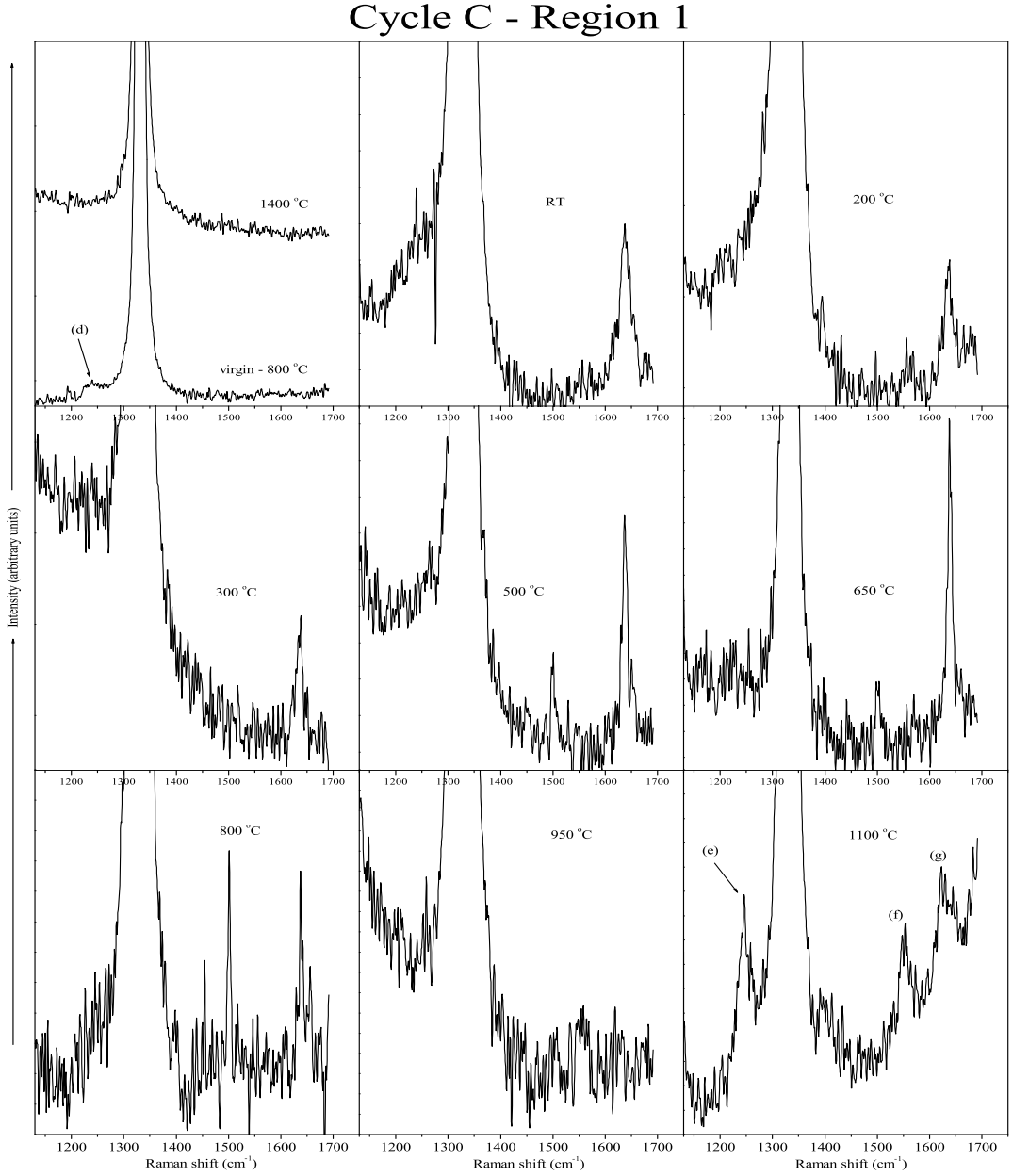


Figure 4.15: Raman spectra obtained for the implanted diamond in cycle C - region 1. The implanted dose is less than D_c. The 1638 cm^{-1} peak is present after the RT implant and anneals up to 800 °C. The 1498 cm^{-1} peak is present after annealing at 500 °C up to anneals to 950 °C. The defect peaks labelled (d), (e), (f) and (g) are assigned to contamination from the annealing crucible. Note the defect labelled (d) was measured from the unimplanted diamond (virgin-800 °C) after annealing at 800 °C.

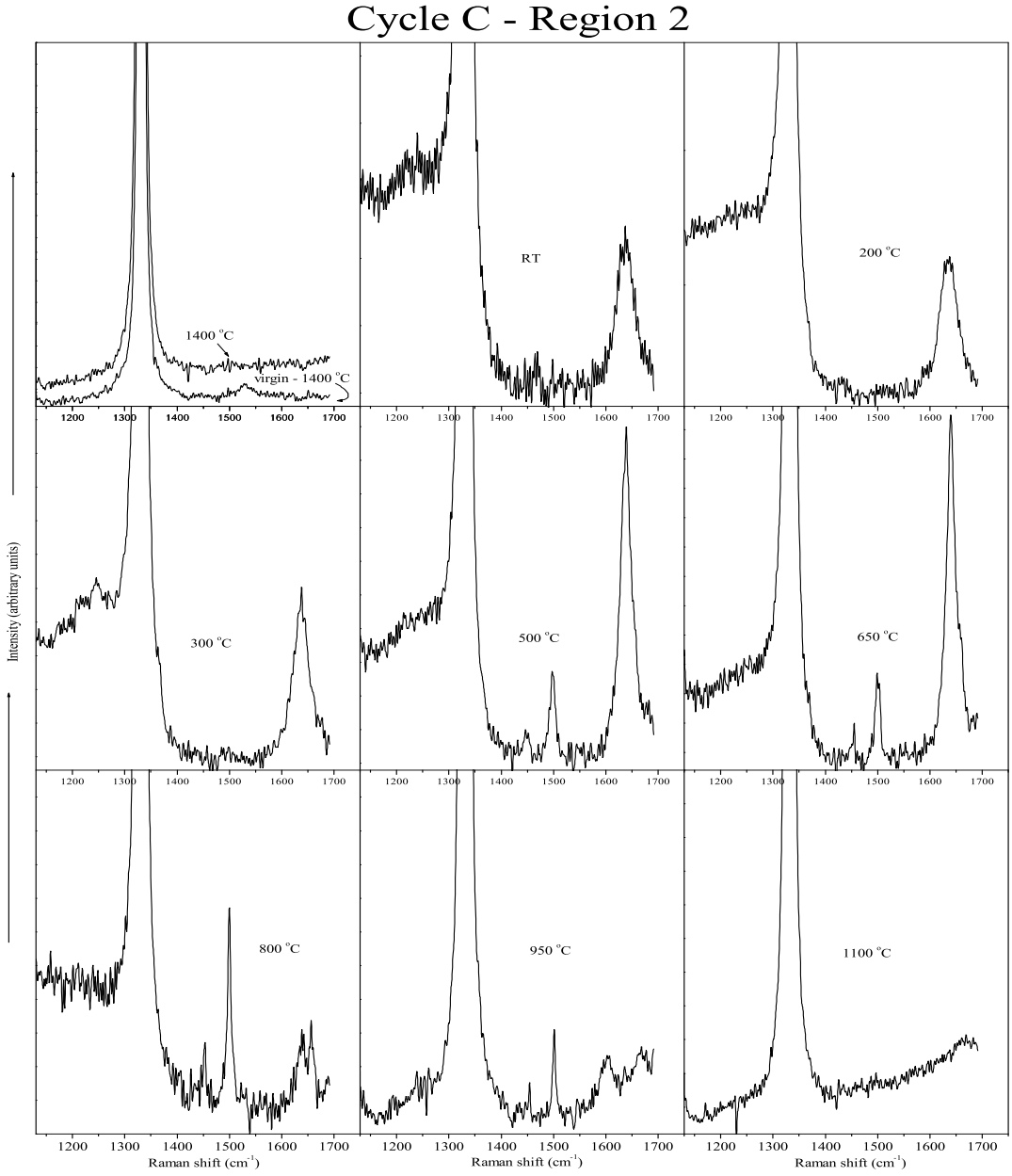


Figure 4.16: Raman spectra obtained for the implanted diamond in cycle C - region 2. The implanted dose is less than D_c. The 1638 cm^{-1} peak is present after the RT implant and anneals up to 800 °C. The 1498 cm^{-1} peak is present after annealing at 500 °C up to anneals to 950 °C. The defect peaks at 1620 cm^{-1} and 1680 cm^{-1} after the 950 °C are assigned to contamination from the annealing crucible. The same conclusion is made for the Raman shift measured at 1530 cm^{-1} in the virgin spectrum after annealing at 1400 °C.

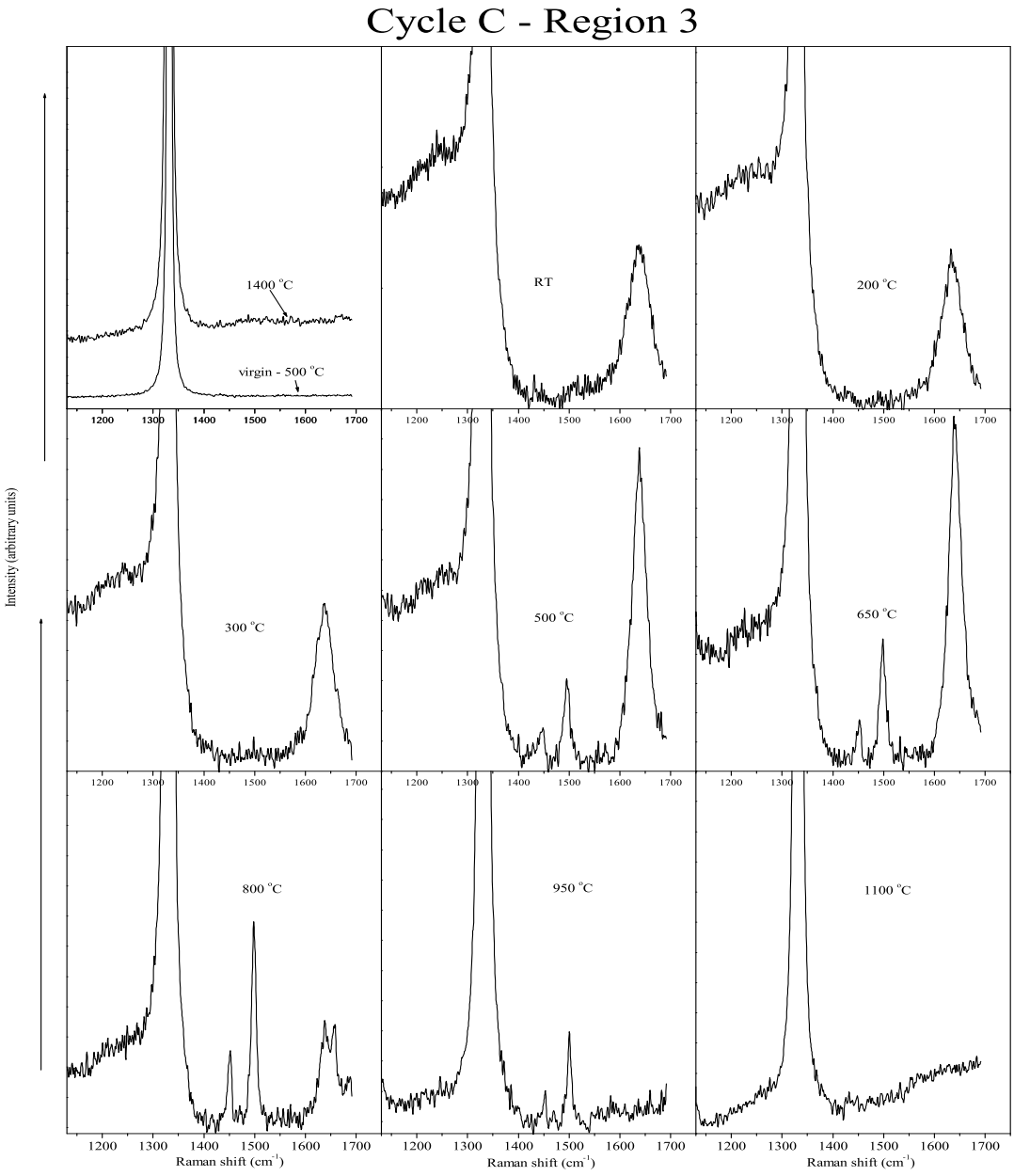


Figure 4.17: Raman spectra obtained for the implanted diamond in cycle C - region 3. The implanted dose is less than D_c. The 1638 cm^{-1} peak is present after the RT implant and anneals up to 800 °C. The 1498 cm^{-1} peak is present after annealing at 500 °C up to anneals to 950 °C.

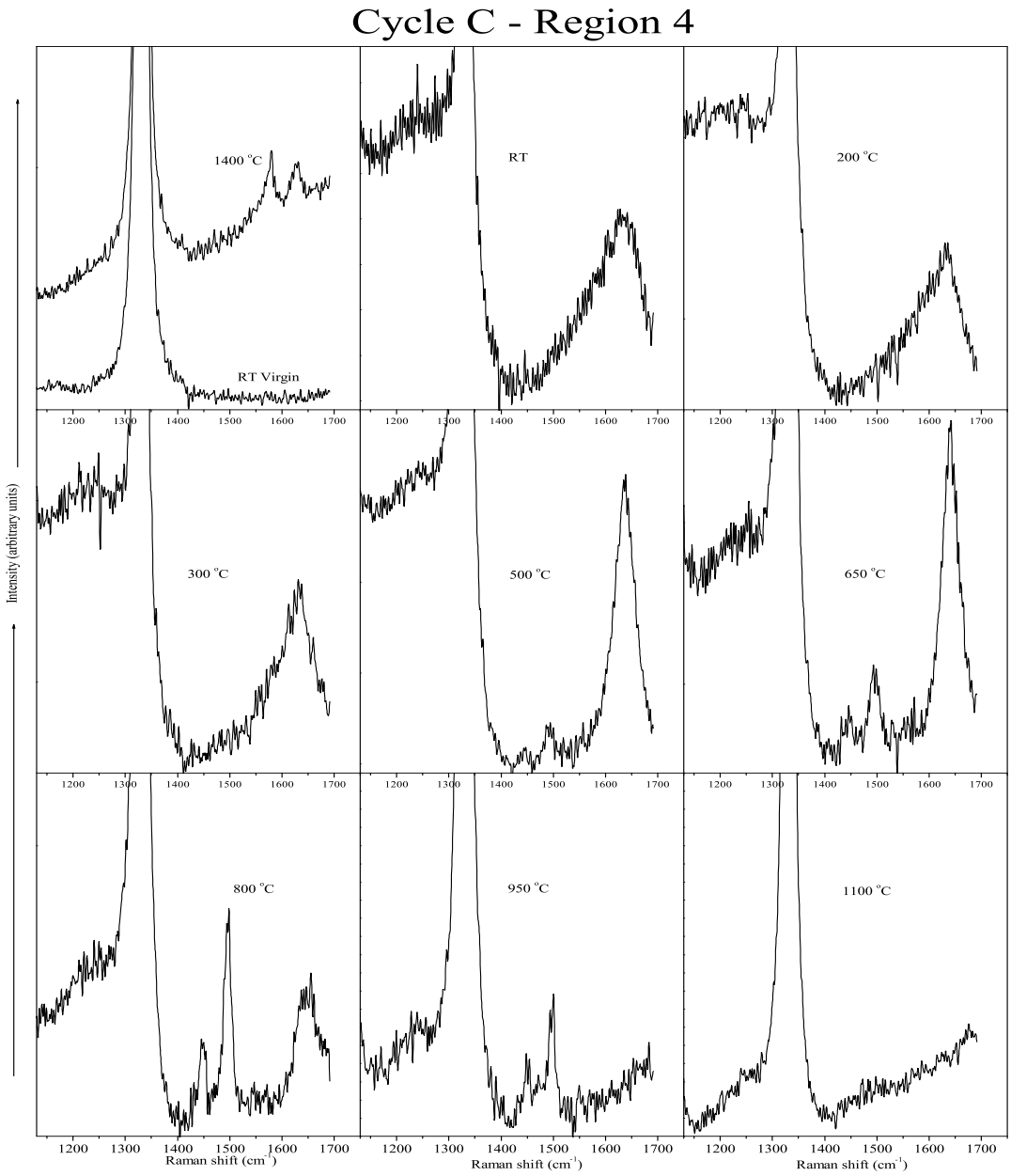


Figure 4.18: Raman spectra obtained for the implanted diamond in cycle C - region 4. The implanted dose is greater than D_c. The 1638 cm^{-1} peak is present after the RT implant and anneals up to 800 °C. The 1498 cm^{-1} peak is present after annealing at 500 °C up to anneals to 950 °C. The defect peaks at 1580 cm^{-1} and 1620 cm^{-1} after the 1400 °C anneal are assigned to contamination from the annealing crucible.

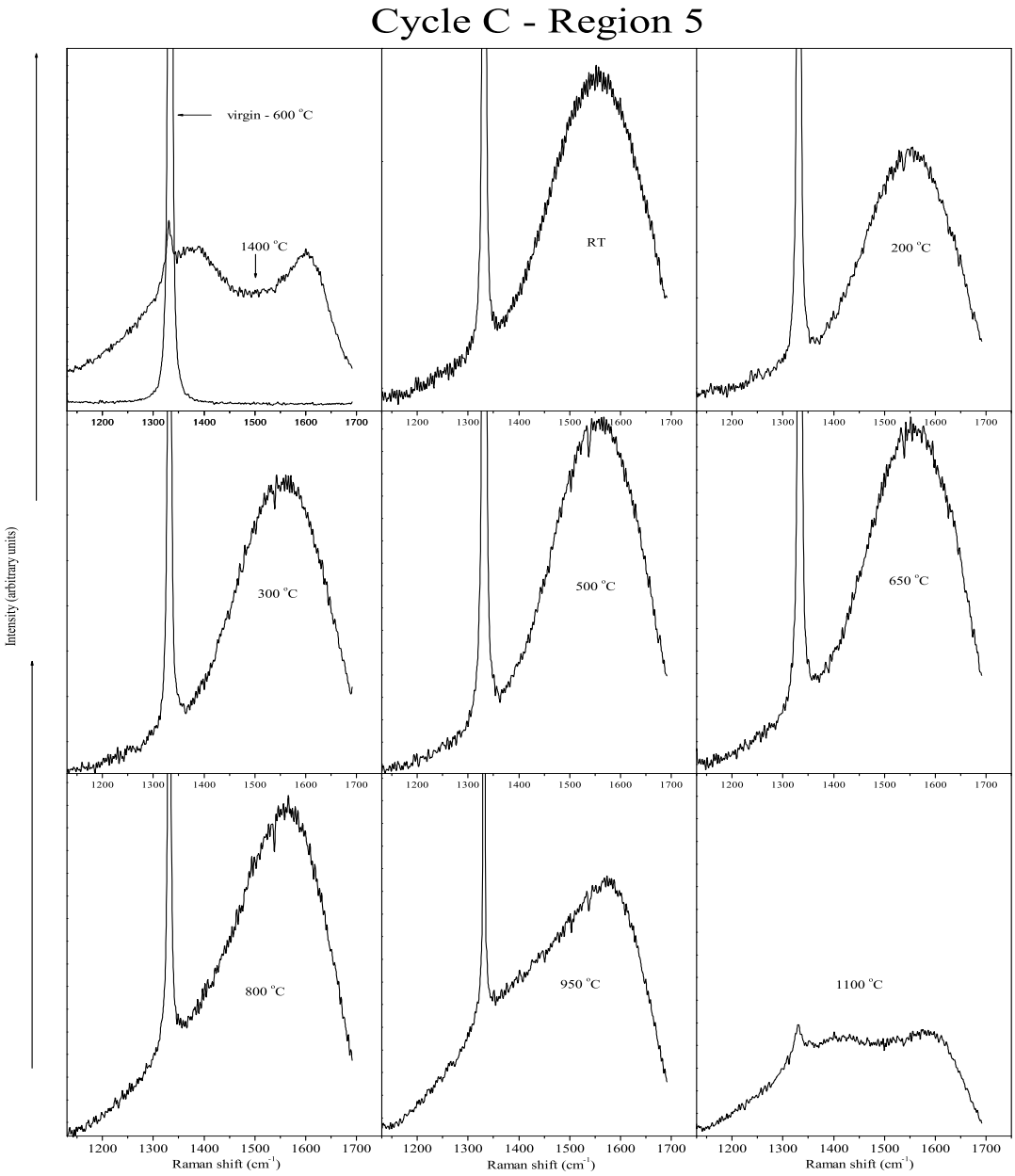


Figure 4.19: Raman spectra obtained for the implanted diamond in cycle C - region 5. The implanted dose is greater than D_c. No evidence of the 1638 cm^{-1} peak and the 1498 cm^{-1} peak is present after the RT implant. The spectra are dominated by a broad band centred around 1550-1580 cm^{-1} and 1360 cm^{-1} which indicates that the implanted - annealed layer consists primarily of disordered graphite.

The area in region 5, for cycles A, B, C and D was dark after ion implantation and it remained opaque after the subsequent high temperature anneals. For cycle D this visual onset of graphitization was observed also at region 4 and the subsequent high temperature annealing did not restore the region to any form of diamond. As described in the experimental setup, the Raman setup allowed us to probe a region of $\approx 2.5\,\mu$m (minimum) below the surface of the diamond. The Raman spectra thus showed scattered light from below the implantation region which in this case was about $0.23\,\mu$m. The diamond peak observed for regions 1 to 4 will therefore also include light scattered from the region below the surface where little or no damage took place as a result of the implantation-annealing process. As a result of this no analysis can be collated with respect to the intensity or peak position of the diamond line. For region 5, most of the light is absorbed within the opaque layer, and the spectra observed showed a weak or no diamond line. The vacancy density as predicted by TRIM for region 5 is well beyond the graphitization threshold for diamond. The graphitization threshold for diamond has been estimated to lie at $1 \times 10^{22}\,\mathrm{vac/cm^3}$ [105]. The Raman scattering data collected for region 5 indicated that this implanted region collapsed to a graphitic type structure and no subsequent annealing could restore the implanted layer back to any crystalline form. In Regions 1 to 4, for cycles A, B and C, the defect peaks that appear in the Raman scattering spectra are similar to those obtained for high energy (MeV) and low energy (keV) ion implantation [1, 13, 38, 106, 107, 152–155]. Based on the different conditions listed in [1, 13, 38, 106, 107, 152–155], it is clear that the appearance of these Raman shifts near 1450, 1498, $1638\,\mathrm{cm^{-1}}$ are not related to implantation energy or for that matter the mass of the implanted ion. As we will see it is dependent on the dose and the strain in the implanted layer which determines whether these Raman shifts will be observed. The annealing behaviour of the $1498\,\mathrm{cm^{-1}}$ and $1638\,\mathrm{cm^{-1}}$ peak at FWHM was monitored as a function of the implantation dose and annealing temperature [fig. 4.25 and fig. 4.26].

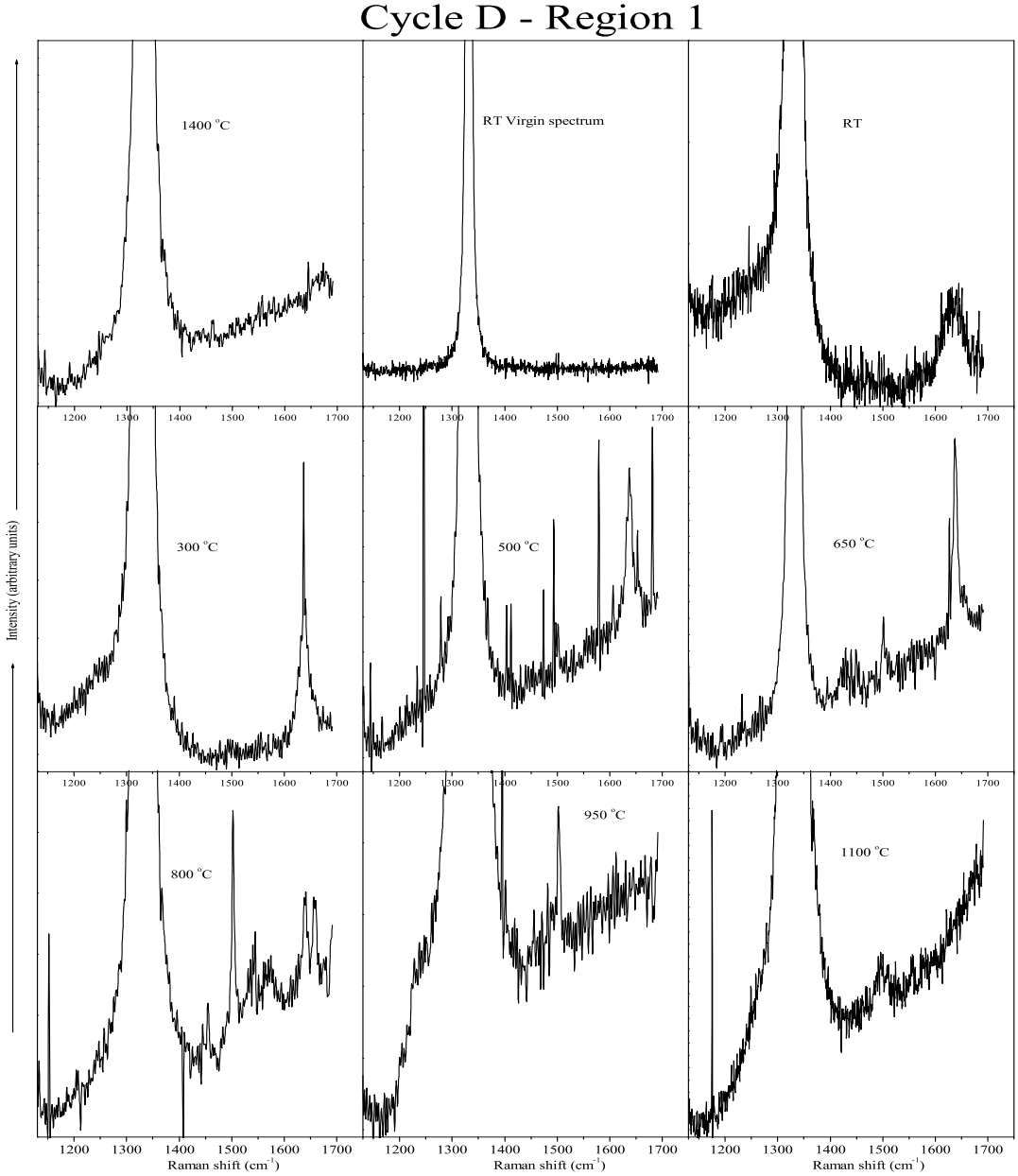


Figure 4.20: Raman spectra obtained for the implanted diamond in cycle D - region 1. The implanted dose is less than D_c. The 1638 cm^{-1} peak is present after the RT implant and anneals up to 800 °C. The 1498 cm^{-1} peak is present after annealing at 500 °C up to anneals to 950 °C. The broad defect band at 1480 cm^{-1} after the 1100 °C anneal is most probably due to contamination from the annealing crucible. The same can be said for the defect band at 1660 cm^{-1} after the 1400 °C anneal.

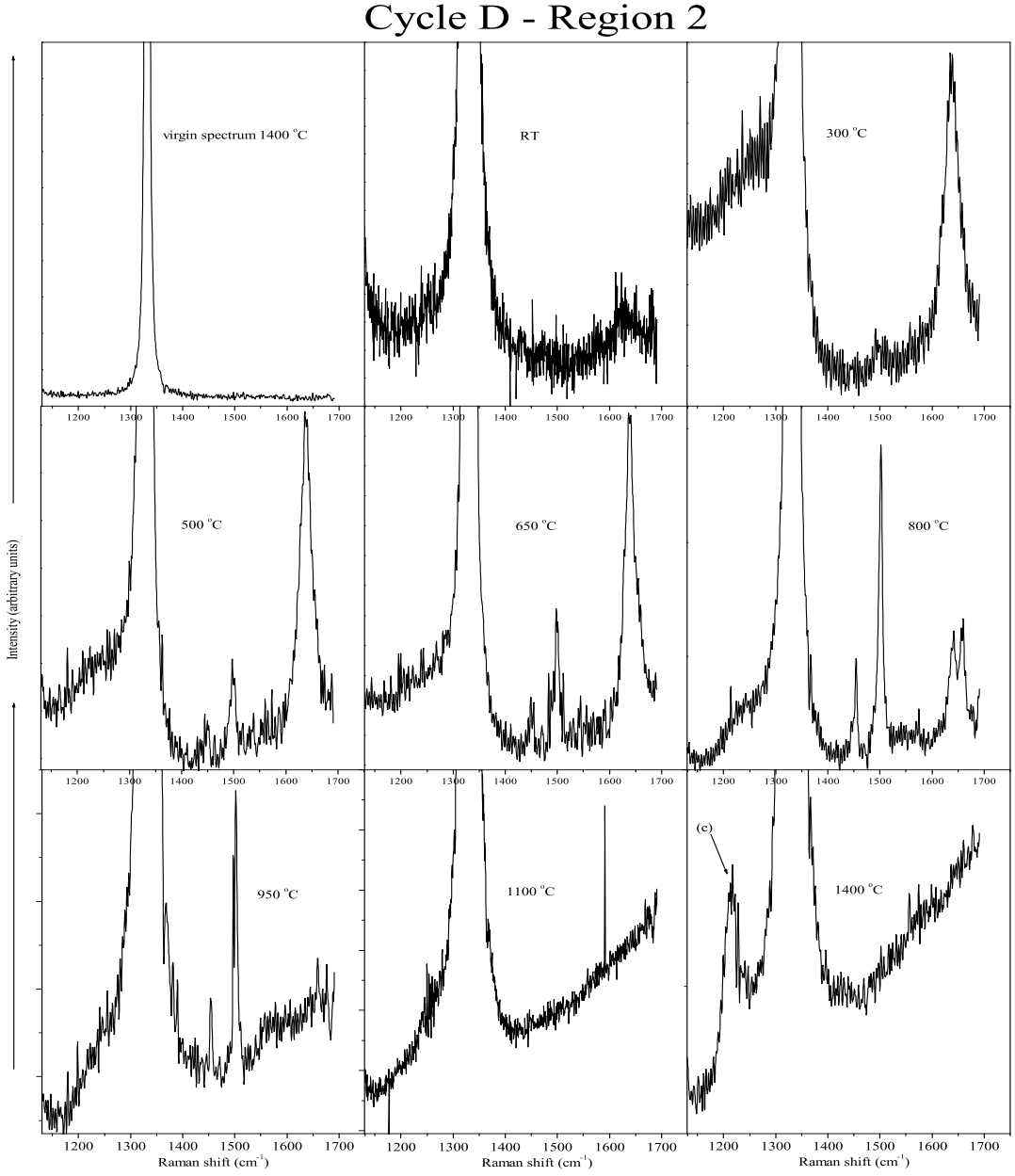


Figure 4.21: Raman spectra obtained for the implanted diamond in cycle D - region 2. The implanted dose is less than D_c. The 1638 cm^{-1} peak is present after the RT implant and anneals up to 800 °C. The 1498 cm^{-1} peak is present after annealing at 300 °C (not well defined) up to anneals to 950 °C. The sharp defect band labelled (c) at 1210 cm^{-1} after the 1400 °C anneal is tentatively assigned to contamination from the annealing crucible during the annealing stage at this high temperature.

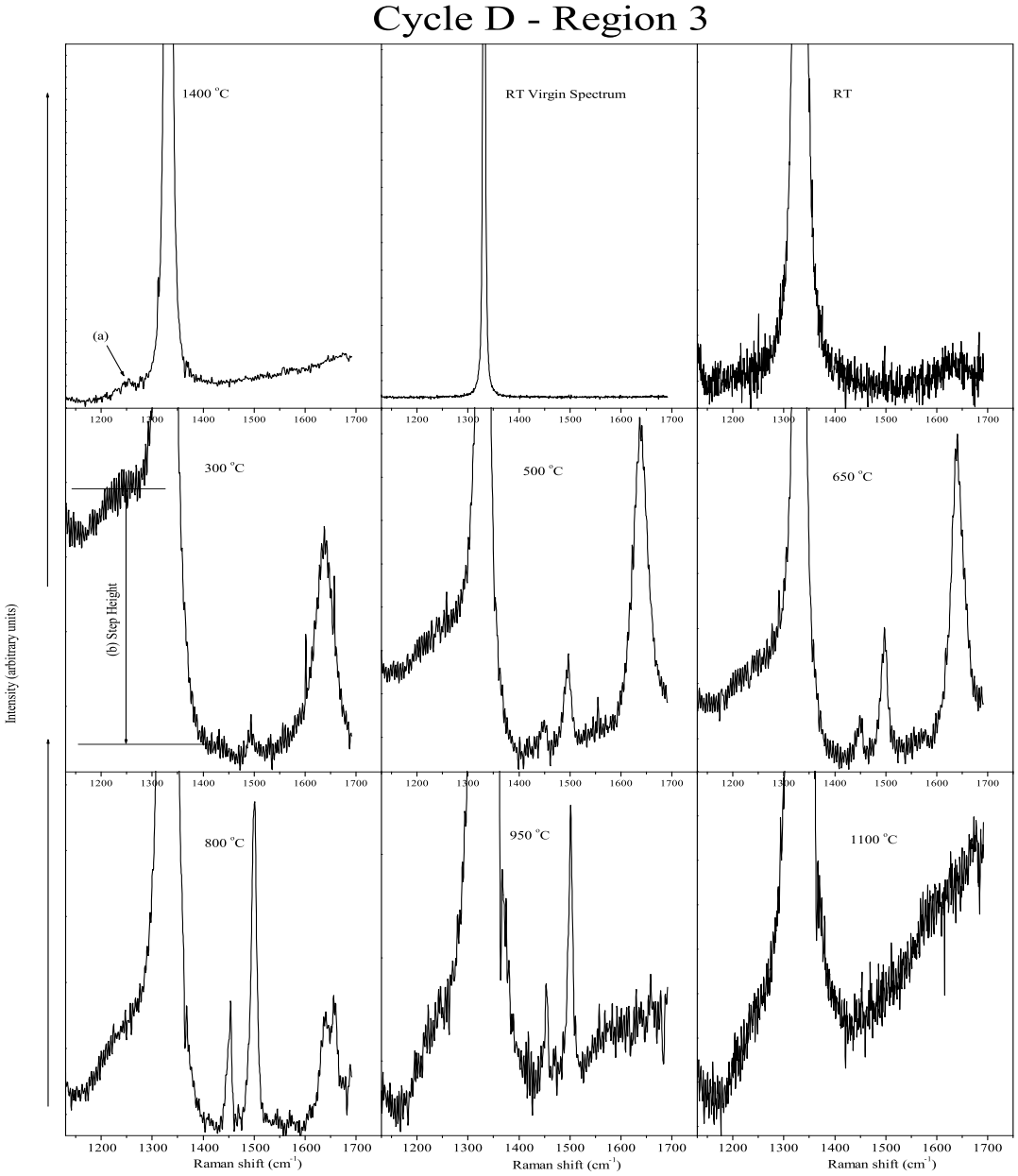


Figure 4.22: Raman spectra obtained for the implanted diamond in cycle D - region 3. The implanted dose is less than D_c. The 1638 cm^{-1} peak is present after the RT implant and anneals up to 800 °C. The 1498 cm^{-1} peak is present after annealing at 300 °C up to anneals to 950 °C. The defect band labelled (a) at 1250 cm^{-1} after the 1400 °C anneal is tentatively assigned to contamination from the annealing crucible. Similar defects appear in the virgin spectra after high temperature annealing as shown earlier in other spectra.

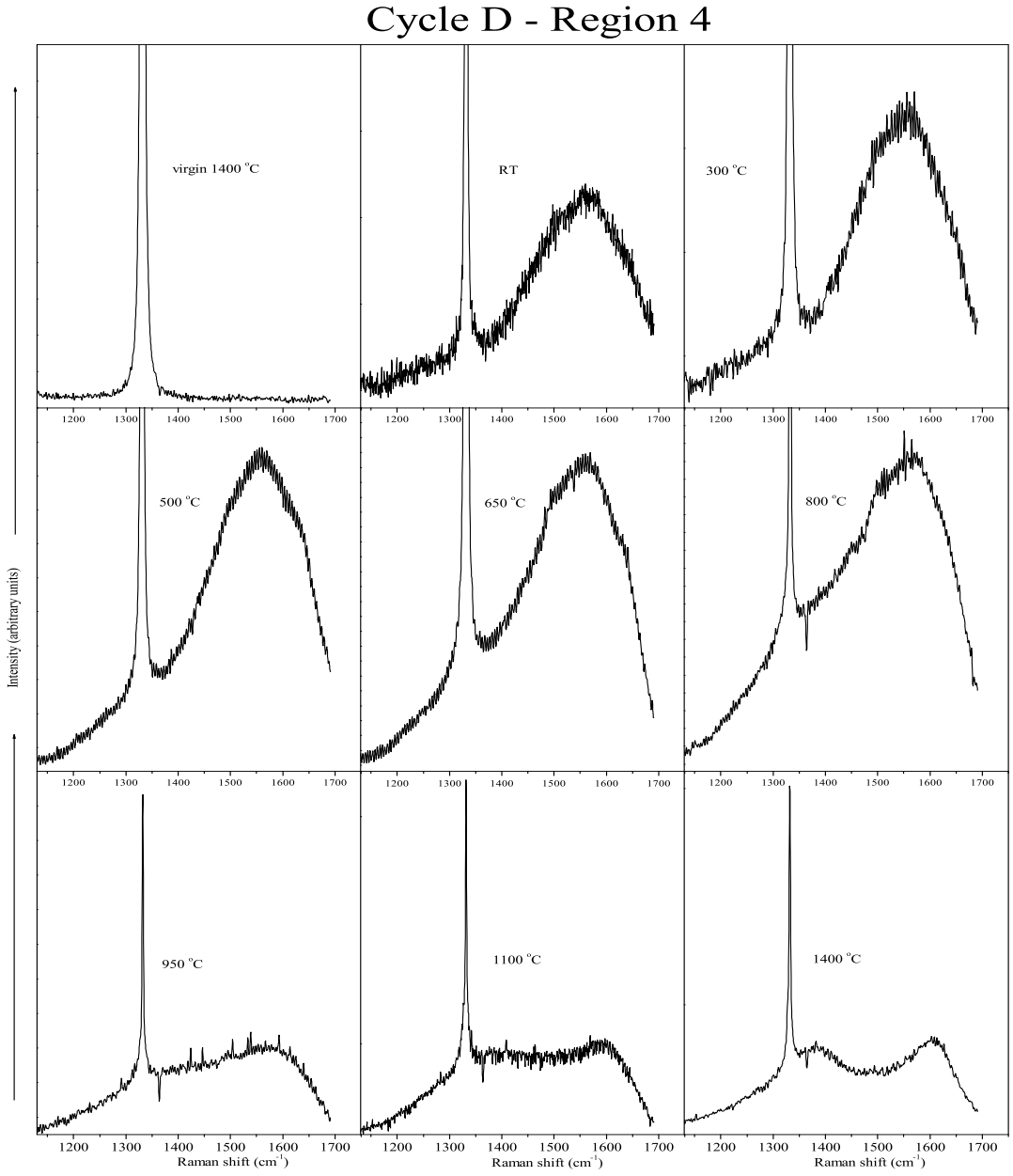


Figure 4.23: Raman spectra obtained for the implanted diamond in cycle D - region 4. The implanted dose is greater than D_c. No evidence of the 1638 cm^{-1} peak and the 1498 cm^{-1} peak is present after the RT implant. The spectra are dominated by broad bands centred around 1550-1580 cm^{-1} and 1360 cm^{-1} which indicates that the implanted - annealed layer consists primarily of disordered graphite. It is interesting to note that in these spectra there is strong evidence of the diamond peak in spite the presence of a broad disordered graphite band even after annealing at high temperatures. The diamond line in this case most probably arises from the unimplanted layer above the graphitic layer recalling that for cycle D the implanted dose was performed at a single energy.

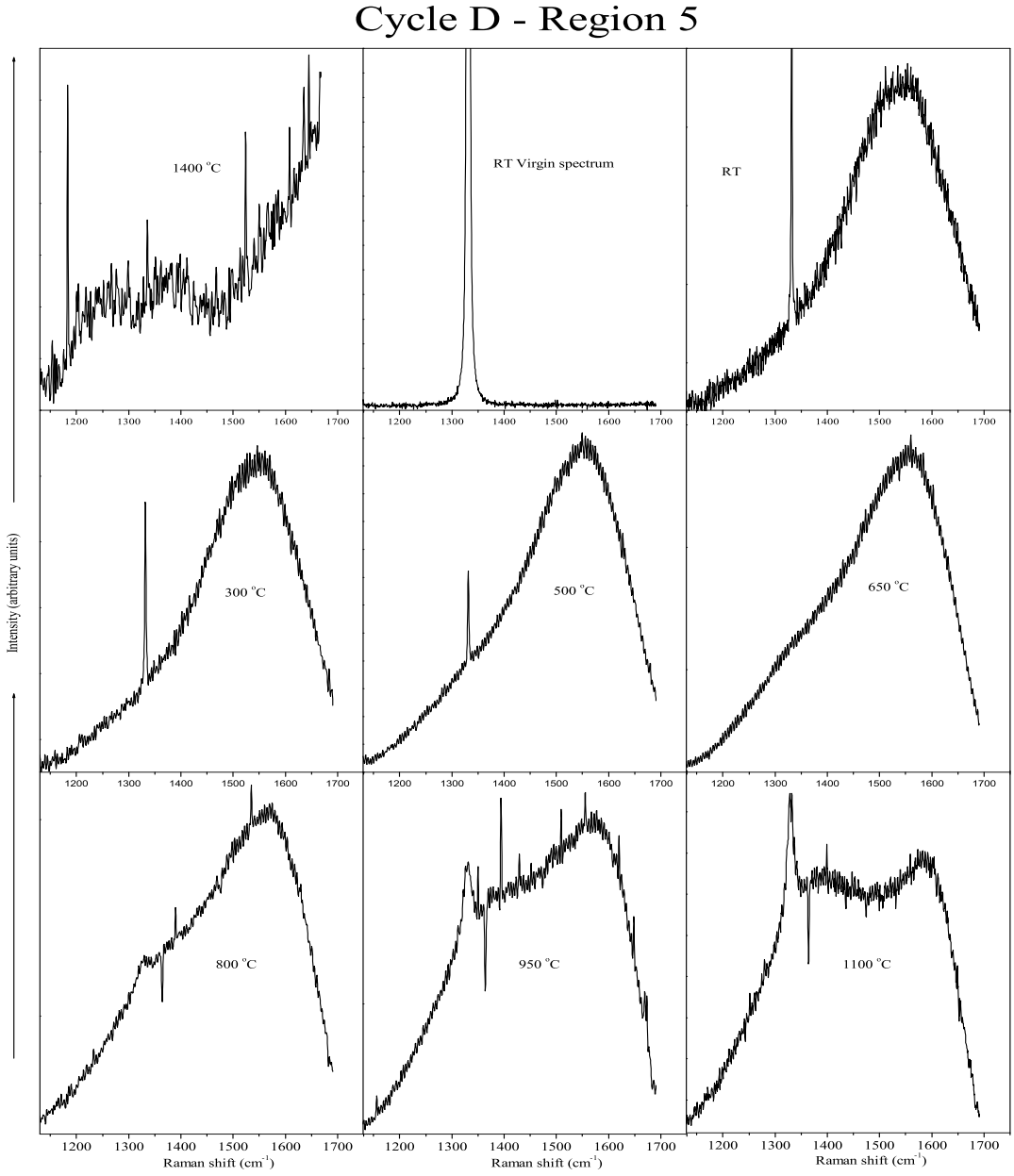


Figure 4.24: Raman spectra obtained for the implanted diamond in cycle D - region 5. The implanted dose is greater than D_c. No evidence of the 1638 cm^{-1} peak and the 1498 cm^{-1} peak is present after the RT implant. The spectra are dominated by a broad band centred around 1550-1580 cm^{-1} which indicates that the implanted - annealed layer consists primarily of disordered graphite.

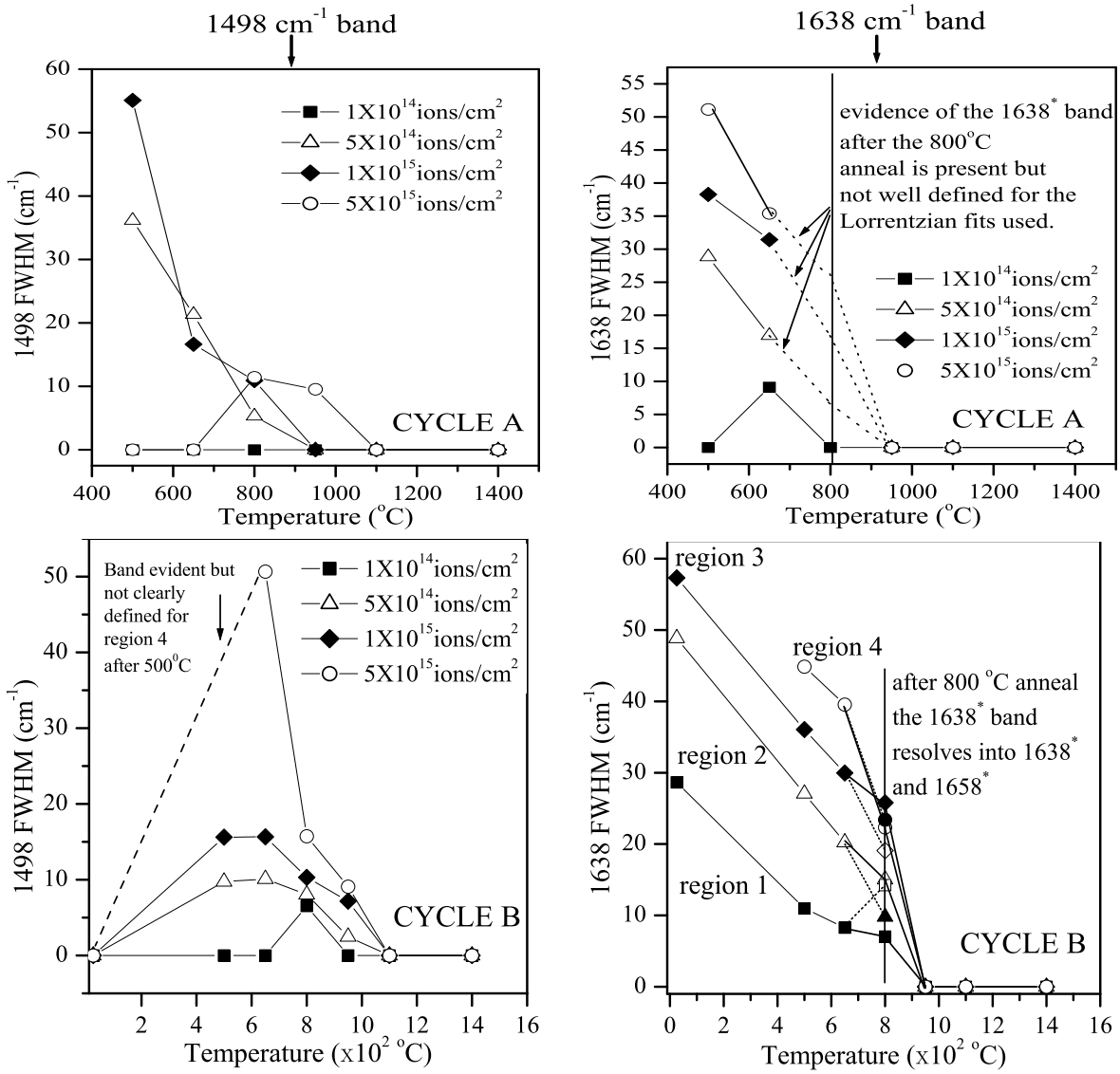


Figure 4.25: Annealing behaviour of the 1498 and 1638 cm^{-1} bands for cycle A and B. The Full Width at Half Maximum (FWHM) was obtained for the different peaks by fitting a Lorentzian function over the appropriate peaks in the Raman spectra.

4.4 Discussion

The assignment that the 1638 cm^{-1} defect peak is related to an interstitial type defect, is made since the migration or diffusion of interstitials in diamond occur at lower temperatures. This has also been argued for the case of MeV implanted layers [13]. In all of the implantation-annealing sequences employed, this band is present during the low temperature anneals and only completely anneals away after the 950 °C anneal.

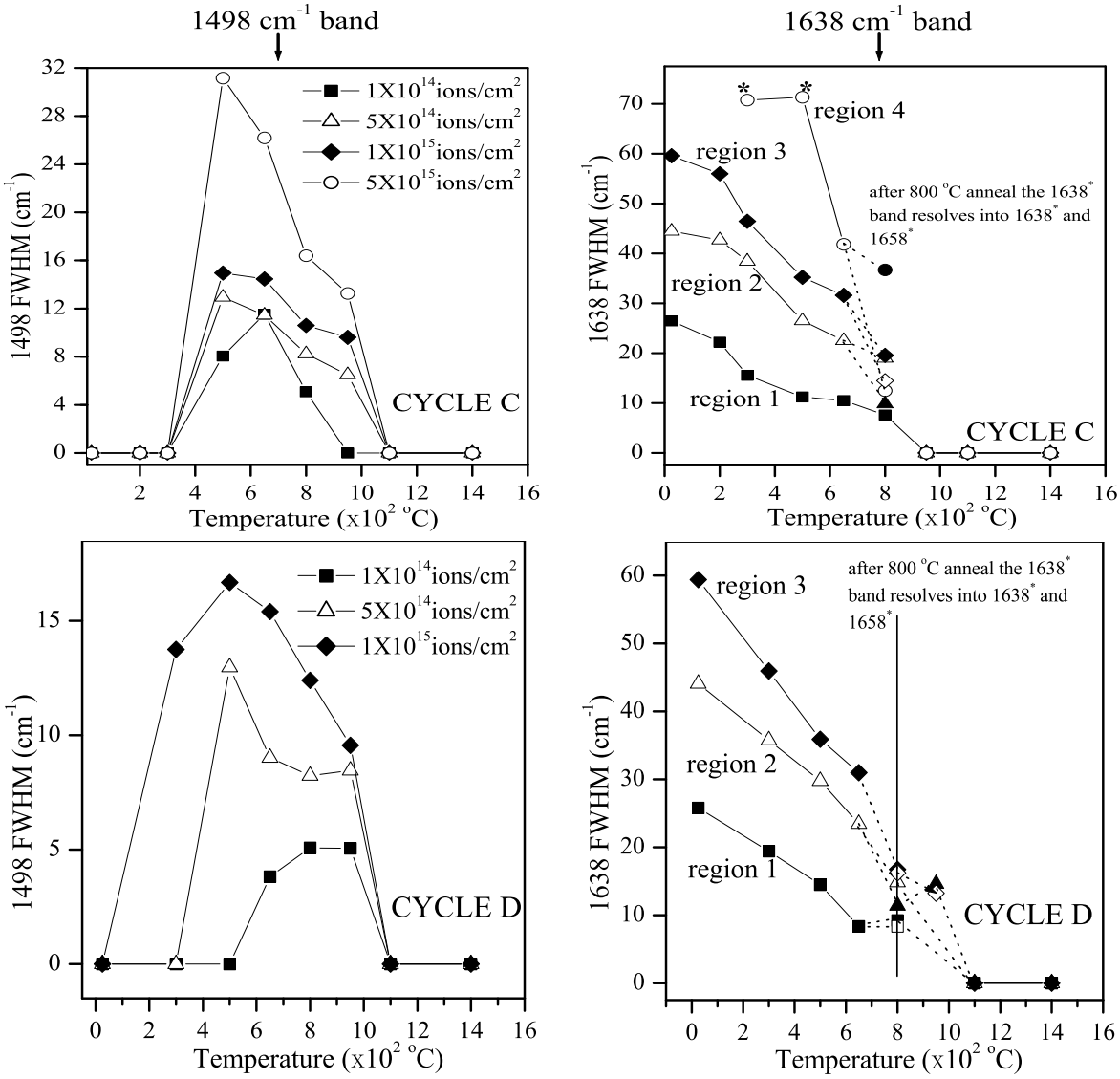


Figure 4.26: Annealing behaviour of the 1498 and 1638 cm^{-1} bands for cycle C and D. The Full Width at Half Maximum (FWHM) was obtained for the different peaks by fitting a Lorentzian function over the appropriate peaks in the Raman spectra. The data points labelled with * in cycle C for the 1638 cm^{-1} are those where the band was initially not centred around 1638 cm^{-1}, but appeared as a broad band centred around 1630 cm^{-1}. Note that cycle D had no additional features in regions 4 and 5 at any of the annealing temperatures, but rather broad bands centred around 1580 cm^{-1} and 1360 cm^{-1}.

The 1638 cm^{-1} has been associated with the split <100> interstitial in diamond [13]. Theoretical calculations predict that the split <100> interstitial type defect is stable in diamond [114] and channelling measurements made by Spits *et al* [118] confirm that the split interstitial is the most probable interstitial type defect that forms in ion implanted

and annealed diamond. An interesting observation is noted for the 1638 cm^{-1} peak. The band is initially observed as a single band after annealing at 500 °C, but after annealing at 800 °C there is another defect peak that appears at ≈1658 cm^{-1} with the 1638 cm^{-1} [fig. 4.27]. The appearance of the 1658 cm^{-1} defect peak is more apparent in the implantation-annealing cycles B, C and prominent in regions 1 to 3 for cycle D. The formation of the 1658 cm^{-1} Raman active mode is clearly present with the 1638 cm^{-1} Raman peak. Although this distinction is only more clearly observed after annealing at 800 °C , it appears likely that the broadness of the 1638 cm^{-1} Raman peak prior to the 800 °C anneal is a result of both strain in the implanted layer and the prescence of the 1658 cm^{-1} peak. Because the 1658 cm^{-1} Raman peak apears and anneals away with the 1638 cm^{-1} Raman peak it is highly probable that the Raman shift measured at 1658 cm^{-1} is due to Raman active vibrational modes of carbon atoms at or near interstitial sites. The most favourable defect for the 1658 cm^{-1} Raman peak could be a form of the di-interstitial defect in diamond which are shown to form from the split <100> interstitials [116].

The 1498 cm^{-1} and 1450 cm^{-1} defect peaks become clearly defined after annealing at 500 °C. The vacancy in diamond is reported to be mobile above 500 °C. It thus appears that the defects related to these Raman peaks are related to vacancies. This band is not observed after annealing above 1000 °C in any of the regions 1 to 4. Since the GR1 band associated with neutral single vacancies anneals away at 600 °C the 1498 cm^{-1} and 1450 cm^{-1} peaks is more likely related to the TH5 defect (divacancy) [115] or multivacancy complexes that are reported to form along the <110> axes [120].

It was initially thought that the 1450, 1498 and 1638 cm^{-1} bands were unique to high energy implantation [153, 155, 156]. The implanted layer was argued to be confined by a pressure cap as a result of the lightly damaged diamond above the implanted layer. It has been suggested that it is this pressure cap that allows one to implant doses in excess of the graphitization threshold, and subsequent annealing will recover the implanted layer to the original diamond structure [13, 153, 155, 156]. Most of the comparisons

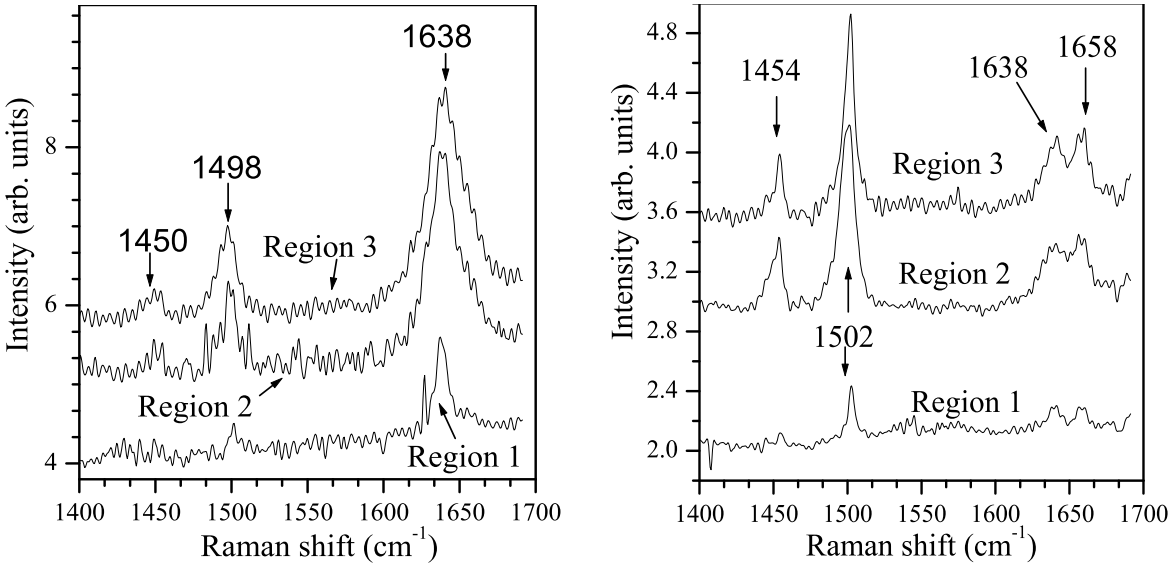


Figure 4.27: Raman spectra collected during cycle D after annealing at 650 °C (left figure) for 1 hour and thereafter at 800 °C (right figure) for 1 hour. The 1638 cm^{-1} and the 1658 cm^{-1} peaks are clearly visible as well as the defect band centred around 1450 cm^{-1}. Note also the shift to higher wavenumbers for the 1450 and 1498 cm^{-1} defect bands afer the 800 °C anneal.

to MeV implanted diamond made in relation to this work is with respect to the data presented by Orwa *et al* in [13]. In their paper (Orwa) high energy (3.5 MeV) He-ion irradiation to a dose of 1×10^{17} ions/cm^2 was used to create the damaged layer in a natural type IIa diamond. The projected range where the implanted He ions will stop in the diamond lattice for this energy is close to 5.88 μm according to TRIM. In this study we observed that the implanted layer at keV energies (max depth 0.23 μm for cycle A,B and C and 0.15 μm for cycle D as shown earlier) did not relax to graphite even when the critical dose was exceeded. Regions 4 and 5 were all implanted with doses which created an average vacancy density above 1×10^{22} vac/cm^3 (see fig. 4.2), but relaxation to graphite was only observed for region 5 for the implantation-annealing cycles A, B and C and in regions 4 and 5 for cycle D. The same observation has been reported in [157].

Because the implanted layer is relatively close to the surface in keV implanted layers it is difficult to make an assessment of the behaviour of the first order diamond Raman line as a function of dose and annealing temperature within the implanted layer

nor can we asses the intensity as a function of depth for any of the Raman damage peaks. In MeV implanted layers, it is easier to monitor the changes in the first order diamond line by using a cross-sectional configuration [13, 154] and compare this with the intensity of the Raman damage peaks for that particular depth. In most cases found in literature, a downward shift and broadening of the first order diamond Raman line is associated with tensile stress [3, 124, 125]. In terms of the phonon confinement model, this downward shift and broadening is accompanied by a skewing of the first order diamond Raman line [124]. Prawer [107] argues that when a downshift and broadening of the diamond Raman line is not accompanied by any skewing of the line, then the shift and broadening of the $1332\,\mathrm{cm}^{-1}$ line is due to the presence of defects *without* any residual stress in the implanted layer. It is important to note that the symmetry and broadening of the diamond Raman line noted by Prawer is enhanced when the 'diamond allowed' and 'diamond forbidden' spectra are subtracted from each other [13]. We argue that the implanted layers in this study at keV energies are in *tensile* stress by monitoring the behaviour of the Raman shifts observed at 1498 and $1638\,\mathrm{cm}^{-1}$. The peak position of the $1498\,\mathrm{cm}^{-1}$ vs annealing temperature and TRIM damage is shown in figures [4.28] and [4.29] respectively. For annealing cycles B, C, D the peak position was lower at higher doses and increased in wavenumber as the annealing temperature was raised. Also note the decrease in the FWHM for both the 1498 and $1638\,\mathrm{cm}^{-1}$ Raman shifts with increasing annealing temperature [fig 4.25 and 4.26]. This suggests that the implanted layer under keV irradiation is under tensile stress since the defect peaks are broadened by strain within the implanted later which then become more defined as the strain is relaxed by higher temperature anneals. Hence one can argue that it is the defects created by the implantation process that induces the strain in the implanted layer and causes the downward shift and symmetric broadening of the first order diamond Raman line [125] as observed in MeV implanted diamond [13]. The peak FWHM $1498\,\mathrm{cm}^{-1}$ versus peak position $1498\,\mathrm{cm}^{-1}$ [fig. 4.30] peak follows a similar trend as observed for MeV implanted diamond [13].

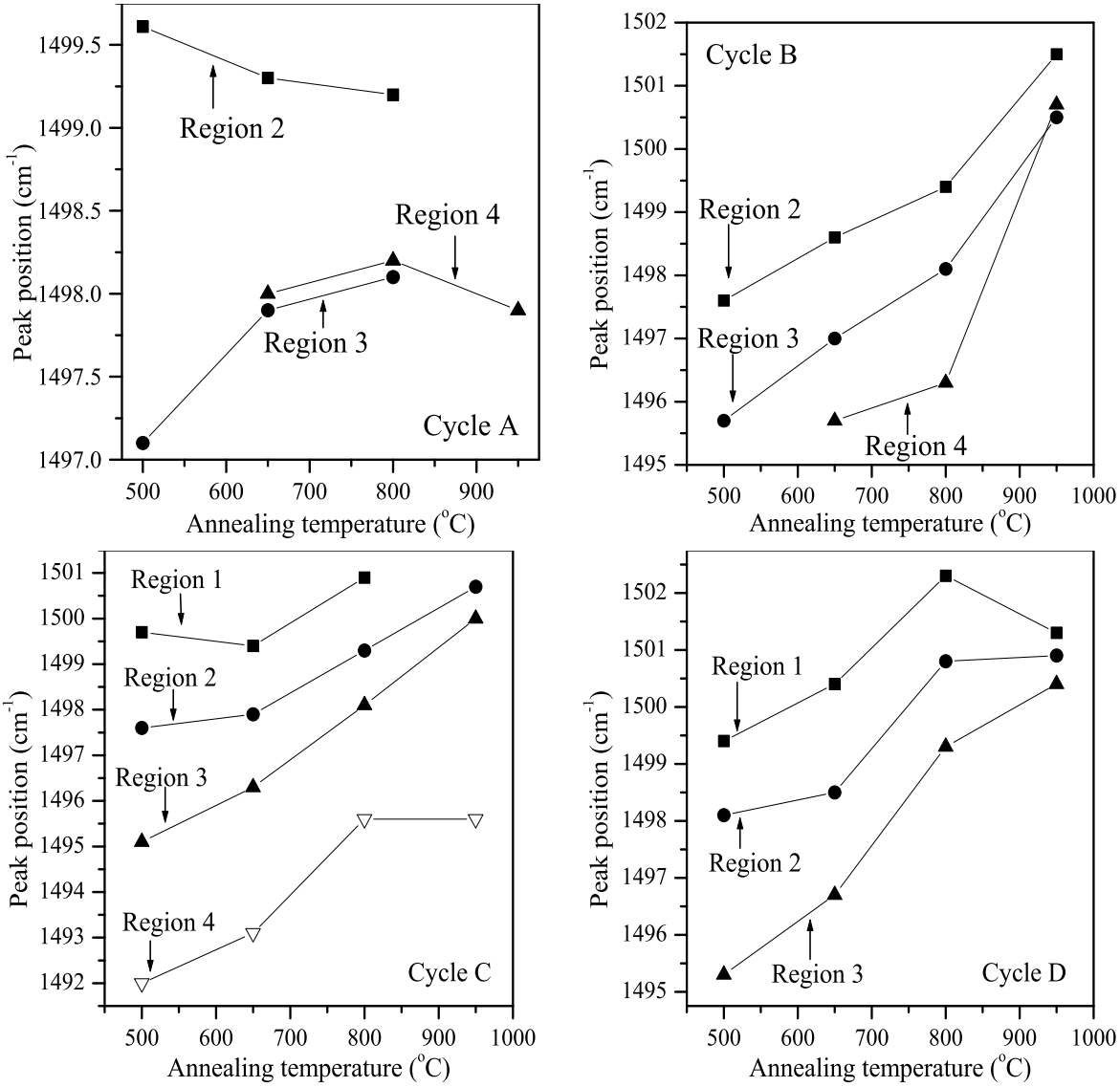


Figure 4.28: 1498 cm^{-1} peak position versus annealing temperature. The behaviour for cycle A indicates that the tensile stress in is substantially less after a CIRA process with the dose implanted over a wide width.

In MeV implanted diamond the 1638 cm^{-1} peak FWHM versus 1638 cm^{-1} peak position shows a similar trend as in fig 4.30 for the 1498 cm^{-1} Raman line. This is not observed in keV implanted diamond for the 1638 cm^{-1} Raman shift. This behaviour is related to this shift being composed of two peaks that initially appear as a single broad band. This could be attributed to the fact that the induced stress due to the implantation is contained in a narrow width for keV implanted diamond. At the lower temperature

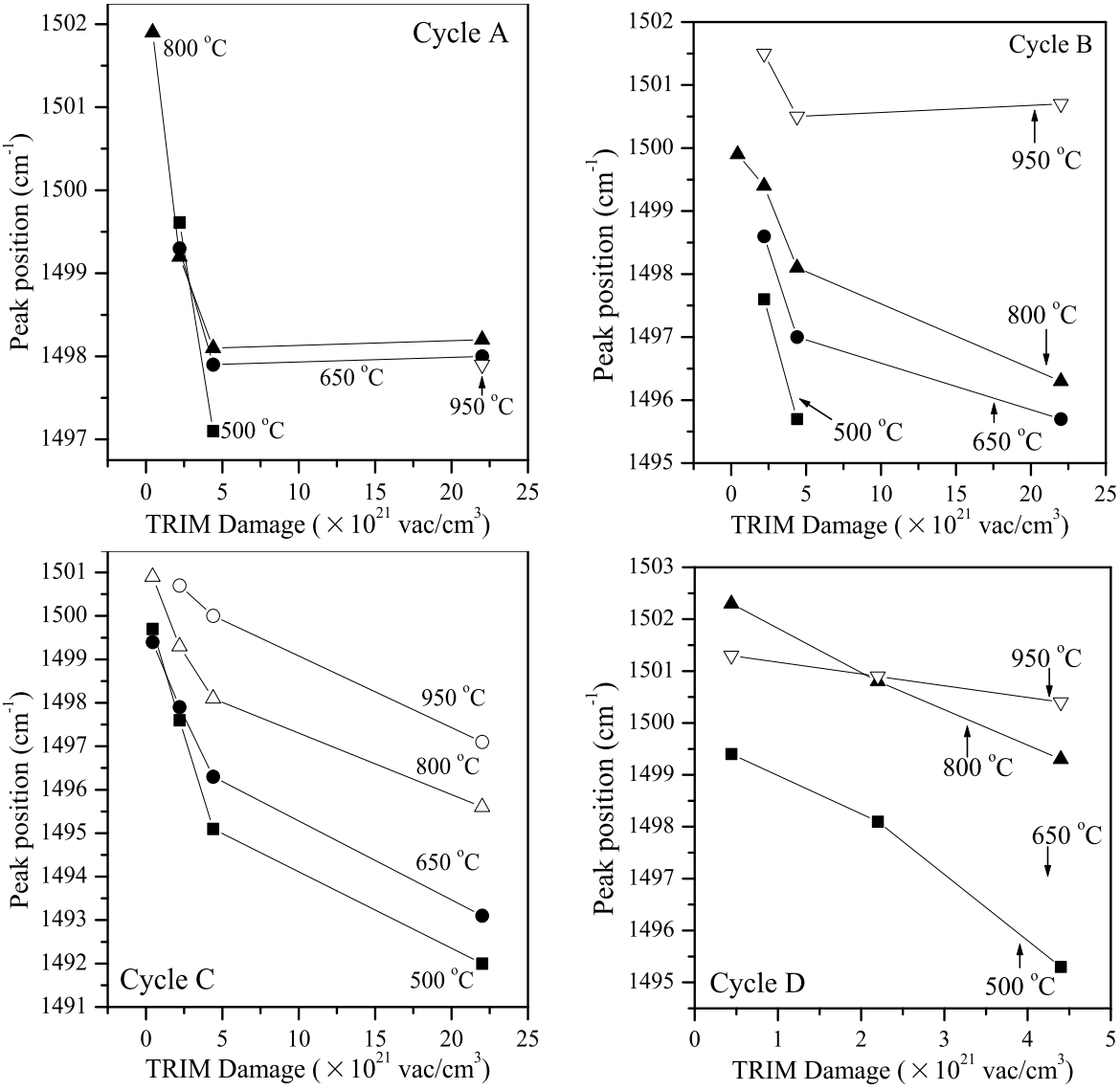


Figure 4.29: 1498 cm^{-1} peak position versus TRIM damage.

anneals the implanted layer has a higher amount of stress and higher defect density. This is typically where the 1638 cm^{-1} peak shifts and peak widths are assessed. Hence the broad band at 1630-1658 cm^{-1} is indeed an overlap of two peaks and both broadened by strain. Hence the peak position and peak width of the 1638 cm^{-1} Raman shift cannot be easily monitored. This is not the case for the 1498 cm^{-1} Raman shift which only becomes well defined after annealing at 500°C.

One of the debates in present literature regarding ion implantation into diamond is:

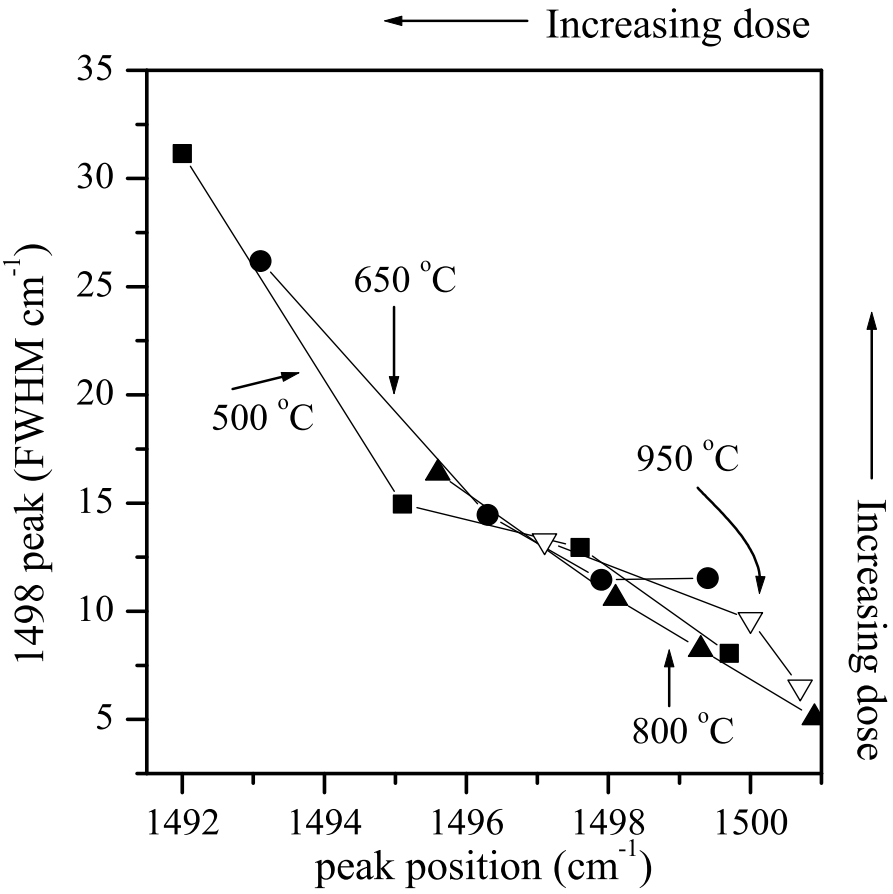


Figure 4.30: Peak width plotted against peak position for cycle C. The lines joining the points are for guiding the eye. A linear approximation can be deduced between the two quantities. The same is reported for MeV implanted diamond [13].

why does diamond reach an amorphous or graphitized state for an implanted dose that is substantially lower when compared to ion implanted silicon to reach an amorphous state? One of the more popular models that have been used to address this discrepancy in diamond is the Morehead and Crowder model [13]. In this model it is assumed that an ion forms amorphous islands during its passage through the crystal. The energy to create an amorphous cluster is argued to originate from displacement spikes in which large amounts of energy are deposited in a short space of time within the collision cascades of the implanted ions. Close to the projected end of range where most of the implanted ions come to rest, the energy deposited is more intense and clusters that form eventually begin to overlap and form a connective network. However Prins

and Derry [36] argue that diamond being a radiation hard material will be less prone to diplacement spikes forming along a collision cascade. Friedland and Sellschop also show that the cascade density and size for light ions (carbon) implanted into diamond is rather low [108]. Orwa *et al* [13] use the Morehead and Crowder model to explain the saturation of a band that appears in the Raman spectrum close to $1250\,\mathrm{cm}^{-1}$. In their Raman setup, the data could be acquired with a polarization technique that removed the Raman diamond line from the Raman spectra and thereby enhanced the defect peaks. They argue that the observed Raman shift at $1250\,\mathrm{cm}^{-1}$ lies close to a peak in the vibrational density of states of diamond (see section 2.3.6). In the implanted layers produced by keV implanted diamond we see evidence of this 'band' by observing in the spectra for cycle D - region 3 (see label (b) fig 4.22) after the $300\,^{\circ}\mathrm{C}$ anneal. We did not have the setup to acquire the data in the polarization mode as performed by Orwa, but the step height as it is labelled (see label (b) fig 4.22), is clearly evident for most of the spectra collected in cycles B, C and D. It is it not clearly evident in any of the spectra collected for cycle A. Initially when this step height appeared in MeV boron implanted diamond the same group [13, 156] assigned it to skewing of the first order diamond Raman line. We cannot conclude whether this defect appears as a band or if the observed step height is due to skewing of the first order diamond line. In either case one could assign this behaviour to the formation of amorphous regions within the implanted layer. Prins in [28] was able to show that Orwa's data could be modelled by ballistic self annealing during ion implantation and this depends only on ballistic type processes. We also recall that the CIRA approach to doping diamond is modelled entirely by vacancy-interstitial reactions within the implanted layer which have been created by the implantation process. We cannot directly compare the observations reported in this work to the behaviour of the amorphous band as obtained in MeV implanted layers since we do not have a reference with which we can normalise the data. For keV implanted diamond the observed Raman shift for the diamond line includes scattered light from regions below the implanted region. In Mev implanted diamond, the Raman shift for the diamond line is measured in a cross-sectional configuration

such that the scattered light emerges entirely from the implanted region. In this case the intensity of first order diamond Raman line serves as a meaningful normalisation factor [13]. We can nonetheless infer that amorphous regions are possibly created for both MeV and keV implanted layers if we accept that the 1200-1250 cm^{-1} Raman shifts are due to amorphous diamond. This is still an unresolved issue, since Ferrari and Robertson assign this Raman shift to transpolyacetylene (trans-PA) [127]. The origin of trans-PA is well understood in CVD diamond and nanodiamond and can be deduced from double-bonded carbon chains which are terminated by hydrogen. In this case Raman shifts near 1150 cm^{-1} and 1460 cm^{-1} are argued to orginate from trans-PA. When nanocrystalline diamond is produced by shock synthesis a peak near 1240 cm^{-1} is observed in the Raman spectrum and its origin is also argued to be from trans-PA in the absence of hydrogen [127]. To make the assignment of the observed Raman shift near 1200-1250 cm^{-1} in ion implanted diamond to trans-PA is debatable. We can conjecture that it is possible that double-bonded structures could form from the interstitial carbon atoms created during the implantation process. It is interesting to note that we observed Raman shifts near 1230-1250 cm^{-1} in some virgin spectra after annealing. Further to the arguments presented by Prins, Friedland and Sellschop, Nakata presents an interesting model which describes how amorphous structures can be created by ion implantation by considering inelastic energy loss processes and elastic energy loss processes without recoil [37].

Orwa *et al* do state that as yet, no one has reported the formation of graphitic type clusters during implantation. We cannot make concrete suggestions that will support any particular model with the data presented here. Further experimentation using transmission electron microscopy (TEM) on thin layers of diamond may reveal a suitable data set with a consistent model.

4.5 Conclusions

The results acquired from this study were the first to demonstrate that the 1498 cm^{-1}, 1450 cm^{-1} and 1638 cm^{-1} peaks are also created during keV implantation and are not unique to MeV implantation [1]. The reason why they were not seen in earlier work in keV implanted diamond was due to strain in the implanted layer. It thus shows that the the point defects created by the implantation process are not determined by the implantation energy. It has been argued [31, 36] that it is primarily the implantation width that is the determining factor in the way that the defects anneal that are created during the implantation process. This argument is confirmed in this study by observing that when the dose was implanted at a single energy the layer collapsed to graphite in the cases for region 4 and 5 described earlier. For low energy implantation the interstitials that diffuse away from the implanted layer easily migrate to the surface, where they remain. By implanting at high energies, one can argue that the width over which the point defects will interact has indeed increased, thereby increasing the probability of interstitial-vacancy recombination and thus allowing implantation to doses above the graphitization threshold. It has been suggested that because the annealing behaviour of MeV implanted diamond has a much higher graphitization threshold then keV implanted layers, this should result in much better doping of diamond. Vogel *et al* [32] observed that for a MeV implanted boron layer at doses well below the graphitization threshold only resulted in higher dopant activation but the hole mobilities they measured were low. It is clear from results of Vogel that even though the diamond Raman line is restored to its pristine state after implantation, there are still defects within the implanted regime that are not Raman active. This suggests that some of the vacancy type defects that give rise to the 1454 cm^{-1} and 1498 cm^{-1} peaks may have aggregated to some type of vacancy superstructure or collapsed to extended defects which are most likely dislocations.

We can therefore conclude that the CIRA process and implantation over a large width provides a suitable way to dope diamond and reduce the defect structures that

are created during the implantation and post-annealing process. It is particulary noted that for a CIRA implanted layer, defect clusters associated with 'amorphous' diamond are not present following an anneal at 500 °C. It also appears more likely that in order to generate doped diamond with high carrier mobilities and higher dopant activation, it would be preferable to choose a low dose and perform multiple implantation steps over a large width using the CIRA approach.

Chapter 5

Electroluminescence in ion implanted diamond

5.1 Introduction

The fabrication of active electronic devices in diamond, requires the need for ohmic [110] and rectifying contacts [20, 21, 158]. Both p- and n-type materials are needed to effect a pn-junction. At present, p-type layers can be prepared by different methods [17, 159, 160], and this is being done in many laboratories. However, good quality n-type layers have been more elusive to attain. High dose ion implantation into diamond causes severe damage [chapter 4], but such layers can act as if they are n-type regions [17]. Employing this approach, bipolar transistor action [17] and electroluminescent (EL) junctions [161] could be prepared using natural type IIb diamonds as substrates. Sullivan and Baragiola [162] used ion beam induced luminescence (IBIL) to study the EL generated by the process used in [161]. In the above experiments high dose carbon implantation was used to create the 'n-type' region.

Recent results strongly indicate that n-type layers may be attainable when doping with phosphorus atoms [163–165]. In order to effect ohmic contacts to such n-type layers, a multiple implantation procedure, using P^+ ions, has been developed [166]. It

was found that such an implantation sequence into p-type semiconducting diamond, renders an electron injecting contact. This use of phosphorus, instead of high-dose carbon-ion implantation (as mentioned above) is of considerable interest, since it could lead to more efficient diode junctions in diamond. In this chapter the electroluminescence from both C^+ and P^+ ion junctions, is compared and studied in relation to the annealing temperature and diode operating temperature and compared with luminescent bands induced by cathodoluminescence. Other methods of inducing electroluminescence in diamond are discussed in [167, 168] (impact ionization due to avalanche breakdown at high electric fields) and [4, 51] (CVD doped layers).

5.2 Experimental procedure

A rectangular, single crystal type IIb diamond with dimensions of $5 \times 2 \times 1.6\,\mathrm{mm}^3$ polished in the {100} direction was used. On one broad face an ohmic contact was made by overdoping this entire face with B^+ ions [169]. The procedure as outlined by Prins in [169] is consistent with the observations in chapter 4 (cycle D - region 5), where it is shown that for keV implanted diamond at a single energy with carbon ions, doses in excess of $5 \times 10^{15}\,\mathrm{ions/cm}^2$ will form a disordered graphitic layer after annealing at 500 °C. The above method in [169] and used in this work implanted boron ions to a dose of $3 \times 10^{16}\,\mathrm{ions/cm}^2$ at an energy of 30 keV. The diamond is annealed to 500 °C and the implanted layer which is near the surface is etched away when the diamond is boiled in an oxidising acid solution. At the etched interface there is a high enough concentration of boron ions which creates the overdoped ohmic contact. On the opposite face, the diamond was implanted at liquid nitrogen temperature [CIRA process] with either P^+ or C^+ ions, after it had been repolished to remove any traces of previous implantations, since this diamond had been used for experimentation before. The target holder was oriented 7° to the normal incidence of the beam in order to reduce any channelling effects. A dose rate of $\approx 10^{13}\,\mathrm{ions.s}^{-1}.\mathrm{cm}^{-2}$ was used in all of the implantation steps. The energies and doses used are given in Table 5.1.

This face was masked to demarcate an implanted strip with a length of 4.6 mm and a width of 1 mm, such that the strip intersected one of the edges of the surface (see fig. 5.1). A TRIM [75] simulation of the expected damage and range profiles, which should be near identical for both ions, can be seen in figure 5.2. As can be seen, the density of both the damage and range profiles increases rapidly towards the external surface. At a depth near the surface, the damage becomes high enough to graphitize the implanted region (as observed in chapter 4). After the first rapid thermal anneal (RTA) to 500 °C in an argon atmosphere, this graphitized layer was etched away, by boiling in an oxidising acid solution, to leave a surface which had been damaged to just below the graphitization threshold, and which, in the case of the P^+ ion implantations contained a high density of phosphorus atoms. For both the P^+ and C^+ implanted layers that remain at the etched surface, it is observed that they both form an effective n-type injection electrode.

After the etching step, which also ensured that the diamond was clean, the back surface (which had been made ohmic) was covered with silver paint and the diamond

$^{31}P^+$		$^{12}C^+$	
Energy (keV)	Dose ($\times 10^{14}$ ions/cm^2)	Energy (keV)	Dose ($\times 10^{14}$ ions/cm^2)
30	10		
45	8	25	63
70	6	30	21
95	4	43	14
120	2	55	7
145	1	67	3.5
170	0.5	80	1.75

Table 5.1: Ion energies and doses used for the P^+ and C^+ diode junctions in type IIb diamond. According to the TRIM simulation program, the maximum depth traversed would be $\approx 0.16\,\mu$m for both ions. The multistep implantation sequence is achieved by implanting the dose fraction indicated at the highest energy and then moving up along the column to the next energy and implanting the dose fraction at that energy and so on. A total dose of 11.025×10^{15} ions/cm^2 was implanted for the C^+ junction, whereas the P^+ junction had a total dose of 3.15×10^{15} ions/cm^2.

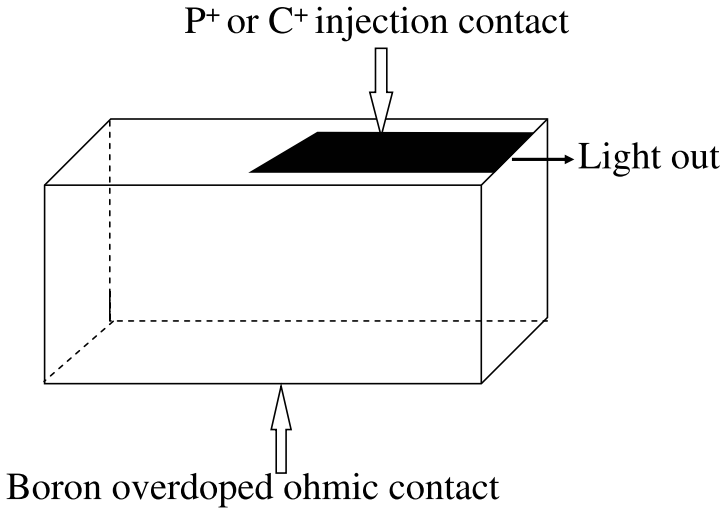


Figure 5.1: Device set-up (not drawn to scale). The above configuration was clamped in a specifically designed holder to measure the IV characteristics, and thereafter placed in a chamber with a monochromator assembly and photomultiplier tube so that the light output could be recorded.

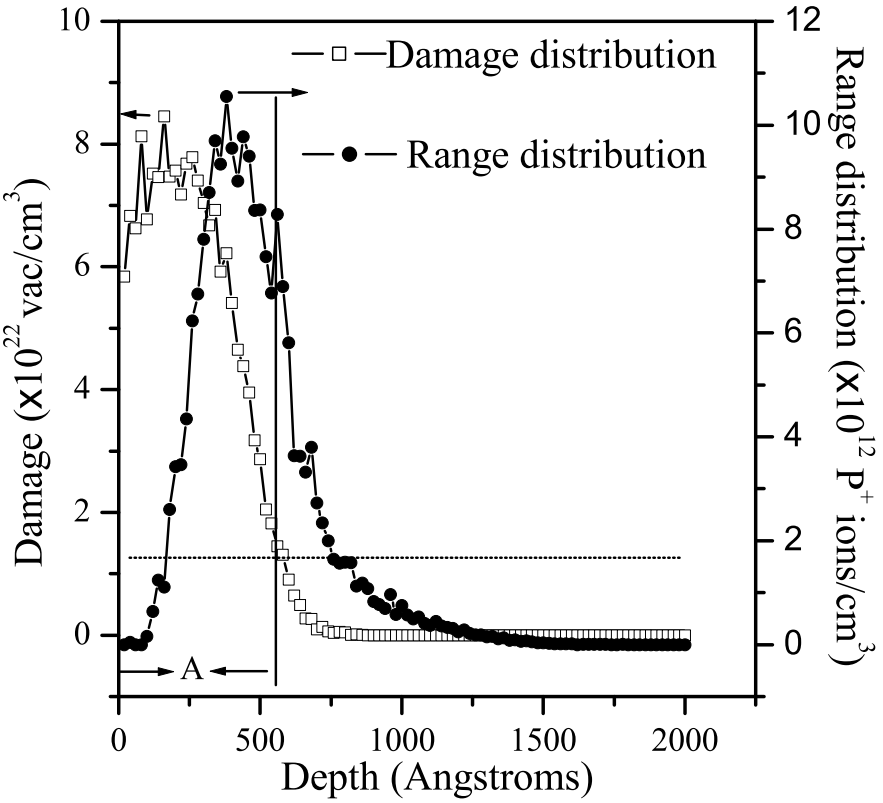


Figure 5.2: Damage and range profiles for the P^+ junction as obtained from TRIM98 with $E_d = 45\,\text{eV}$. The doses and energies used are shown in table 5.1. A similar profile is obtained for the C^+ implanted junction. Based on our observations of chapter 4, we could expect that implanted layer above the dashed line (close to $1\times10^{22}\,\text{vac/cm}^3$) will form a graphitic layer which will be etched away when boiled in an oxidising acid solution. The region demarcated A is within a rough approximation the layer that is removed by boiling in the hot acid solution. The shape of the profiles suggests why the diodes are considered graded np-junctions as argued in the text.

allowed to bake at 360 °C for 6 to 8 hours in air. Electrical contact to this face was achieved by clamping the diamond in the target holder against a flat copper contact which was connected to the power supply. Contact to the implanted strip on the front surface was effected by pressing a gold-wire strip to it whilst mounting it in a special sample holder designed for the diamond used in this experiment. The sample holder was mounted within a cryostat in a way that would ensure that any light that may emerge from the edge of the diamond will impinge onto the slit of a McPherson model 275 scanning monochromator. A Hamamatsu model R298 photomultiplier (PM) tube was used to record the light intensity as a function of wavelength. This was done while applying different forward bias voltages across the diode junction, and also at reverse biases up to 30 V. Results were recorded at different temperatures as well as after isochronal anneals lasting one hour each at 700, 900, 1100, 1300 and 1500 °C. Before and after each anneal the diamond was cleaned by boiling in acids, and before the next measurements silver paint was again applied and baked onto the boron overdoped ohmic contact.

5.3 Results

The current-voltage (IV) characteristics of both the C^+ and P^+ implanted junctions showed rectifying behaviour (fig. 5.3). Owing to the fact that the top contact had been made by merely pressing a gold wire against the implanted surface, one cannot guarantee that the active junction area had been exactly the same for all the measurements. It is, thus, not possible to directly compare the current densities or, for that matter, the light intensities measured.

Light emission from the junctions started at a forward bias of ≈15.0 V and increased in intensity with increasing voltage. No light emission could be observed in reverse bias up to and below reverse breakdown. In all of the electroluminescence (EL) spectra measured, the well known blue band A (BBA), situated at 2.9 eV dominated when exciting the junction at room temperature. After anneals at 500, 700, and 900 °C, the EL spectra, when excited at junction temperatures above room temperature, contained

the green band (GBA) feature around 2.4 eV. This was the case for both the C^+ and P^+ junctions. The spectra shown in fig 5.4 and 5.5 show a selection of spectra obtained from the EL junctions under different foward voltages and temperatures.

At high temperatures, above ≈100 °C, the intensity of this green band could even exceed that of the blue band. This is shown more clearly for a set of selected spectra in fig. 5.6. This has also been observed in cathodoluminescence (CL) [170].

After a further anneal at 1100 °C, bands centred around 4 eV (in the Ultra-Violet (UV)) and 2.06 eV (in the red part of the spectrum) appeared in the case of both junctions (shown more clearly in fig. 5.7). In contrast, the green 2.4 eV band could no longer be generated as before at high diode operating temperatures of the order of 100 °C and above. The 4 eV (UV) band decreased in intensity after annealing at 1300 °C and became barely visible after further annealing at 1500 °C. The 2.06 eV emission was no longer visible in the EL spectra after the 1300 °C anneal. A striking

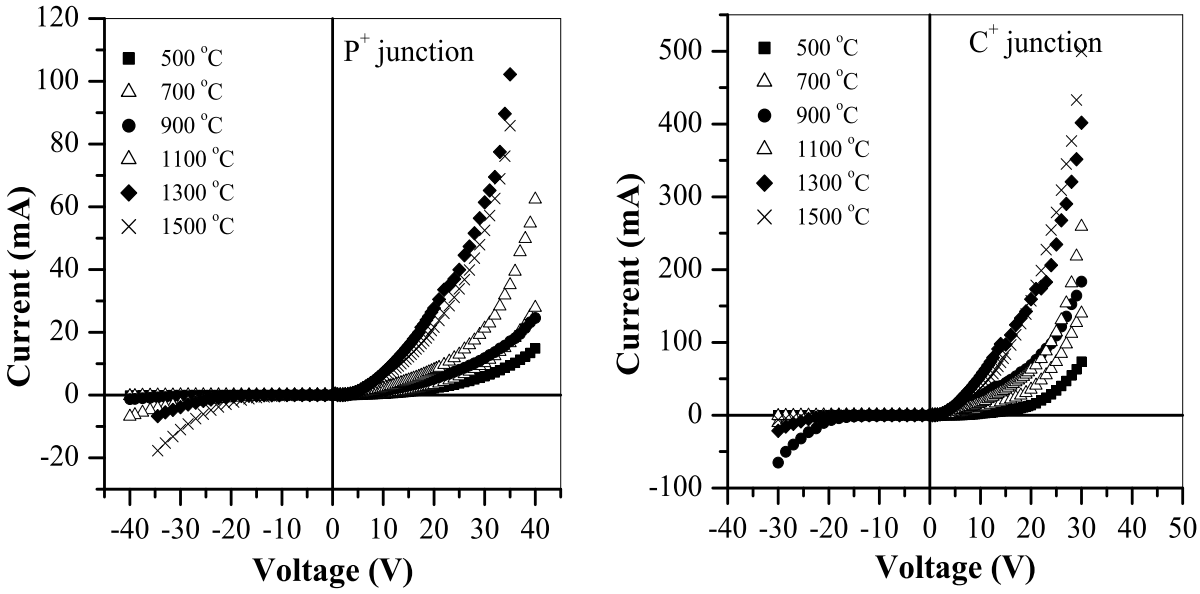


Figure 5.3: Typical IV curves obtained for the diode junctions. The legend describes the IV curve measured after annealing the diamond at that temperature. All measurements were done at room temperature. No conclusions are made with respect to the current density since the device set-up did not yield the same active area for different measurements.

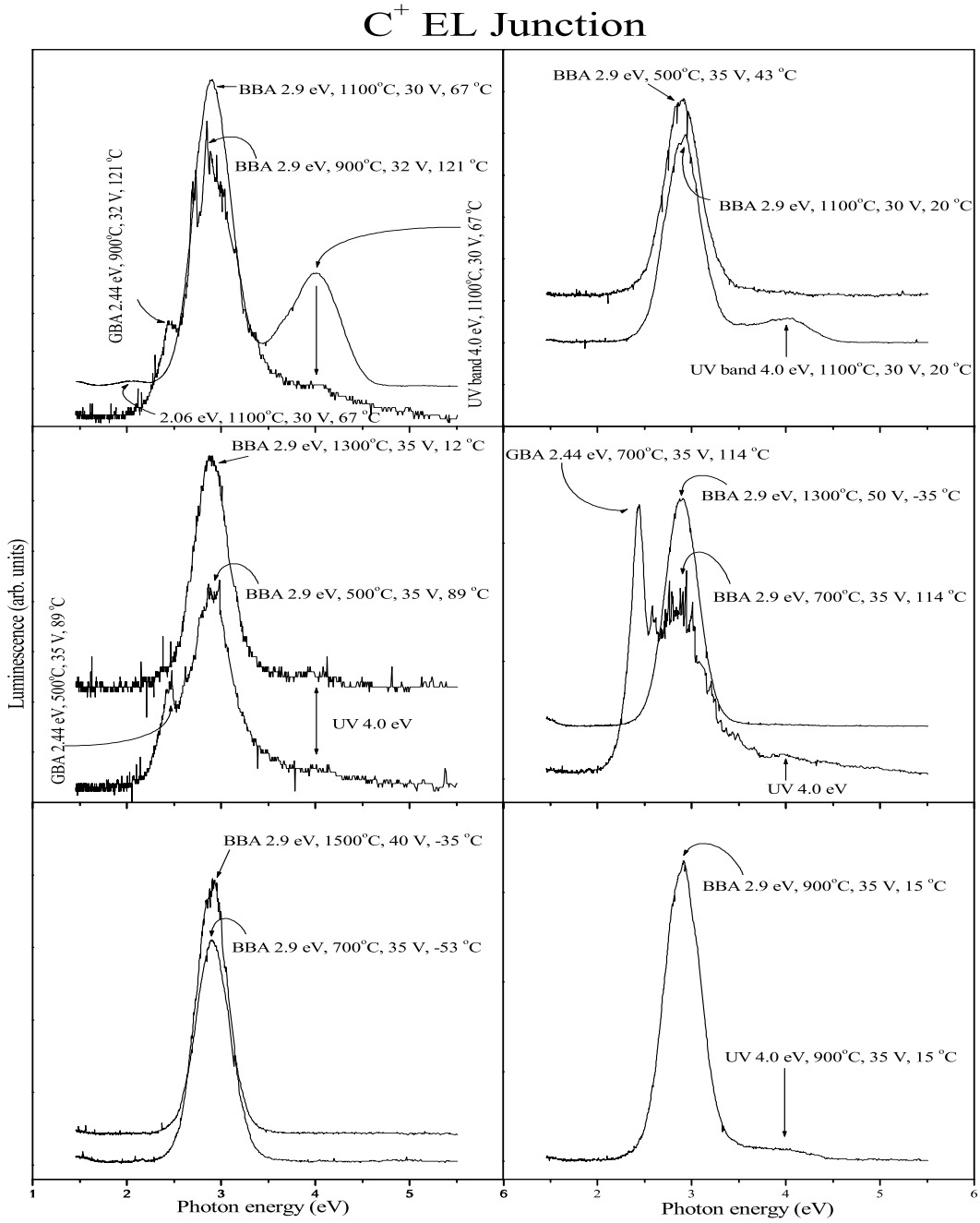


Figure 5.4: EL spectra measured for the C^+ junction under different foward voltages and diode operating temperatures. The peak assignment, peak energy, annealed temperature, bias voltage and diode temperature are listed alongside each of the peaks in the spectra shown. Since the active area of the junctions were not the same for different measurements, no conclusions were made with respect to the measured intensities.

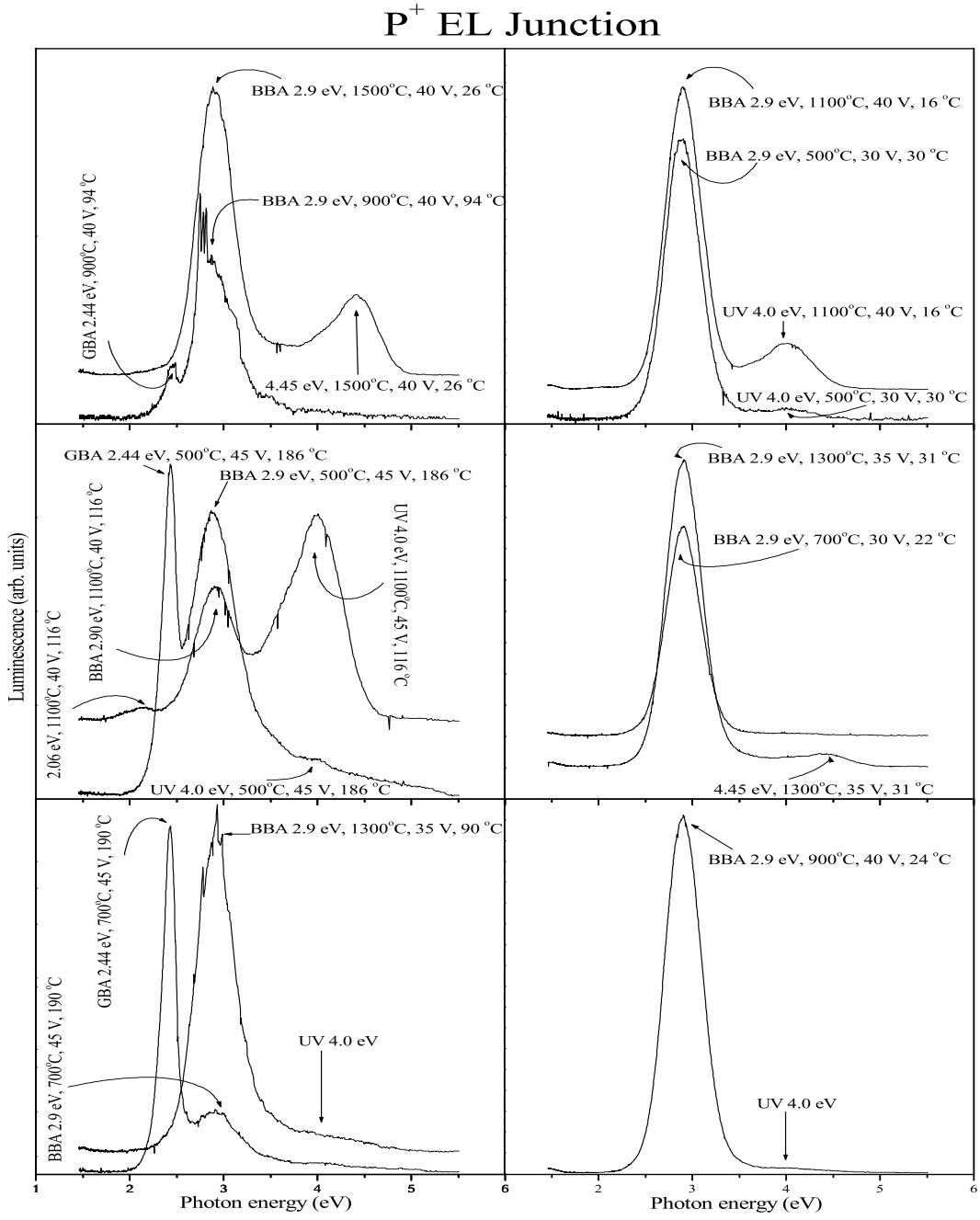


Figure 5.5: EL spectra measured for the P^+ junction under different foward voltages and diode operating temperatures. The peak assignment, peak energy, annealed temperature, bias voltage and diode temperature are listed alongside each of the peaks in the spectra shown. Since the active area of the junctions were not the same for different measurements, no conclusions were made with respect to the measured intensities.

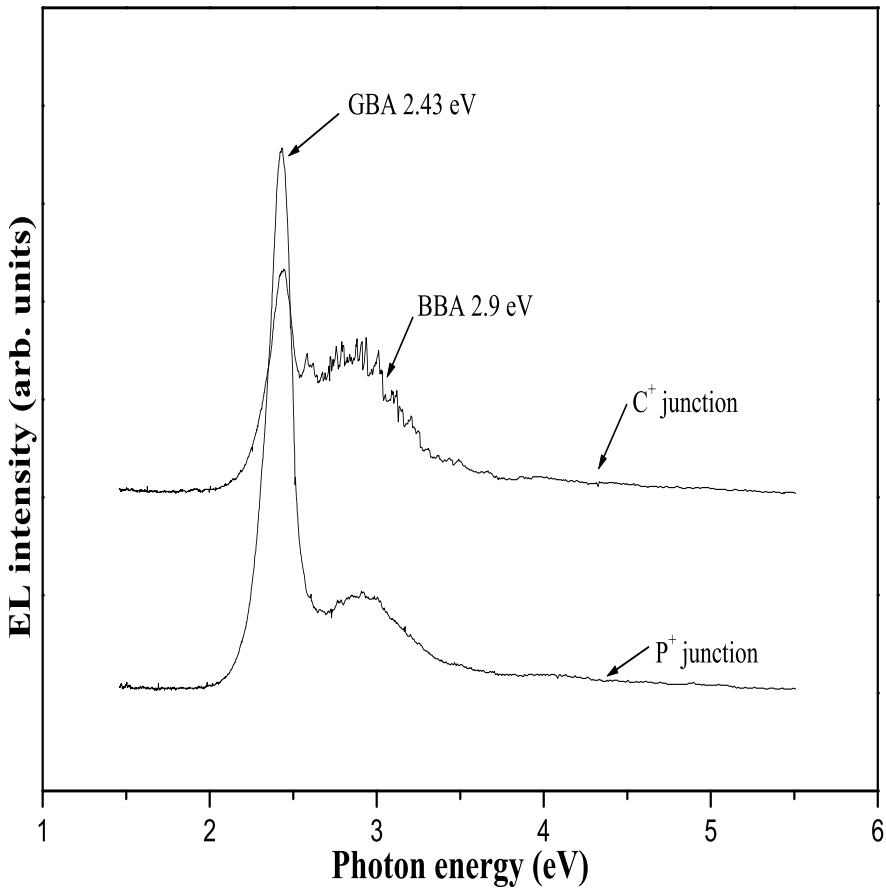


Figure 5.6: EL spectra measured following an anneal at 700 °C. The P^+ spectrum was recorded at 190 °C at a forward bias of 40 V. For the C^+ junction, a forward bias of 35 V at 112 °C was used. Both junctions show the generation of Green Band A luminescence at high temperatures. Similar spectra, (as can be seen in fig 5.4 and 5.5) at high diode temperatures, are obtained following the anneals at 500 and 900 °C. Since the active area of the junctions were not the same for different measurements, no conclusions were made with respect to the measured intensities.

difference between the C^+ and P^+ junctions only appeared after the 1300 and 1500 °C anneals (see fig. 5.8). A band centred around 4.45 eV appeared in the spectrum from the P^+-junction, but not from the C^+-junction.

5.4 Discussion

Owing to the implantation profiles which were used to effect the injecting contacts in this study (fig. 5.2), the damage, and implanted ions, would have been highest at the surface while decreasing with depth. Assuming that the boron acceptors are uniformly distributed in the type IIb diamond, these implantation profiles would, thus, have established graded np-junctions where, near the end of range, the boron acceptors will dominate with further depth. Whereas in the case of the C^+-junction the donor centres would all be damage-related, the P^+-junction should have had both these same damage-related donors as well as, hopefully, also activated phosphorus donors. The idea of the graded np-junction is consistent with the results obtained in chapter 4 where we observed that graphite and graphitic like carbon will be formed near the region where the damage density is in excess of 1×10^{22} vac/cm^3. It is logical to accept that the n-p interface formed at the position where the density of the implantation-created donor centres is the same as the density of the boron acceptors within the diamond. From this neutral interface, the density of the donors will increase towards the surface, and the density of the uncompensated boron acceptors will, likewise, increase with depth to reach the bulk value at the end of the implanted ion range.

When biased in the forward direction, electrons are injected into the p-type, lower lying substrate, while holes are injected into the implanted 'n-type' contact region. On both sides of the junction, there exist depletion layers generated by ionised boron acceptors (negatively charged) on the p-type side and positively charged donors on the n-type side. These electrons and holes can relax to lower lying energy states by non-radiative transitions (for example phonon-related processes) or some radiative de-excitation. Consequently any luminescence, except for free exciton luminescence, will

be related to defect structures and their associated energy levels in the band gap. From previous results [171], it has been argued that the blue 2.9 eV luminescence band (BBA) occurs by recombination of electrons and holes at a deep lying acceptor-like state. It first traps an electron from the conduction band and then captures a hole from the valence band, which then recombines while radiating the blue ≈2.9 eV luminescence. Assuming this mechanism to be correct, the blue luminescence should be generated within the p-type material of the junction, by de-excitation of the electrons injected into it. It is also probable that the BBA luminescence is also generated near the n-type region since the implanted dose near the surface was above the graphitization threshold. We could expect that extended defects were generated within this region due to the implantation-annealing process. It is highly likely that the extended defects that arise from the implantation-annealing procedure could well be dislocations. BBA luminescence has been observed to be more intense near dislocations within the diamond crystal [172, 173].

It is well established that the green band at ≈2.4 eV (GBA) only appears when boron acceptors are present [172, 174–176]. Since a natural IIb diamond was used in this experiment, it is more probable that the 2.4 eV band is related to the presence of the boron, and not the H3 centre which forms when vacancies are trapped at nitrogen A aggregates, which also has a mean energy of luminescence at ≈2.4 eV. In this study it could only be observed after the lower temperature anneals (below 1100 °C) and when the diode interface was at a sufficiently high temperature (see fig. 5.6). It has been proposed that the green band is related to blue band A, in that the light is generated at the same recombination centre after it has trapped an electron, but that in this case, the hole which is captured, for recombination to occur, comes from a neutral boron acceptor and not from the valence band [170]. If this is the case, then the green 2.4 eV band cannot be generated by electrons within the depletion region on the p-side, but only by electrons injected right across it into the lower lying substrate where neutral acceptors can be found. Thus its disappearance after the higher temperature anneals indicates that very few electrons are able to traverse the whole width of the depletion

layer on the p-type side.

When annealing the implanted diode junctions at increasing temperatures, the density of the damage-related donors on the n-type side decreases [149]. It is believed that the vacancies, which on their own can also act as donor centres [177], start to diffuse at temperatures above ≈500 °C. It is logical to assume that after the 500 °C anneal, the damage-related donors are mostly the vacancies. Electrical measurements indicate that anneals at higher temperatures than 500 °C, cause the vacancies to agglomerate, in this way forming more complex, extended defects (called *vacloids*), which, like the single vacancies, can act as donors [27]. This is supported by the Raman spectra acquired in chapter 4, where it was observed that the vacancy related defects become prominent after annealing above 500 °C. We cannot conclude that the Raman active defect peaks related to the vacancies are in any way related to the luminescent bands observed in EL, but we can at least conclude that within the parameters of the implantation steps performed and annealing temperatures used, that the UV band is created from the vacancies or vacancy related structures created as a result of the implantation-annealing process.

However, because each vacloid consists of many vacancies, their number density is less than that of the single vacancies, which results in a decrease of donor centres. Furthermore, vacancies can diffuse into the p-side and form vacloids which will compensate boron acceptors lying deeper than the implanted ion range. On both the n- and p sides, the respective densities of uncompensated donors and acceptors will, accordingly, decrease. Owing to the decrease in donor centres at the position of the original, neutral n-p interface, the new interface will be situated nearer to the surface. In other words, with each anneal which reduces the donor centres, this interface could move towards the surface, leaving in its wake a deeper region that contains an uncompensated density of boron acceptors which is lower than the bulk value. This will cause the width of the depletion layer on the p-side to increase, which makes it more difficult for the electrons being injected from the n-side to traverse it and meet up with neutral acceptors, thus

reducing the possibility of generating the green, 2.4 eV band.

As can be seen from figures 5.4 and 5.5, the disappearance of the green luminescence band is accompanied by the appearance of the 4 eV (UV) band. It should thus be possible to also explain this UV band in terms of the same changes at the n-p interface that led to the disappearance of the green band. It has been concluded from cathodoluminescence (CL) studies, that the 4 eV UV band could be the fingerprint of the vacloid donors [178]. According to this model, these extended donors luminesce by first trapping a hole from the valence band, followed by capturing an electron from the conduction band. As mentioned above, the anneals at temperatures above 600 °C, will lead to the formation of these extended donor defects, and the fact that they appear in the EL spectrum is thus not surprising. Holes injected from the p-side into the n-side can de-excite to neutral vacloids, which then subsequently capture electrons from the valence band. Thus, as already proposed previously, the 4 eV UV band is excited within the 'n-type' layer [171].

CL studies showed that the 4 eV UV band anneals out at temperatures above ≈1400 °C [149]. In the present study, this also occurred. Although electrical measurements showed that the density of these vacloid centres do, indeed, decrease with such anneals [179], it also showed that this density does not become zero. Thus, although the 4 eV UV band cannot be seen any more, the diamond still contains some of the donor-like recombination centres believed to be responsible for this luminescence. It seems that with these high temperature anneals, some of the donor-like vacloids change their nature to become acceptor-like, extended defects responsible for the blue 2.9 eV luminescence [149]. These results indicate that both types of recombination centres form from the agglomeration of vacancies, with the donors dominating after low temperature anneals while the acceptors dominate after anneals at higher temperatures. Thus, the anneals at 1300 and 1500 °C, would have led to an increase in the 2.9 eV recombination centres at the expense of the vacloid donors. The fact that the diode characteristics did not disappear altogether, is a further indication that not all the

donors change into 2.9 eV recombination centres. Nevertheless, the decrease in donors at the neutral n-p interface, will force it nearer to the surface thus further increasing the width of the p-type depletion layer. This correlates with the fact that the 2.4 eV band could still not be observed after the high temperature anneals (fig. 5.7).

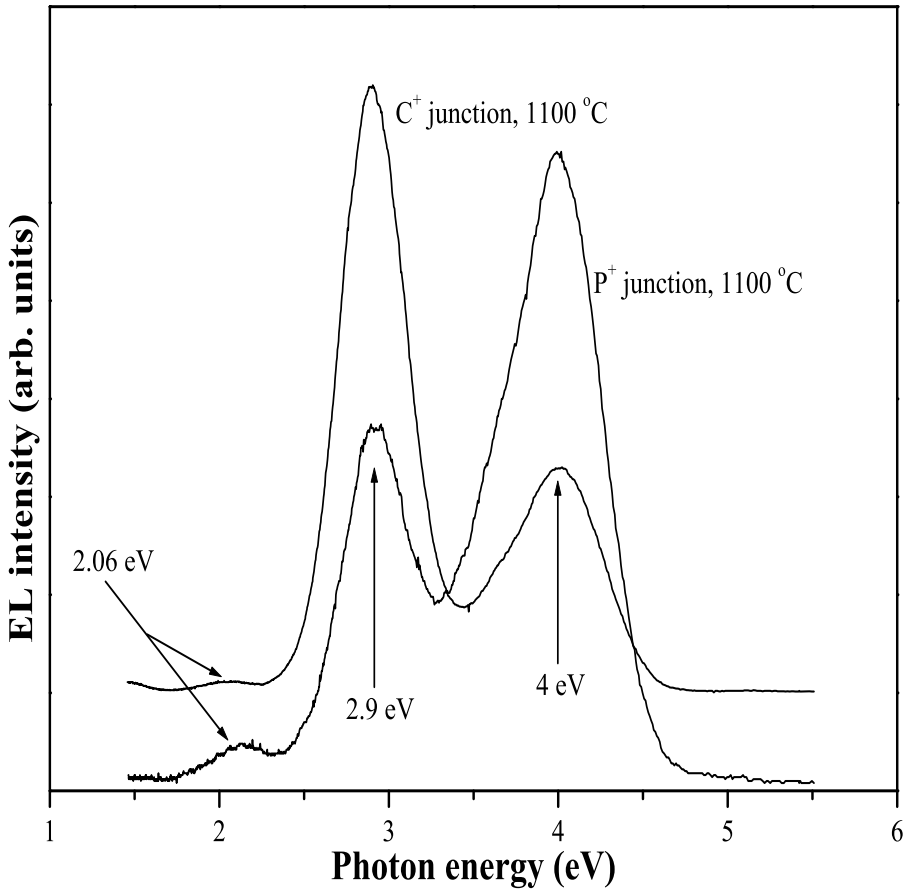


Figure 5.7: EL spectra measured for the C^+ and P^+ junctions after annealing at 1100 °C. The spectrum obtained for the C^+ junction was at a forward bias of 30 V and a temperature of 67 °C. The P^+ spectrum was recorded at a forward bias of 40 V at 111 °C. There is no indication of the 2.4 eV band even at a high diode temperature. The 2.06 eV band and 4 eV bands were prominent after the 1100 °C anneal. No conclusions are made with respect to the emitted intensities.

However, after these high temperature anneals, the first striking difference developed between the EL spectra of the C^+ and P^+ diode interfaces, is the appearance of a

band centred around 4.45 eV, which appears only in the P^+ injection junction (fig. 5.8).

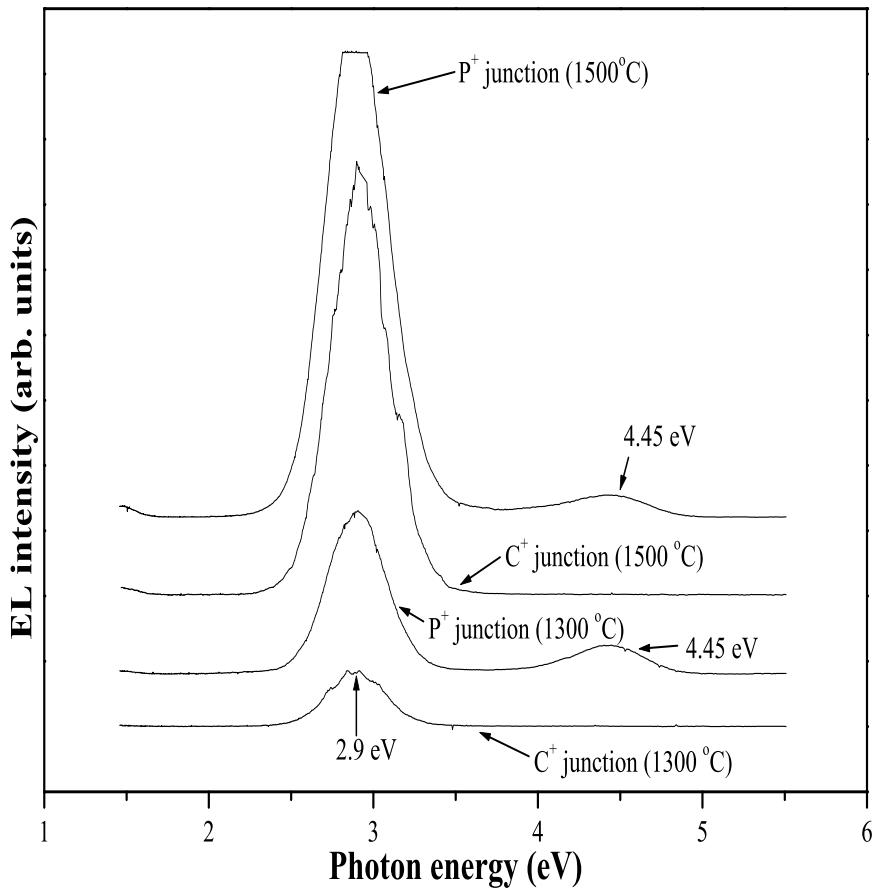


Figure 5.8: Electroluminescence spectra obtained for the C^+ and P^+ diode junctions after the anneals at 1300 and 1500 °C. Both junctions emitted blue band A (2.9 eV), while only the P+ junction had a UV emission centred around 4.45 eV. The C^+ (1300 °C) and C^+ (1500 °C) spectra were recorded at a forward bias of 40 and 45 V, while the diode operating temperature was at -34 and -45 °C respectively. The P^+ (1300 °C) and P^+ (1500 °C) spectra were recorded at a forward bias of 40 and 35 V, while the diode operating temperature was at -39 and 22 °C respectively. There are no indications of the 2.06 and 4 eV band nor could the 2.4 eV band be generated after the high annealing cycles. No conclusions are inferred from the emitted intensities.

From CL studies on various p-type substrates, a band centred around 4.6 eV has been reported [170, 174–176, 180, 181]. There is now no doubt that this band only appears when boron acceptors are present [175, 176]. It has been proposed that this band may be an energy shifted near replica of the 4 eV band, where the energy shift occurs under the influence of ionised (negatively charged) boron acceptors [170]. It

is tempting to speculate that the 4.45 eV band is the counterpart of the 4.6 eV band, which in this case forms under the action of the phosphorus donors. However, if the 4.6 eV band is a higher photon energy replica of the 4 eV band under the action of negative boron acceptors, one would have expected that the shift should be to a lower photon energy under the influence of the positively charged phosphorus donors. Thus the proposed model for the 4.6 eV band may be wrong, or the 4.45 eV band is not related to it. The latter conclusion is supported by the fact that the 4.6 eV boron related band could only be observed at low temperatures (near liquid nitrogen) in cathodoluminescence studies, while the phosphorus related 4.45 eV band observed in this study by EL was also present at room temperature.

An alternative to the origin of the 4.45 eV band can be a simple case of recombination between the P^+ donor and boron acceptor. This is illustrated in fig. 5.7. It is highly probable that at some point along the np-junction, there will exist a region within the implanted layer where the activated boron and phosphorus atoms will lie in close proximity to each other. Based on the analysis presented in [48, 182] one could infer that the donor level of phosphorus lies close to 0.63 eV for the observed EL of 4.45 eV with respect to donor-acceptor recombination (DAP) between the activated boron and phosphorus defect levels. The broadening of the band could be the result of the strain induced due to the implantation process.

The 2.06 eV band appeared and disappeared with the 4 eV band, suggesting that it is related to it or some other vacancy related defect. A reasonable argument as to the possible origin of the 2.06 eV band is still under investigation.

5.5 Conclusions

Similar bands to those excited by CL, have been observed in both the P^+ and C^+ injection contacts, by EL. A broad band, centred around 4.45 eV is only observed in the P^+ junction. The 4.45 eV luminescence produced in this work is the first observation by EL. The same band was also produced in the work of Koizumi [183], but they did

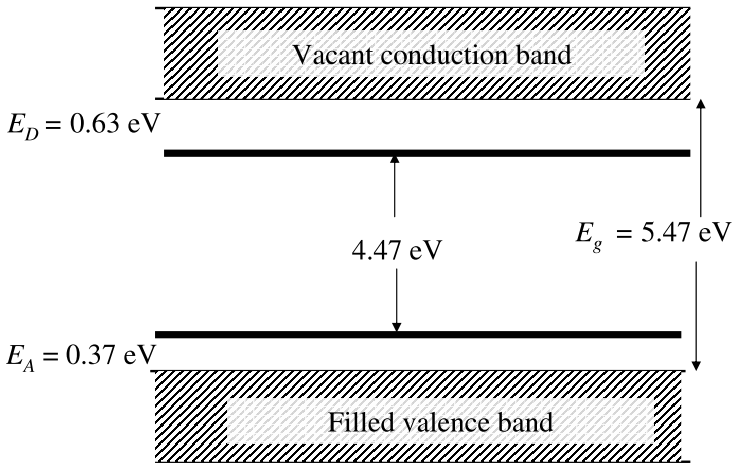


Figure 5.9: Recombination between activated phosphorus and boron (DAP recombination) can be used to explain the origin of the 4.45 eV observed in the EL diodes fabricated in this study.

not cite the result published in [2] as the first observation of the band by EL. For the BBA emission we continue to argue that its origin results from a charged acceptor at 2.9 eV above the valence band which recombines with a hole in the valence band, while the green band luminescence is a radiative transition from the ionised 2.9 eV acceptor to the neutral boron acceptor levels. The UV band at 4 eV below the conduction band, is related to the donor centres created by vacancies, and the resultant emission is regarded as electron transitions from the conduction band to the ground states of these donors. Tentative arguments related to the 4.45 eV band have been proposed, while the 2.06 eV band will be investigated further. This method of creating a diode junction has opened a useful avenue to investigate recombination luminescence from defects in diamond. The results also reveal that with a suitable n-type dopant, minority carrier injection is possible in p-type diamond. With suitable refinements, the method can therefore help in the realisation of useful semiconductor devices in diamond.

Summary and conclusions

The content of this thesis has focussed on three pertintent issues in the evolution of diamond electronics. In chapter 3 we considered an alternative approach to grow diamond on a FCC crystal (Cu and Cu-Ni) which can be easily extended to larger dimensions. No conclusive evidence was found to indicate that single crystal diamond could be realised using the experiment outlined in this initial study. We hope to continue this research endeavour when the analysis equipment is fully functional. The work in chapter 4 focussed on the radiation damage that ocuurs as a result of ion implantation into diamond which can be viewed as an interpenetrating FCC lattice. Ion implantation is presently considered as the best means of introducing dopants into the diamond lattice to high concentration for semiconductor application. In this study keV implantation was used and no substantial differences were observed when compared to MeV implantation as reported in the literature. This research suggests that in order to minimize the radiation damage and obtain high dopant activation, this will be best achieved by low dose multiple CIRA implantation steps over a wide energy (depth) range. The results of chapter 4 also suggest that there is strain generated in the implanted layer during keV irradiation. It is possible that strain generated in the near surface layers will have a deleterious affect when attempting to generate single crystal growth by implantation and outdiffusion processes as attempted in chapter 3.

In chapter 5, an electroluminescent junction is generated by ion implantation in a natural type IIb diamond. This work clearly demonstrates that ion implantation can indeed be used to create semiconductor devices in diamond and how the radiation damage in diamond (as a result of the implantation process) can be useful to create minority carrier injection contacts. It is also shown that EL junctions can be a useful tool to investigate defect bands that are created during the implantation process. This will be useful in our future research which will focus on finding shallower p-type and n-type dopants in diamond in the pursuit of establishing diamond as a superior candiate for semiconductor application in harsh environments.

Bibliography

[1] JF Prins, *Diamond Relat. Mater.*, **10**, (2001), 1756–1764.

[2] SR Naidoo and JF Prins, *Diamond Relat. Mater.*, **8**, (1999), 1502–1507.

[3] AM Zaitsev, *Optical properties of diamond: A data Handbook*, Springer-Verlag, Berlin, Heidelberg, New York, 2001.

[4] WL Wang, KJ Liao, CZ Cai, YB Zhu, Y Ma and HY Liao, *Diamond Relat. Mater.*, **12**, (2003), 1385–1388.

[5] HO Pierson, *Handbook of Carbon, Graphite, Diamond and Fullerenes - Properties, Processing and Applications*, William Andrew Publishing, Noyes, 1993.

[6] JC Riviere, *The Analyst*, **108**(1287), (1983), 649–684.

[7] C Kittel, *Introduction to Solid State Physics*, John Wiley & Sons Inc., New York, sixth edition, 1986.

[8] P Wilkes, *Solid State Theory in Metallurgy*, Cambridge University Press, London, New York, 1973.

[9] Y Lifshitz, SR Kasai, JW Rabalais and W Eckstein, *Physical Review B*, **41**(15), (1990), 10468–10480.

[10] SR Kasi, H Kang and JW Rabalais, *J. Chem. Phys.*, **88**(9), (1988), 5914–5924.

[11] Z Sitar, PC Yang, CA Wolden, R Schlesser, JT Prater and W Liu, *Diamond Relat. Mater.*, **7**, (1998), 276–282.

[12] Y Hayashi, N Shiraokawa and S Nishino, *Thin Solid Films*, **374**, (2000), 268–273.

[13] JO Orwa, KW Nugent, DN Jamieson and S Prawer, *Physical Review B*, **62**(9), (2000), 5461–5472.

[14] JE Field, *The Properties of Diamond*, Academic Press, New York, 1979.

[15] G Davies, *Diamond*, Adam Hilger Ltd, Bristol, 1984.

[16] JC Angus, in A Paoletti and A Tucciarone (eds.), *International School of Physics, Enrico Fermi Course CXXXV, The Physics of Diamond*, IOS Press, Amsterdam, 1997.

[17] JF Prins, *Materials Science Reports*, **7**, (1992), 721.

[18] JPF Sellschop, A Freund, J Hoszowska, SH Connell, M Rebak and RC Burns, *Phys. Stat. Sol. (a)*, **193**(3), (2002), 415–422.

[19] SH Connell, RC Burns, JO Hansen, AG Anker and J Hartwig, in *Electronic Proceedings: The 2nd International Conference on Diamond for Modern Light Sources*, Kwa Maritane, South Africa, 2006, (Organising Committee).

[20] J Isberg, J Hammersberg, E Johansson, T Wikstrom, DJ Twitchen, AJ Whitehead, SE Coe and GA Scarsbrook, *Science*, **297**(5587), (2002), 1670–1672.

[21] DJ Twitchen, AJ Whitehead, SE Coe, J Isberg, J Hammerberg, T Wikstrom and E Johansson, *IEEE Transactions on Electronic Devices*, **51**(5), (2004), 826–828.

[22] JR Zeidler, CA Hewett and RG Wilson, *Physical Review B*, **47**(4), (1993), 2065–2071.

[23] F Fontaine, C Uzan-Saguy, B Philosoph and R Kalish, *Applied Physics Letters*, **68**(16), (1996), 2264–2266.

[24] JF Prins, *Nucl. Instr. and Meth. A*, **514**, (2003), 69–78.

[25] JF Prins, *Physical Review B*, **61**(11), (2000), 7191–7194.

[26] JF Prins, *Semicond. Sci. Technol.*, **16**, (2000), 1–3.

[27] JF Prins, *Phys. Rev. B*, **39**, (1989), 3764.

[28] JF Prins, *J. Phys. D: Appl. Phys.*, **34**, (2001), 1–8.

[29] JF Prins, in A Paoletti and A Tucciarone (eds.), *International School of Physics, Enrico Fermi Course CXXXV, The Physics of Diamond*, IOS Press, Amsterdam, 1997.

[30] O Yang and BV King, *Nucl. Instr. and Meth. B*, **106**, (1995), 555–559.

[31] JF Prins, *Semicond. Sci. Technol.*, **18**, (2003), 27–33.

[32] T Vogel, J Meijer and A Zaitsev, *Diamond Relat. Mater.*, **13**, (2004), 1822–1825.

[33] J Bernhole, A Antonelli, TM Del, Sole, Y Bar-Yam and ST Pantelides, *Physical Review Letters*, **61**(23), (1988), 2689–2692.

[34] JF Prins, *Diamond Relat. Mater.*, **9**, (2000), 1835–1839.

[35] Y Lifshitz, SR Kasai, JW Rabalais and W Eckstein, *Physical Review B*, **44**(6), (1991), 2470–2479.

[36] JF Prins and TE Derry, *Nucl. Instr. and Meth. B*, **166**, (2000), 364–373.

[37] J Nakata, *Physical Review B*, **60**(4), (1999), 2747–2761.

[38] R Kalish, A Reznik, KW Nugent and S Prawer, *Nucl. Instr. and Meth. B*, **148**, (1999), 626–633.

[39] G Davies, *Physica B*, **273**, (1999), 15–23.

[40] R Kalish, in A Paoletti and A Tucciarone (eds.), *International School of Physics, Enrico Fermi Course CXXXV, The Physics of Diamond*, IOS Press, Amsterdam, 1997.

[41] K Ueda, M Kasu, A Tallaire and T Makimoto, *Diamond Relat. Mater.*, **15**, (2006), 1789–1791.

[42] K Ueda, M Kasu and T Makimoto, *Appl. Phys. Lett.*, **90**, (2007), 122102–1–122102–4.

[43] K Thonke, *Semicond. Sci. Technol.*, **18**, (1989), 20–26.

[44] JF Prins, *Physical Review B*, **38**(8), (1998), 5576–5584.

[45] M Suzuki, S Koizumi, M Katagiri, H Yoshida, N Sakuma, T Ono and T Sakai, *Diamond Relat. Mater.*, **13**, (2004), 2037–2040.

[46] K Haenen, M Nesladek, DL Schepper, R Kravets, M Vanecek and S Koizumi, *Diamond Relat. Mater.*, **13**, (2004), 2041–2045.

[47] H Kato, S Yamasaki and H Okushi, *Diamond Relat. Mater.*, **14**, (2005), 2007–2010.

[48] H Sternschulte, K Thonke, R Sauer and S Koizumi, *Physical Review B*, **59**(20), (1999), 12924–12927.

[49] A Aleksov, A Denisenko, M Kunze, A Vescan, A Bergmaier, G Dollinger, W Ebert and E Kohn, *Semicond. Sci. Technol.*, **18**, (1989), 59–66.

[50] AJ Garrido, CE Nebel, R Todt, G Rösel, C Amann, M Stultzmann, E Snidero and P Bergonzo, *Appl. Phys. Lett.*, **82**(6), (2003), 989–990.

[51] T Makino, H Kato, SG Ri, Y Chen and H Okushi, *Diamond Relat. Mater.*, **14**, (2005), 1995–1998.

[52] JP Goss, PR Briddon, R Jones and S Sque, *Diamond Relat. Mater.*, **13**, (2004), 684–690.

[53] SH Connell, IZ Machi and K Bharuth-Ram, *Hyperfine Interactions*, **159**, (2004), 217–226.

[54] T Miyazaki, H Okushi and T Uda, *Physical Review Letters*, **88**(6), 066402-1-066402-4.

[55] AB Anderson and EJ Grantscharova, *Physical Review B*, **54**(20), (1996), 14341–14348.

[56] SA Kajihara, A Antonelli, J Berholc and R Car, *Physical Review B*, **66**(15), (1991), 2010–2013.

[57] J Shirafuji and T Sugino, *Diamond Relat. Mater.*, **5**, (1996), 706–713.

[58] J Van der Weide and RJ Nemanich, *Physical Review B*, **49**(19), (1994), 13629–13637.

[59] BD Thomas, MS Owens and JE Butler, *Appl. Phys. Lett.*, **65**(23), (1994), 2957–2959.

[60] JE Butler and LR Woodin, *Phil. Trans. R. Soc. Lond. A*, **342**, (1993), 209–224.

[61] BD Thoms and JE Butler, *Surface Science*, **328**, (1995), 291–301.

[62] T Fraunheim, T Kohler, M Sternberg, D Porezag and MR Pederson, *Thin Solid Films*, **272**, (1996), 314–330.

[63] J Furthmuller, J Hafner and G Kresse, *Physical Review B*, **53**(11), (1996), 7334–7351.

[64] FJ Himpsel, DE Eastman, P Heinmann and JF Veen, *Physical Review B*, **24**(12), (1981), 7270–7274.

[65] Y Mori, H Kawarada and A Hiraki, *Appl. Phys. Lett.*, **58**(9).

[66] PE Pehrsson, JP Long, MJ Marchywka and JE Butler, *Appl. Phys. Lett.*, **67**(23).

[67] PK Baumann and RJ Nemanich, *Physical Review B*, **58**(3), (1998), 1643–1654.

[68] TA Kennedy, JS Colton, JE Butler, RC Linares and PJ Doering, *Appl. Phys. Lett.*, **83**(20), (2003), 4190–4192.

[69] JR Rabeau, YL Chin, S Prawer, F Jelezko, T Gaebel and J Wrachtrup, *Applied Physics Letters*, **86**(131926), (2005), 1–3.

[70] J Meijer, B Burchard, M Domhan, C Wittmann, T Gaebel, I Popa, F Jelezko and J Wrachtrup, *Applied Physics Letters*, **87**(261909), (2005), 1–3.

[71] T Gaebel, M Domhan, I Popa, C Wittmann, P Neumann, F Jelezko, J Rabeau, N Stavrias, AD Greentree, S Prawer, J Meijer, J Twamley, PR Memmer and J Wrachtrup, *Nature Physics*, **2**, (2006), 408–4–13.

[72] R Hanson, O Gywat and DD Awschalom, *Physical Review B*, **74**(161203), (2006), 1–4.

[73] EA Ekimov, VA Sidorov, ED Bauer, NN Mel'nik, NJ Curro and JD Thompson, *Nature*, **428**, (2004), 542–545.

[74] VG Vins and EV Pestryakov, *Diamond Relat. Mater.*, **15**, (2006), 569–571.

[75] JF Ziegler, JP Biersack and U Littmark, *The stopping and range of ions in solids*, Pergamon, New York, 1985.

[76] L Dobrzynski, *Handbook of Surfaces and Interfaces*, Garland STPM Press, New York and London, 1978.

[77] AJ Forty, *Surface Science Vol. 1*, ICTP, Trieste, Vienna, 1975, IAEA-SMR-15/11.

[78] JC Vickerman, *Surface Analysis: The Principal Techniques*, John Wiley & Sons Ltd., England, 1997.

[79] GC Allen, PM Tucker and RK Wild, *Surface Science*, **68**, (1977), 469–478.

[80] LA Harris, *Analytical Chemistry*, **40**(14), (1968), 25–34.

[81] HJ Steffen, CD Roux, D Marton and JW Rabalais, *Physical Review B*, **44**(8).

[82] NV Richardson and DA King, *Phys. Bull.*, **36**.

[83] A Hoffman, S Prawer and R Kalish, *Physical Review B*, **45**(22), (1992), 12736–12745.

[84] HG Maguire, *Phys. Stat. Sol. (b)*, **76**, (1976), 715.

[85] OE Mustecaplioglu and AS Shumovsky, *Physical Review B*, **60**(6), (1999), 3970–3975.

[86] WF Smith, *Principles of Materials Science and Engineering*, McGraw-Hill Inc, New York, 1990, Int. Edition.

[87] G Dearnaley, *Rep. Prog. Physics*, **32**, (1969), 405–491.

[88] R Ohl, *Bell Systems Tech. J.*, **31**, (1952), 204.

[89] WD Cussins, *Prog. Phys. Soc. B*, **68**, (1955), 213.

[90] W Shockley, *U.S. Patent No. 2 787 564.*

[91] W Moyer, J, *U.S. Patent No. 2 842 466.*

[92] T Alvager and NJ Hansen, *Rev. Sci. Instrum.*, **33**, (1962), 567.

[93] WJ Martin, FW ad King and S Harrison, *IEEE, Trans. Nucl. Sci.*, **NS-11**(3), (1964), 280.

[94] S Kalbitzer, R Bader, H Herzer and K Bethge, *Z. Phys.*, **203**, (1967), 117.

[95] O Meyer and G Haushahn, *Nucl. Instrum. Meth.*, **56**, (1967), 177.

[96] JW Mayer, *Nucl. Instrum. Meth.*, **63**, (1968), 144.

[97] JA Kerr and LN Large, in *Proc. Conf. Applications of Ion Beams to Semiconductor Technology*, 1967.

[98] PN Wang, Z Guo, XT Ying, JH Chen, XM Xu and FM Li, *Physical Review B*, **59**(20), (1999), 13347–13349.

[99] H Cheng, QM Jonathan, Wu, J Shen, S Kotake and Y Suzuki, *Thin Solid Films*, **402**, (2002), 117–120.

[100] DH Lee, H Lee, B Park, DB Poker and L Reister, *Appl. Phys. Lett.*, **70**(23), (1997), 3104–3106.

[101] TE Derry, JF Prins, CCP Madiba, J Ennis, RA Spits and JPF Sellschop, *Nucl. Instr. and Meth. B*, **35**, (1988), 431–434.

[102] JF Prins, TE Derry and JPF Sellschop, *Physical Review B*, **34**(12), (1986), 8870–8874.

[103] JF Prins, TE Derry and JPF Sellschop, *Nucl. Instr. and Meth. B*, **18**(12), (1987), 261–263.

[104] JPF Sellschop and SH Connell, *Nucl. Instr. and Meth. B*, **123**, (1998), 1253–1258.

[105] C Uzan-Saguy, C Cyterman, R Brener, V Richter, M Shaanan and R Kalish, *Appl. Phys. Lett.*, **67**(9), (1995), 1194–1196.

[106] E Friedland and LC Prinsloo, *Surface and Coatings Technology*, **158**, (2002), 64–68.

[107] S Prawer and RJ Nemanich, *Phil. Trans. R. Soc. Lond. A*, **362**, (2004), 2537–2565.

[108] E Friedland and JPF Sellschop, *Nucl. Instr. and Meth. B*, **191**, (2002), 17–21.

[109] KL Bhatia, S Fabian, S Kalbitzer, Ch Klatt, W Kratschmer, R Stoll and JPF Sellschop, *Thin Solid Films*, **324**, (1998), 11–18.

[110] W Matthias, *Semicond. Sci. Technol.*, **18**, (1989), 41–46.

[111] TS Lee, WM Lau, LJ Huang, Z Ren and F Qin, *Diamond Relat. Mater.*, **4**, (1995), 1353–1359.

[112] CE Nebel, *Semicond. Sci. Technol.*, **18**, (2003), 1–11.

[113] A Mainwood, *Physical Review B*, **49**(12), (1994), 7934–7040.

[114] A Mainwood, FP Larkins and AM Stoneham, *Solid State Electronics*, **21**, (1978), 1431–1433.

[115] G Davies, SC Lawson, AT Collins, A Mainwood and SJ Sharp, *Physical Review B*, **46**(20), (1992), 13157–13170.

[116] JP Goss, BJ Coomer, R Jones, TD Shaw, PR Briddon, M Rayson and S Oberg, *Physical Review B*, **63**(195208), (2001), 1–8.

[117] DC Hunt, DJ Twitchen, ME Newton, JM Baker, TR Anthony, WF Banholzer and SS Vagarali, *Physical Review B*, **61**(6), (1991), 3863–3876.

[118] RA Spits, TE Derry and JF Prins, *Nucl. Instr. and Meth. B*, **64**, (1992), 210–214.

[119] EH Lee, DM Hembree, Jr, GR Rao and LK Mansur, *Physical Review B*, **48**(21), (1993), 15540–15551.

[120] K Lakoubovskii and A Stesmans, *Physical Review B*, **66**, 045406-1-7.

[121] AT Collins, in A Paoletti and A Tucciarone (eds.), *International School of Physics, Enrico Fermi Course CXXXV, The Physics of Diamond*, IOS Press, Amsterdam, 1997.

[122] MC Rossi, *Applied Physics Letters*, **73**(9), (1998), 1203–1205.

[123] AC Ferrari and J Robertson, *Phil. Trans. R. Soc. Lond. A*, **362**, (2004), 2477–2512.

[124] JW Ager III, DK Veirs and GM Rosenblatt, *Physical Review B*, **43**(8), (1991), 6491–6499.

[125] L Bergman and RJ Nemanich, *J. Appl. Phys.*, **78**(11), (1995), 6709–6719.

[126] AC Ferrari and J Robertson, *Physical Review B*, **61**(20), (2000), 14095–14107.

[127] AC Ferrari and J Robertson, *Physical Review B*, **63**(121405), (2001), 1–4.

[128] Y Lifshitz, SR Kasi and JW Rabalais, *Physical Review Letters*, **62**(11), (1989), 1290–1293.

[129] BV Derjaguin, BV Spitsyn, AE Gorodetsky, AP Zakharov, LL Bouilov and AE Aleksenko, *Journal of Crystal Growth*, **31**, (1975), 44–48.

[130] M Pitter, MB Hugenschmidt and RJ Behm, *Appl. Phys. Lett.*, **68**(18).

[131] LM Hanssen, WA Carrington, JE Butler and KA Snail, *Materials Letters*, **7**(7,8), (1988), 289–292.

[132] MG Donato, G Faggio, M Marinelli, G Messina, E Milani, A Paoletti, S Santangelo, A Tucciarone and RG Verona, *Eur. Phys. Journal B*, **20**, (2001), 133–139.

[133] C Ronning, *Appl. Phys. A: Ion beam synthesis and growth mechanism of diamond like materials*, DOI:10.1007/s00339-002-2063-7.

[134] M Zhibin, W Jianhua, W Qinchong and W Chuanxin, *Surface and Coatings Technology*, **155**, (2002), 96–101.

[135] H Natter, M Schemlzer and R Hempelmann, *J. Mater. Res.*, **13**(5), (1998), 1186–1197.

[136] L Constant and LF Normand, *Diamond Relat. Mater.*, **6**, (1997), 664–667.

[137] M Ece, B Oral and J Patscheider, *Diamond Relat. Mater.*, **5**, (1996), 211–216.

[138] JF Prins and HL Gaigher, in R Meissser, J Glass, J Butler, and R Roy (eds.), *Proc. 2nd Int. Conf. on new Diamond Science and Technology*, 567, Materials Research Society, Pittsburgh, PA, 1991.

[139] HA Hoff, DJ Vestyck, JE Butler and JF Prins, *Appl. Phys. Lett.*, **62**(1), (1993), 34–36.

[140] S Tong Lee, S Chen, G Braunstein, X Feng, I Bello and WM Lau, *Appl. Phys. Lett*, **59**(7).

[141] J Narayan, VP Goodbole and CW White, *Science*, **25**, (1991), 416–418.

[142] T Cabioc'h, M Jaouen, JP Riviere, J Delafond and G Hug, *Diamond Relat. Mater.*, **6**, (1997), 261.

[143] F Banhart and PM Ajayan, *Nature*, **382**, (1996), 433–435.

[144] Q Lu-Chang and S Iijima, *Chemical Physics Letters*, **262**, (1996), 252–258.

[145] A Hiroaki, *Diamond Relat. Mater.*, **10**, (2001), 1201–1204.

[146] SB Wang, PR Zhu and WJ Wang, *Surface and Coatings Technology*, **123**, (2000), 173–176.

[147] VD Blank, VV Aksenenkov, MY Popov, SA Perfilov, BA Kulnitskiy, YV Tatyanin, OM Zhigalina, BN Mavrin, VN Denisov, AN Ivlev, VM Chernov and VA Stepanov, *Diamond Relat. Mater.*, **8**, (1999), 1285–1290.

[148] R Selvan, R Unnikrishnan, S Ganapathy and T Pradeep, *Chemical Physics Letters*, **316**(3,4), (2000), 205–210.

[149] JF Prins, *Diamond Relat. Mater.*, **5**, (1996), 907–913.

[150] VS Vavilov, MA Gukasyan, MI Guseva, TA Karatygina and EA Konorova, *Sov. Phys. Semicond.*, **8**(4), (1974), 471–473.

[151] JJ Blandino, DG Goodwin and CE Garner, *Diamond Relat. Mater.*, **9**, (2000), 1992–2001.

[152] LC Prinsloo, *Appl. Phys. A*, **72**, (2001), 658–663.

[153] JD Hunn, SP Withrow, CW White and DM Hembree, Jr, *Physical Review B*, **52**(11), (1995), 8106–8111.

[154] DN Jamieson, S Prawer, KW Nugent and SP Dooley, *Nucl. Instr. and Meth. B*, **106**, (1995), 641–645.

[155] S Prawer, KW Nugent and DN Jamieson, *Diamond Relat. Mater.*, **7**, (1998), 106–110.

[156] R Walker, S Prawer, DN Jamieson, KW Nugent and R Kalish, *Appl.Phys.Lett.*, **71**(11), (1997), 1492–1494.

[157] JF Prins, *Diamond Relat. Mater.*, **10**, (2001), 463–468.

[158] JE Butler, MW Geis, KE Krohn, J Lawless, Jr, S Deneault, TM Lyszczarz, D Flechtner and R Wright, *Semicond. Sci. Technol.*, **18**, (1989), 67–71.

[159] CN Huggins and P Cannon, *Nature*, **194**, (1962), 829.

[160] N Fujimori, T Imai and A Doi, *Vacuum*, **36**, (1986), 99.

[161] JF Prins, *Appl. Phys. Lett.*, **41**, (1982), 950–952.

[162] PA Sullivan and RA Baragiola, *J. Appl. Phys.*, **76**(8), (1994), 4847–4852.

[163] S Koizumi, M Kamo, Y Sato, H Ozaki and T Inuzuka, *Appl. Phys. Lett.*, **71**, (1997), 1065.

[164] JF Prins, *Diamond Relat. Mater.*, **8**, (1999), 1635.

[165] S Koizumi, M Kamo, Y Sato, S Mita, A Sawebe, A Reznik, Uzan-Saguy and R Kalish, *Diamond Relat. Mater.*, **7**, (1998), 540.

[166] JF Prins, *Diamond Films Technol.*, **8**, (1998), 4.

[167] ZC Dong, AS Trivinof, NV Suetin and PV Minakov, *Surface Science*, **549**, (2004), 203–210.

[168] JR Prior and FC Champion, *Proc. Phys. Soc.*, **80**, (1962), 849–859.

[169] JF Prins, *J. Phys. D*, **D 22**, (1989), 1562.

[170] JF Prins, *Mater. Res. Innovat*, **1**, (1998), 243–253.

[171] JF Prins, *Diamond Relat. Mater.*, **3**, (1994), 922–925.

[172] JA Freitas, Jr, U Strom and AT Collins, *Diamond Relat. Mater.*, **2**, (1993), 87–91.

[173] AA Gippius, RA Khmelnitskiy, VA Dravin and SD Tkachenko, *Diamond Relat. Mater.*, **8**, (1999), 1631–1634.

[174] JA Freitas, PB Klein and AT Collins, in S Saito, N Fujimoro, O Fukunaga, M Kamo, K Kobashi and M Yoshikawa (eds.), *Advances in New Diamond Science and Technology*, 321–326, MYU, Tokyo, 1994.

[175] JF Prins, in S Saito, N Fujimoro, O Fukunaga, M Kamo, K Kobashi and M Yoshikawa (eds.), *Advances in New Diamond Science and Technology*, 443–448, MYU, Tokyo, 1994.

[176] SC Lawson, H Kanda, H Kiyota, T Tsutsumi and H Kawarada, in S Saito, N Fujimoro, O Fukunaga, M Kamo, K Kobashi and M Yoshikawa (eds.), *Advances in New Diamond Science and Technology*, 315–320, MYU, Tokyo, 1994.

[177] JF Prins, *Thin Solid Films*, **42**, (1992), 11.

[178] JF Prins, *Trans. Mater. Res. Soc. Jpn*, **14B**, (1994), 1571.

[179] JF Prins, *Thin Solid Films*, **11**, (1992), 212.

[180] JF Prins, *Appl. Phys. Lett.*, **73**, (1998), 16.

[181] AT Collins, M Kamo and Y Sato, *J. Phys. : Condens. Matter*, **1**, (1989), 4029–4033.

[182] H Sternschulte, K Thonke and R Sauer, *Phys. Stat. Sol (a)*, **172**(37), (1999), 37–48.

[183] S Koizumi, K Watanabe, M Hasegawa and H Kanda, *Science*, **292**(5523), (2001), 1899–1892.

Bibliography

S R Naidoo - Conference presentations

[1] TE Derry, SR Naidoo, *The implantation of radioactive cobalt-57 ions*, SRCNS Report 95/03, Internal Report, (1995).

[2] SR Naidoo, JF Prins, *Cathodoluminescence studies on CIRA processed diamonds*, SAIP conference, Mmabatho, (1994).

[3] SR Naidoo, MC Stemmet, *The implantation of radioactive Indium-111 for research purposes*, SAIP conference, Bloemfontein, (1991).

[4] CG Smallman, RW Fearick, TE Derry, SR Naidoo, *Lattice location of implanted flourine in diamond*, SAIP conference, Johannesburg, (1992).

[5] RD Maclear, JE Butler, SH Connell, BP Doyle, IZ Machi, SR Naidoo, JPF Sellschop, *Quantatative trace hydrogen distributions in natural and synthetic diamond using 3D-micro-ERDA microscopy*, Ion Beam Analysis 13, Portugal, (1997).

[6] SR Naidoo, JF Prins, *Electron injection junctions in diamond*, SAIP conference, Durban, (1997).

[7] SR Naidoo, JF Prins, *Electron injection junctions in diamond created by phosphorus and carbon implantation*, ICNDST'98, Pretoria, (1998).

[8] T Hauser, SR Naidoo, E Friedland, *Diffusion behaviour of aluminium in silicon using NRA*, ICNDST'98, Pretoria, (1998).

[9] M Hayes, T Hauser, E Friedland, SR Naidoo, *Ranges of aluminium ions implanted into targets with atomic number > 23*, Ion Beam Analysis 13, Portugal, (1997).

[10] SR Naidoo, JF Prins, *Carbon overgrowths on copper by ion implantation*, SAIP conference, Cape Town, (1998).

[11] SR Naidoo, JF Prins, JD Comins, M Nieuwoudt, *Investigation of radiation damage after ion implantation in diamond using Raman spectroscopy*, SAIP conference, Johannesburg, (2000).

[12] P Letaba, J Lafait, TH Pagat, SR Naidoo, TE Derry, M Maaza, *Nano-composites: 3rd order optical sensitivity*, SAIP conference, Durban, (2001).

[13] M Harting, DF Kanguwe, CM Comri, S Nsengiyumva, SR Naidoo, TE Derry, DT Britton, *Vacancy and krypton dynamics in naturally oxidised aluminium*, ICPA-13, Japan, (2003).